Exclusive Photo-Production Measurement of $K^+\Sigma^{*-}$ off Quasi-Free Neutrons in Deuterium

By

Haiyun Lu

Bachelor of Science
Fudan University 1999, China
Master of Science
Fudan University 2002, China

Submitted in Partial Fulfillment of the Requirements

for the Degree of Doctor of Philosophy in

Physics

College of Arts and Sciences

University of South Carolina

2010

Accepted by:

Ralf Gothe, Major Professor

Fred Myhrer, Committee Member

David Tedeschi, Committee Member

Shmuel Nussinov, Committee Member

James Buggy, Interim Dean of the Graduate School

ProQuest LLC
789 East Eisenhower Parkway
P.O. Box 1346
Ann Arbor, MI 48106-1346

Acknowledgments

First off, I would like to thank Mengyin Li, my wife, for supporting and encouraging me.

I would like to give a great thanks to my adviser, Ralf Gothe. I joined the group with little knowledge of nuclear physics, and I have learned so much from him, which has enabled me to finish my analysis and PhD thesis. Even the little knowledge I had before I joined the group was learned in his classroom and lab. Moreover, he encourages me to pursue my ideas and provides a large amount of time and effort to discussions and helping me with both physics and daily issues. I would like to thank Fred Myhrer, David Tedeschi and Shmuel Nussinov for serving on my thesis committee and providing many helpful suggestions. I would also like to thank Chaden Djalali, Steffen Strauch and Yordanka Ilieva in our group for sharing their academic experience with me and various forms of helps.

I can not thank enough my group mates. They are helping me almost every day. Lewis Graham and Zhiwen Zhao have been together with me throughout my PhD program. Intensive discussion and funny talks (maybe together with Ralf) have made my office life much less boring and lonely. Evan Phelps, Robert Steinman (lastname correct this time) and Ye Tian (the only female in the group) always provide views from different aspects. We have a good group and I appreciate it very much. It greatly helps my work and daily life.

I am indebted to the EG3 analysis group members. Obviously, I could not finish my thesis without the help from them, Elton Smith, Stepan Stepanyan, Hovanes Egiyan and Paul Mattione.

I would like to give thanks to Jörn Langheinrich, Kijun Park (two previous post-doctoral fellows in our group) and Lei Guo for giving me practical and detailed help. Jörn guided me through the complex and confusing simulation and cooking software and related terminologies.

There are also a number of people who I would like to thank for non-physics reasons. First and foremost, I need to thank my parents Along and Guomei for their backup and continuous support. I do want to thank Beth Powell. When I started my graduate program in this strange country, she helped me in getting familiar with the US system and helped me solve complex department and college issues. A similar appreciation goes to Mary Papp. Finally, surviving graduate school more than seven years would not have been possible without friends. Those not listed above include Hongxuan Liu, Baowei Liu, Zhihua Cai, Jiajie Lin, Xurong Chen, Karen Wu, Hongquan Wang and Peng Liang.

Abstract

This work studies the exclusive quasi-free photo-production of $K^+\Sigma^{*-}(1385)$ off neutrons in deuterium. It presents the first total cross section, σ, of this production channel as well as the differential cross section, $\frac{d\sigma}{dcos\theta^K_{CM}}$. In order to understand the production mechanism, the angle distribution in the t-channel helicity frame (Gottfried-Jackson frame) is presented. The experiment was done in Hall B at the Thomas Jefferson National Laboratory (JLab) by using the CEBAF Large Acceptance Spectrometer (CLAS) detector system and the tagger system during the EG3 run period from December 2004 to February 2005. Tagged photons with energies from 1.5 to 5.5 GeV are measured in coincidence with $K^+p\pi^-\pi^-$ in the spectrometer for this channel. After careful detector calibration and developing a new particle identification method and event selection, a very clean data sample with high signal-to-background ratio was obtained with little data loss. This enables us to obtain results agreeing with previous published data and greatly extending the energy coverage.

Contents

List of Tables

List of Figures

Chapter 1

Introduction and Overview

In the process of discovering the world we live in, there are four fundamental interactions found. The gravitational force induced by the mass provides the stage of time and space for the other interactions. The other three interactions, electromagnetic, weak and strong, govern the behavior of fundamental particles. The matter around us in normal life is composed of atoms bound by electromagnetic interaction. The atom is composed of a nucleus and electrons surrounding it, bound to one another by electromagnetic interaction, too. The nucleus is composed of nucleons, which are protons and neutrons. Free neutrons can decay to protons and hyperons to nucleons, which are processes of weak interaction. How strong interaction glues quarks together to nucleons is still not understood in its full complexity. Only in deep inelastic scattering the strong interaction can be described in the language of a perturbative quantum field theory of Quantum Chromodynamics (pQCD) within the framework of the Standard Model of particle physics. The mass of an atom originates mainly from the nucleus, since the ratio of electron mass to nucleon mass is about 1 to 2000. How strong interaction generates this mass and confines quarks at intermediate distances together is still not clear. This work is a small part in a larger picture of trying to find the answer to these questions.

1.1. QCD and Mass of Visible Matter

1.1.1. QCD and QED. As stated above, the strong interaction as one of the four fundamental forces of physics is currently described by perturbative Quantum Chromodynamics (pQCD) or QCD inspired models. QCD generates the interaction

TABLE 1.1. Properties of quarks

Symbol	u	c	t
Name	Up	Charm	Top
Charge(e)	+2/3	+2/3	+2/3
Mass$\left(MeV/c^2\right)$	1.5-3.0	1250 ± 90	$1.725 \pm 0.023 \times 10^5$
Symbol	d	s	b
Name	Down	Strange	Bottom
Charge(e)	-1/3	-1/3	-1/3
Mass$\left(MeV/c^2\right)$	3-7	95 ± 25	4200 ± 70

between quarks and gluons, inside of hadrons. Quarks are fermions belonging to the large group of fundamental particles with half-integer spin. Elementary fermions are the basic building blocks of the visible world and interact with each other via bosons with integer spin. Gluons are one type of bosons, which mediate the interaction between quarks. Quarks besides leptons are one kind of fundamental particles, which are not composed of other particles and therefore point-like particles. They have six different flavors and all of them are electrically charged. Each quark has its own antiparticle or antiquark. Table 1.1 summarized the properties of the six known quarks.

QCD is often compared with Quantum Electrodynamics (QED), which describes the electromagnetic interaction. In QED, elementary processes are that electrically charged particles interact with each other through neutral and massless particles, called photons. Similarly, particles of color charge, or color, are subject to strong interaction, which is the origin of Chromodynamics. There is only one type of charge in QED, while there are three types of color in QCD. These colors are red, green and blue. Each quark carries a color, and the combination of red, green and blue is neutral. Therefore, the simplest model of a color-neutral baryon, whose quantum number is described by quarks only, is based on three quarks. The gluon-mediating interaction between two quarks of different color has color. This implies that a gluon can not only interact with a quark, but also with another gluon. This feature of QCD has an important impact on the coupling constant, which shows how strong the

coupling of the interaction is. The asymptotic freedom behavior of quarks and the decreasing strong coupling constant was proposed by [13, 6, 7]. It has been proven experimentally, and Figure 1.1 shows the worldwide results from different reactions [3].

The difference between QCD and QED as mentioned above makes it currently impossible to solve the QCD equation of motion in the full kinematic regime analytically. However, different approximations are developed for different energy ranges. At high energies, the coupling constant is small compared to unity. The perturbation method, pQCD, is applied similarly to QED. At low energies, the coupling constant becomes large and pQCD is no longer valid. Effective field theories like Chiral Perturbation Theory (ChPT) or QCD inspired model calculations are applied here. A potentially bridging alternative is Lattice QCD (LQCD).

1.1.2. Lattice QCD. In order to solve QCD on the lattice, the first step is to define the Lagrangian

$$L_{QCD} = -\frac{1}{4} G^{\mu\nu}_{\alpha} G^{\alpha}_{\mu\nu} + \sum_{f} \bar{q}_f \left[i\gamma^{\mu} D_{mu} - m_f \right] q_f \tag{1.1}$$

with the gluon field tensor

$$G^{\mu\nu}_{\alpha} = \partial^{\mu} A^{\nu}_{\alpha} - \partial^{\nu} A^{\mu}_{\alpha} + g f^{bc}_{\alpha} A^{\mu}_{b} A^{\nu}_{c} \tag{1.2}$$

and the gauge covariant derivative

$$D^{\mu} = \partial^{\mu} - i\frac{g}{2} A^{\mu}_{\alpha} \lambda^{\alpha}, \tag{1.3}$$

where A^{μ}_{a} represents the gluon field, g the strong coupling constant and f the quark flavor. The method of path integrals is used to determine the expectation value of an observable O

$$\langle O \rangle = \frac{1}{Z} \int d\psi d\bar{\psi} O e^{iS}, \tag{1.4}$$

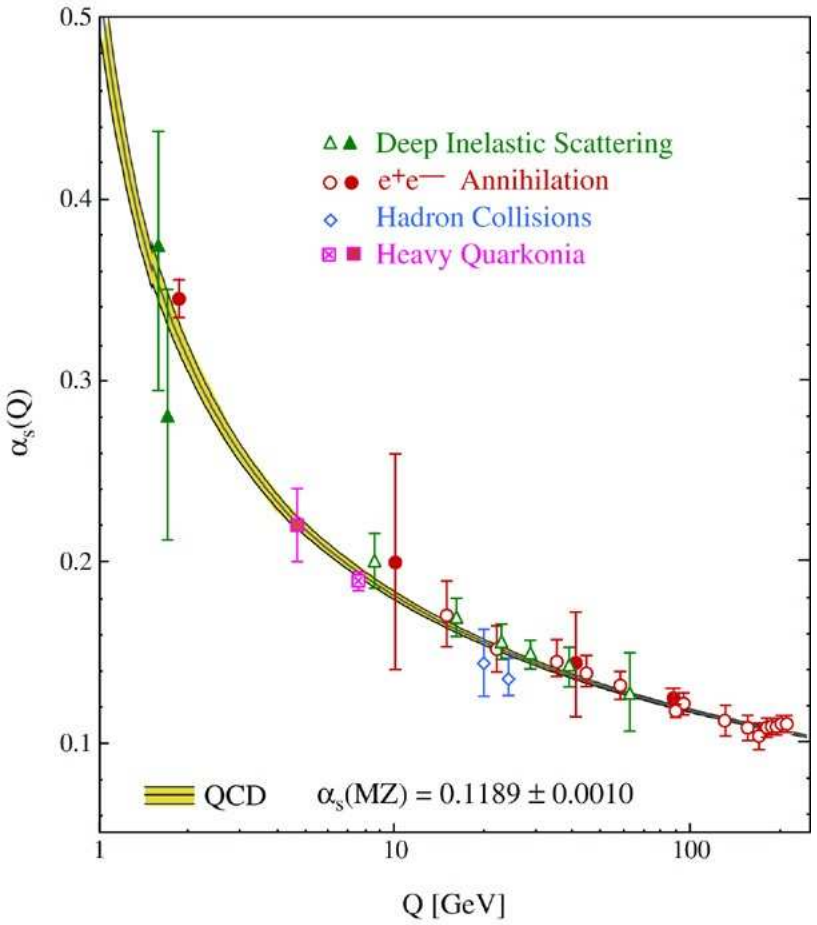

FIGURE 1.1. Running Coupling Constant of QCD. α_s is defined as $\frac{g^2}{4\pi}$ and g is the color like the charge e in QED.

where Z is the partition function

$$Z = \int d\psi d\bar{\psi} e^{iS} \tag{1.5}$$

and S the classical action

$$S = \int dx L_{QCD} \tag{1.6}$$

with L_{QCD} the Lagrangian density. These two equations. (1.1) and (1.4), allow to compute the mass of baryons on the lattice.

Lattice QCD (LQCD) was proposed by Wilson [15] and becomes an especially useful solution when pQCD is not longer applicable. The equation of motion is discretized on a four dimensional Euclidean space-time lattice. Quarks and gluons

can only exist on lattice points and travel over connection lines. The transfer from Minkowski space to Euclidean space is done by redefining

$$x_0 = -ix_4 \tag{1.7}$$

and

$$S_E = iS_M, \tag{1.8}$$

where the time variable is Wick rotated to imaginary time and the action is rotated accordingly. Therefore the factor e^{iS} in (1.4) becomes e^{-S}. The process of approximating the continuum by the discretized lattice is shown Figure 1.2. Accordingly, the integration is replaced

$$\int d^4x \to a^4 \sum_n, \tag{1.9}$$

where a is the lattice constant. It introduces an ultraviolet cutoff of $\frac{1}{a}$, whose impact needs to be investigated and an appropriate continuum limit ($a \to 0$) to get back the continuum theory has to be established. After this discretization, scalars become

$$\begin{aligned} \phi(x) &\to \phi(na) \\ & n = (n_1, n_2, ..., n_D), \end{aligned} \tag{1.10}$$

and derivatives become

$$\partial_\mu \phi(x) \to \frac{\phi((n+\widehat{\mu})a) - \phi((n-\widehat{\mu})a)}{2a} \tag{1.11}$$

with $\widehat{\mu}$ the unit vector along the derivative direction on the lattice similar to n. This approach is very similar to the one used in classical statistical mechanics as summarized in Table 1.2 [9].

For a gauge field on a lattice, scalars sit on lattice points (sites) and vectors are presented by lattice links as described above. Here a gauge field

$$A^a_\mu(x) T^a \in SU(N) \tag{1.12}$$

with

$$\begin{aligned} trT^a &= 0, (T^a)^\dagger = T^a \\ trT^aT^b &= \frac{1}{2}\delta^{ab} \\ \left[T^a, T^b\right] &= if^{abc}T^c \end{aligned} \tag{1.13}$$

and f^{abc} structure constant of SU(N) is not gauge covariant, because it transforms under a gauge transformation like

$$A_\mu(x) \to \frac{\Omega(x)\,\partial_\mu\Omega^\dagger(x)}{ig} + \Omega(x)\,A_\mu(x)\,\Omega^\dagger(x) \tag{1.14}$$

with $\Omega(x) \in SU(N)$. This can be solved by introducing new link variables

$$U_{n,\mu} = exp\left[igaA_\mu(n)\right] \in SU(N) \tag{1.15}$$

and

$$U_{n+\widehat{\mu},-\mu} \equiv U^\dagger_{n,\mu}, \tag{1.16}$$

whose transformation under $g_n \in SU(N)$

$$U_{n,\mu} \to U^g_{n,\mu} = g_n U_{n,\mu} g^\dagger_{n+\widehat{\mu}} \tag{1.17}$$

is covariant. The product of the link variables transforms under gauge transformation as

$$\prod U \equiv U_{n,\mu_1}U_{n+\widehat{\mu}_1,\mu_2}...U_{m-\widehat{\mu}_k,\mu_k} \to g_n \prod U g^\dagger_m \tag{1.18}$$

and for a closed loop C at n as

$$\prod_C U \to g_n \left\{\prod_C U\right\} g^\dagger_n, \tag{1.19}$$

which implies that $tr\left\{\prod_C U\right\}$ is gauge invariant. The closed path on the four-dimensional Euclidean space-time lattice with $U_{n,\mu}$ matrices defined on the links that connect neighboring sites is called a Wilson Loop. As shown above, traces of products

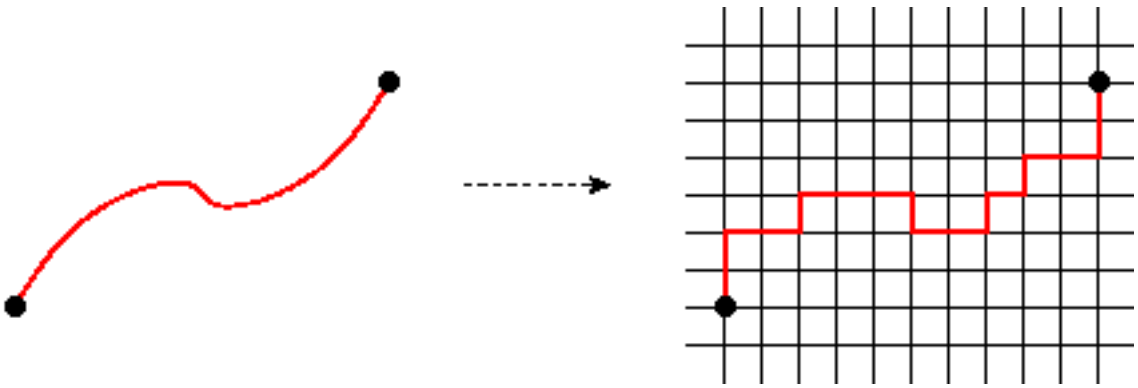

FIGURE 1.2. Discretization of space time in LQCD.

of such matrices along Wilson Loops are gauge invariant. The other gauge invariant quantity is an ordered string of $U_{n,\mu}$ matrices capped by a fermion and an anti-fermion. Therefore the gauge invarance on the lattice is guaranteed. The simplest Wilson Loop, the 1×1 lattice square, agrees with the QCD action to the order $O\left(a^4\right)$. It can be shown by direct Taylor expansion of the lattice expression of the Wilson Loop

$$Re\left(Tr\left(1 - W^{1\times 1}\right)\right) = \frac{a^4 g^2}{2} F_{\mu\nu} F^{\mu\nu}. \tag{1.20}$$

To calculate the mass of hadrons, the propagator is calculated. The mass of the ground state is obtained, when all other states vanish as the time approaches infinity. This result depends on the input mass of the quarks, and needs to be extrapolated to the chiral and the continuum limits, which means the lattice constant goes to zero. The mass spectrum of hadrons from LQCD compared with experimental data is shown in Figure 1.3 [9].

1.1.3. Mass of Visible Matter. The mass spectrum from LQCD is actually very important, since one of the very fundamental questions is "where does the atomic mass come from?" The mass components of the current universe are 4.6% of atoms, 23% of dark matter, and 72% of dark energy. To further distinguish atoms from dark matter and dark energy, atoms are also called visible matter. More than 98% of the visible matter is in fact coming from QCD. Protons and neutrons are the ingredients

TABLE 1.2. The equivalence between a Euclidean field theory and classical statistical mechanics [9].

Euclidean Field Theory	Classical Statistical Mechanics
Action	Hamiltonian
unit of action h	unit of energy $\beta = 1/kT$
Feyman weight for amplitudes $e^{-S/h} = e^{-\int Ldt/h}$	Boltzmann factor $e^{\beta H}$
Vacuum to vacuum amplitude $\int D\phi e^{-S/h}$	Partition function $\sum_{conf.} e^{-\beta H}$
Vacuum energy	Free Energy
Vacuum expectation value $\langle 0\|O\|0\rangle$	Canonical ensemble average $\langle O\rangle$
Time ordered products	Ordinary products
Green's functions $\langle 0\|T\left[O_1...O_n\right]\|0\rangle$	Correlation functions $\langle O_1...O_n\rangle$
Mass M	Correlation length $\xi = 1/M$
Mass-gap	Exponential decrease of correlation functions
Mass-less excitations	Spin waves
Regulation: cutoff $\Lambda \equiv \frac{1}{a}$	lattice spacing a
Renormalization: $\Lambda \to \infty$	continuum limit $a \to 0$
Changes in the vacuum	phase transitions

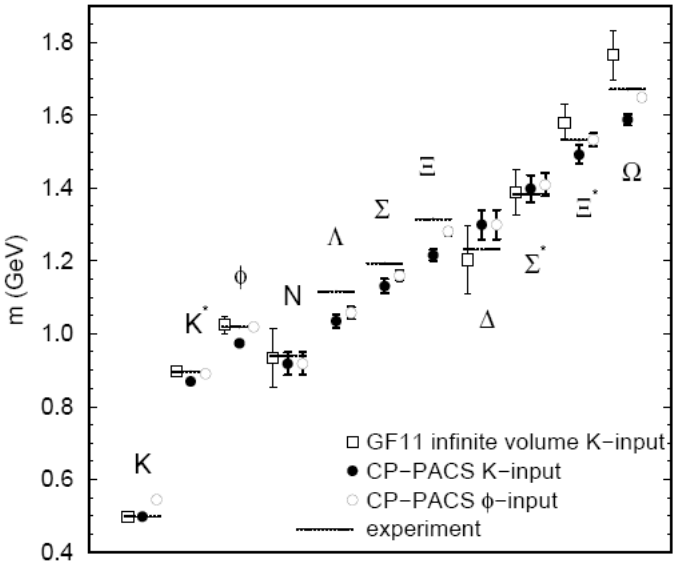

FIGURE 1.3. Hadron spectrum of LQCD in comparison with experimental data citepGupta:1997nd. Data represented by lines are from experiments, square boxes from GF11 project with kaon mass as input, circles from CP-PACS project with input from kaon mass for solid circle and ϕ mass for open circle.

of nuclei in the center of atoms. They are composed of up and down valence quarks. But the masses of up and down bare quarks are below 5 MeV/c^2. However, the masses of nucleons are close to 1 GeV, hence the mass of quarks contribute almost nothing. Instead, the strong interaction between them is the origin of mass as shown by LQCD calculations.

1.2. Baryon Spectroscopy

Hadrons are made of quarks hold together by the strong interaction. They can be again grouped into two categories, baryons and mesons. One way to distinguish them is that the total number of baryons is conserved in every reaction while the total number of mesons is not. A large number of baryons and mesons with different properties have been found. In order to explain and understand their spectra, the constituent quark model (CQM) was proposed, which considers hadrons as quantum bound states of elementary particles, quarks [5]. Baryons are composed of three quarks and mesons are composed of one quark and one antiquark.

1.2.1. Constituent Quark Model. In the constituent quark model, the property of baryons and mesons comes from the constituent quarks. Each quark has a baryon number of 1/3 so that each baryon has a baryon number of 1 and each meson has a baryon number of 0. In every reaction the baryon number needs to be conserved so that the total number of baryons is conserved. Since the baryon number of mesons is zero, the total baryon number of mesons is always zero no matter how many mesons involved in reactions.

Talking about the symmetries, the $SU(N)$ groups are intensively involved here. Because the masses of u, d and s quarks are significantly lower than those of the other three quarks, $SU(3)_{flavor}$ is often adopted. By also considering the group representing the spin of quarks, $SU(6)_{flavor-spin} = SU(2)_{spin} \otimes SU(3)_{flavor}$ is generated.

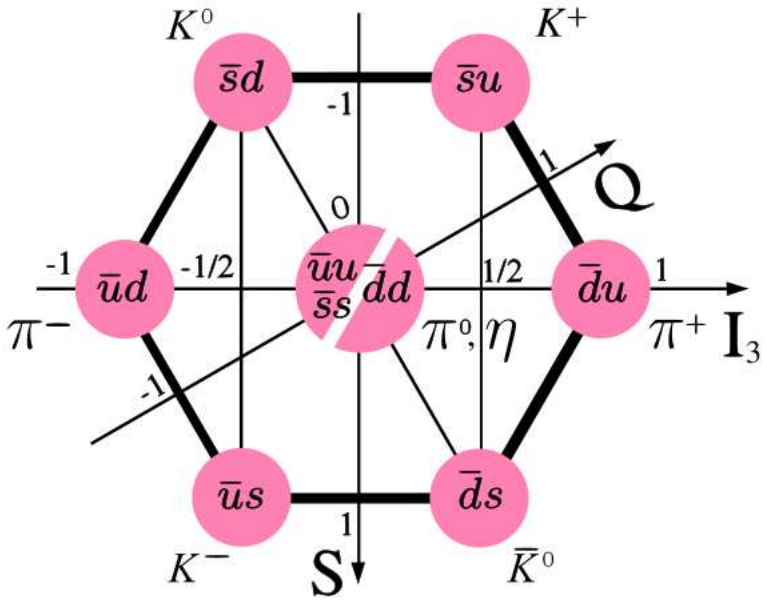

FIGURE 1.4. The meson octet ([14]).

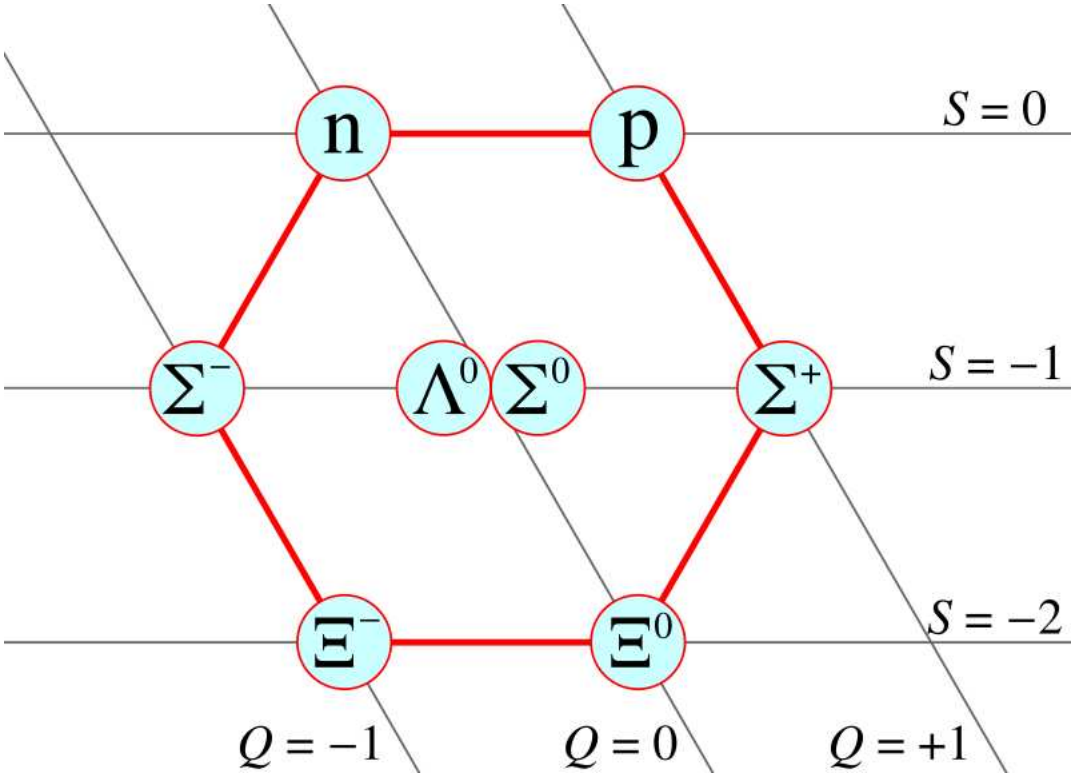

FIGURE 1.5. The Baryon octet ([14]).

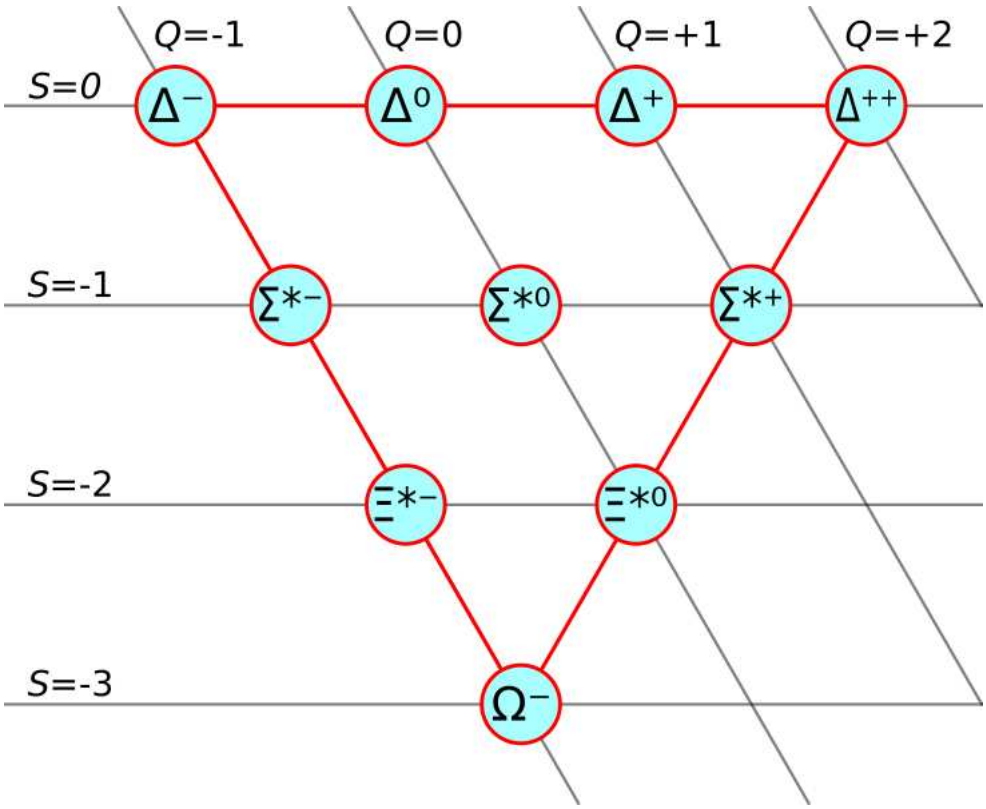

FIGURE 1.6. The Baryon decuplet ([14]).

Since the ground-state wavefunctions of mesons have the same color, spin and spatial components, the categorization solely comes from flavor decomposition. Therefore, the nine states, $SU(3)_{quark} \otimes SU(3)_{antiquark} = 8 \oplus 1$, are decomposed into an octet shown in Figure 1.4 and a singlet η'. A similar situation happens again for baryons, the flavor decomposition $SU(3) \otimes SU(3) \otimes SU(3) = 10 \oplus 8 \oplus 8 \oplus 1$ results in an octet of spin 1/2 baryon states shown in Figure 1.5 and a decuplet of spin 3/2 baryon states shown in Figure 1.6.

The baryon decuplet includes a Δ^{++} particle with spin $\frac{3}{2}$ and charge +2. The only quark combination leading to these quantum numbers is three u quarks (uuu) with spins aligned (↑↑↑). Therefore these three quarks have identical quantum numbers, which is forbidden by Pauli's exclusion principle. This led to the introduction of color, the "charge" of the strong interaction as described before.

TABLE 1.3. N* spectrum predicted by the Constituent Quark Model Capstick and Roberts [4].

J^P	M_{CQM}	M_{PDG}	Rating	J^P	M_{CQM}	M_{PDG}	Rating
$1/2^-$	1460	1535	****	$1/2^+$	1540	1440	****
$1/2^-$	1535	1650	****	$1/2^+$	1770	1710	***
$1/2^-$	1945	2090	*	$1/2^+$	1880		
$1/2^-$	2030			$1/2^+$	1975		
$1/2^-$	2070			$1/2^+$	2065	2100	*
$1/2^-$	2145			$1/2^+$	2210		
$1/2^-$	2195						
$3/2^-$	1495	1520	****	$3/2^+$	1795	1720	****
$3/2^-$	1625	1700	***	$3/2^+$	1870		
$3/2^-$	1960	2080	**	$3/2^+$	1910		
$3/2^-$	2055			$3/2^+$	1950		
$3/2^-$	2095			$3/2^+$	2030		
$3/2^-$	2165						
$3/2^-$	2180						
$5/2^-$	1630	1675	****	$5/2^+$	1770	1680	****
$5/2^-$	2080			$5/2^+$	1980	20000	**
$5/2^-$	2095	2200	**	$5/2^+$	1995		
$5/2^-$	2180						
$5/2^-$	2235						
$5/2^-$	2260						
$5/2^-$	2295						
$5/2^-$	2305						
$7/2^-$	2090	2190	****	$7/2^+$	2000	1990	**
$7/2^-$	2205			$7/2^+$	2390		
$7/2^-$	2255			$7/2^+$	2410		
$7/2^-$	2305			$7/2^+$	2455		
$7/2^-$	2355						
$9/2^-$	2215	2250	****	$9/2^+$	2345	2220	****
$11/2^-$	2600	2600	***				
$11/2^-$	2670						
$11/2^-$	2700						
$11/2^-$	2770						
$13/2^-$	2715						

1.2.2. Excited Nucleon Spectrum. In analogy to the excitation of the hydrogen atom, the nucleon can be excited, since it is a composite system. Table 1.3 lists the predicted excited nucleon states with resonance mass, angular momentum and parity number, and compares them with experimentally found resonances whose evidence is ranked by the number of stars. Most of these predicted states are not

found experimentally. These are often called "missing states". There are two obvious explanations. The first one is that the prediction is wrong. But despite of these missing states, the prediction matches the experiment pretty well, and there is no reason that exceptions should happen to these missing states. The other explanation is that these states do exist but they are not experimentally found.

One possible reason is that the experiments done so far have mostly scattered pions off nucleons. These missing states may only have small or no $N\pi$ coupling strength. Instead, they may couple to $N\pi\pi$, $N\rho$, $N\omega$ or even couple to kaon and hyperon, KY.

1.3. Photoproduction of $K^+\Sigma^{*-}$

The reaction this work studies is $\gamma d \to K^+\Sigma^{*-}(p)$, in which real photon beams scatter off deuterons and produce kaons and Σ^* (1385)s while the proton is a spectator in the reaction. The kaon has strangeness +1 and isospin 1/2 with a z-component of +1/2 as shown in Figure 1.4. The baryon produced in this reaction is Σ^{*-}, which has strangeness −1 and isospin 1 with a z-component of −1 and is a member of the baryon decuplet as shown in Figure 1.6. The Σ^{*-} decays strongly into $\Lambda\pi^-$ with a branching ratio of about 87.0% . The Λ, as the lowest-lying hyperon state shown in Figure 1.5, decays weakly into $p\pi^-$ with a branching ratio of about 63.9%.

1.3.1. Previous Measurement. There is only one published measurement on this channel by [10], which was done at the SPring-8 facility with the LEPS detector. The experiment detected the K^+ and π^- from the strong decay. The polarized photon beam energy ranging from 1.5 to $2.4GeV$ was incident on a 16-cm liquid deuteron target. A start counter (SC) made of scintillators was placed downstream after the target. A Cerenkov detector was used to veto e^+e^- pair production. The tracking system consists of a dipole magnet, wire chambers, and a time-of-flight (TOF) scintillator wall 4 meters away from the target, were used to detect charged particles. The resolution of TOF was about 150 ps and the momentum resolution about 6 MeV/c.

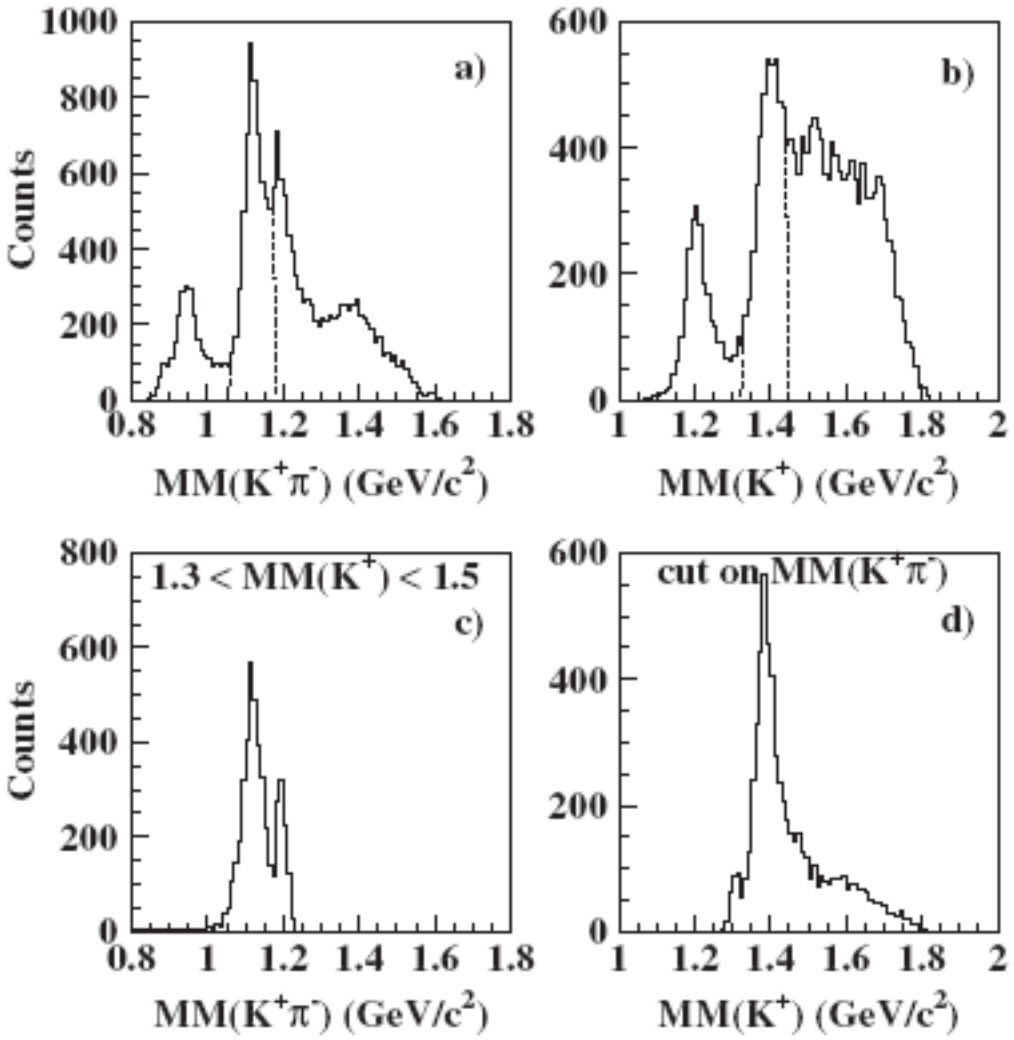

FIGURE 1.7. Mass spectra calculated using the missing mass technique for: (a) detected $K^+\pi^-$; (b) detected K^+ only; (c) same as (a) but cut on the $\Sigma\,(1385)$ peak shown by the dashed lines in (b); (d) same as (b) but cut on the Λ (1116)peak shown by the dashed lines in (a).

The photon energy was tagged from electron scattering through Compton backscattering of polarized laser light. The trigger was formed from the tagging electron, the SC, and a hit in TOF.

Because the detector does not have full solid angle coverage, the way to reconstruct the Σ^{*-} is to combine the information of the beam, target, and detected K^+ and π^-. The resulting missing masses of $K^+\pi^-$ and K^+ were calculated under the assumption that the spectator was at rest. The peaks of $\Lambda(1116)$ and $\Sigma^*(1385)$ are seen in part a

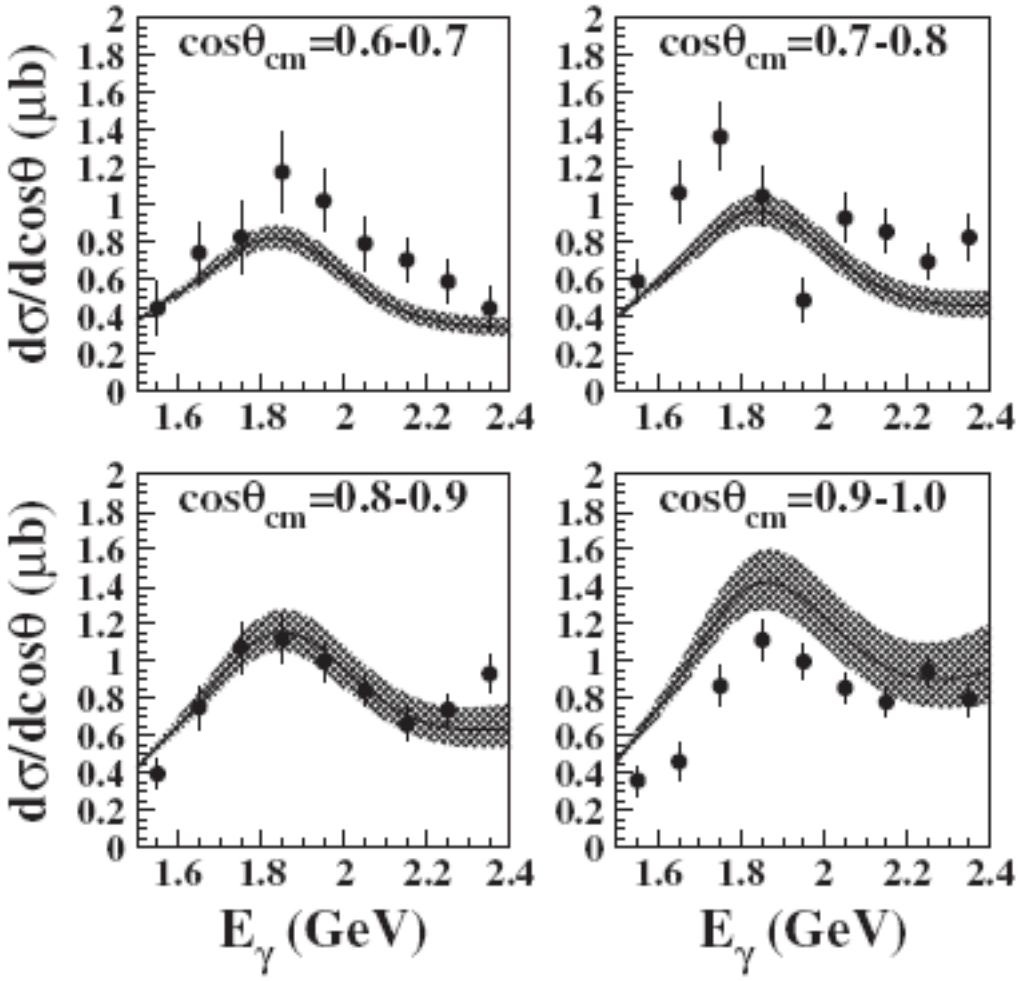

FIGURE 1.8. Differential cross sections as a function of photon energy. Each plot is for the angle bin in $cos\theta_K^{cm}$ as shown. The curves are from the model of [12] for the central angle and the shaded region extends over the given angular range.

and b of Figure 1.5. After cutting on the Σ and Λ, the same histograms with cleaner data sample were produced. The data was divided into nine bins according to the photon beam energy from 1.5 to 2.4 GeV. The yield was obtained by fitting the peak and subtracting the background channels produced from the hydrogen target. After simulation and reconstruction, further corrections were applied and the differential cross section was obtained, which is plotted in Figure 1.8 in comparison with the theoretical prediction [12]. Beam asymmetry and the resulting angular dependence

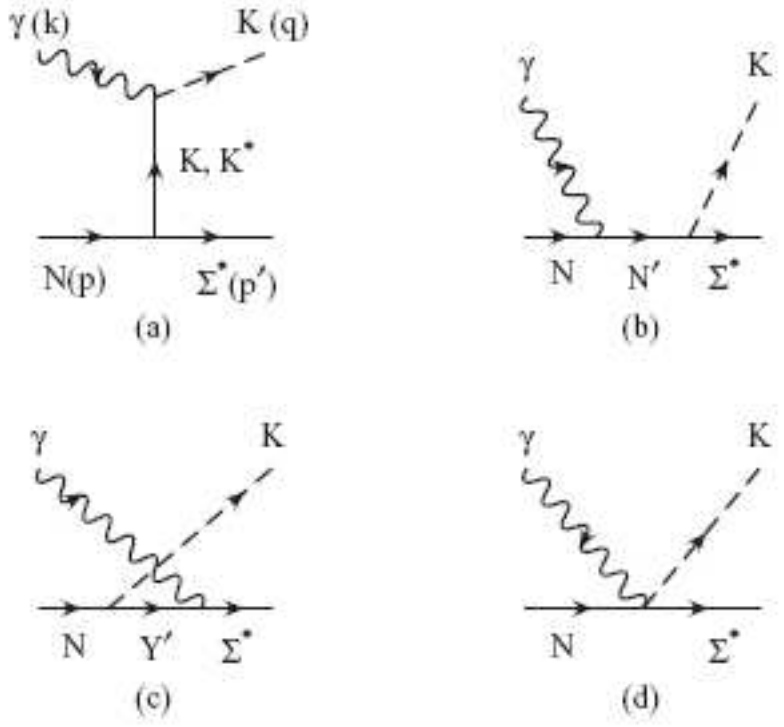

FIGURE 1.9. Feynman diagrams for $\gamma p \to K^+\Sigma^{*0}$. N' stands for the nucleon, Δ and their resonances, and Y' the Λ, Σ and their resonances.

were extracted, too. Since our experiment does not employ polarization information, I will neglect the discussion of their results.

1.3.2. Theoretical Calculation. There are not many theoretical calculations on this production channel. Oh et al. [12] calculated the cross section and other properties of $\gamma p \to K^+\Sigma^{*0}$.

The effective Lagrangian employed by Oh et al. [12] comes from the four Feynman diagrams in Figure 1.9, which are contributions from the t-, s-, and u-channels together with the contact term required by gauge invariance.

The t-channel has two exchange mesons considered in the model; one is K exchange and the other is K^* exchange. The $KN\Sigma^*$ coupling is obtained by applying $SU(3)$ flavor symmetry to $\pi N\Delta$ coupling.

$$\frac{f_{\pi N\Delta}}{M_\pi} = -\sqrt{6}\frac{f_{KN\Sigma^*}}{M_K} \tag{1.21}$$

Accordingly, $f_{KN\Sigma^*}$ is obtained as -3.22. The proton's empirical anomalous magnetic moment, $\kappa_p = 1.793$ is used. The magnetic moment of Σ^* is taken from the quark model prediction of 0.36. For K^* exchange, there are in general three terms as

$$\begin{aligned} L_{K^*N\Sigma^*} = & \quad \tfrac{ig_1}{2N_N}\bar{K}^{*\mu\nu}\bar{\Sigma}^*_\mu \tau\gamma_\nu\gamma_5 N \\ & + \tfrac{g_2}{(2M_N)^2}\bar{K}^{*\mu\nu}\bar{\Sigma}^*_\mu \tau\gamma_5\partial_\nu N \\ & - \tfrac{g_3}{(2M_N)^2}\partial_\nu\bar{K}^{*\mu\nu}\bar{\Sigma}^*_\mu \tau\gamma_5 N + H.C. \end{aligned} \tag{1.22}$$

where K^* is an isodoublet. The coupling constant g_1 is obtained from $SU(3)$ relation to $g_1^{\rho N\Delta}$ and obtained as -5.48 when $g_1^{\rho N\Delta} = 5.5$. The other two coupling constants remain free parameters.

The u-channel diagram shown in Figure 1.9 contains an intermediate hyperon. Here only the Λ ground state is considered. There are two terms in the $\Sigma^*\Lambda\gamma$ coupling as

$$\begin{aligned} L_{\Sigma^*Y\gamma} = & \quad -\tfrac{ief_1}{2M_Y}\bar{Y}\gamma_\nu\gamma_5 F^{\mu\nu}\Sigma^*_\mu \\ & - \tfrac{ef_2}{(2M_Y)^2}\partial_\nu\bar{Y}\gamma_5 F^{\mu\nu}\Sigma^*_\mu + H.C. \end{aligned} \tag{1.23}$$

and Y stands for a hyperon with spin-1/2 in general and Λ here. The radiative decay of $\Sigma^* \to \Lambda\gamma$ and the ratio of two helicity amplitudes, $A_{3/2}/A_{1/2} \simeq 1.82$, are used to obtain the $\Sigma^*\Lambda\gamma$ coupling constants, $f_1 = 4.52$ and $f_2 = 5.63$. The coupling $g_{KN\Lambda}$ is again obtained through $SU(3)$ symmetry, and the value is -13.24.

The s-channel incorporates excitation of nucleon and Δ resonances. Resonances with total spin $j \leq 5/2$ are included. They are grouped into two categories. One includes those listed in Particle Data Book (PDG) and the other the so-called "missing states". The PDG resonances included here are $S^*_{11}(2090)$, $D^{**}_{13}(2080)$, $D^{**}_{15}(2200)$,

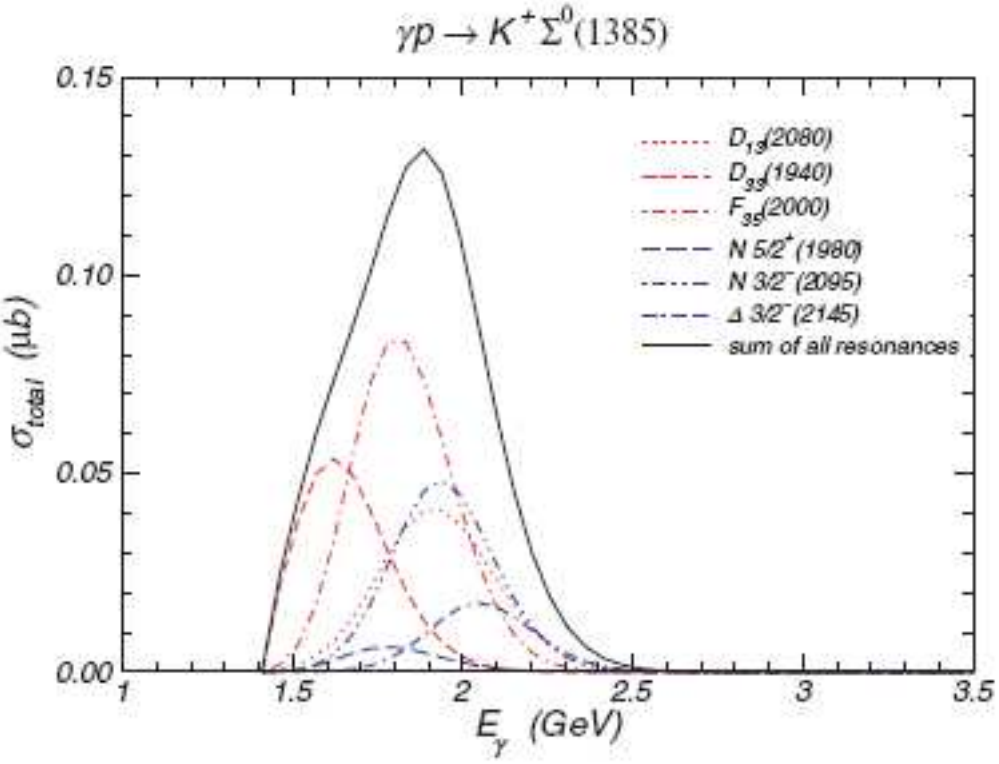

FIGURE 1.10. (Color online) Contributions from various resonances to the total cross section for $\gamma p \to K^+\Sigma^{*0}(1385)$.

$D^*_{33}(1940)$, and $F^{**}_{55}(2000)$. The "missing resonances" included here are $N^-_{\frac{3}{2}}(2095)$, $N^+_{\frac{5}{2}}(1980)$ and $\Delta^-_{\frac{3}{2}}(2145)$. The relative contributions are shown in Figure 1.10.

1.4. SUMMARY

Mass, as a physics term, is known by almost every one. However, the origin still remains unsolved, which is to say it is still not fully understood. The mass of visible matter, as only about 4% of the universe, is generated by QCD and fairly well calculated by LQCD with chiral extrapolation.

LQCD cannot calculate the mass of all baryons. Moreover, there are still "missing resonances", which means that even the existence of some baryons is still in question. The constituent quark model can describe the spectrum of those baryons and mesons that are detected very well. However, there is still a large discrepancy between the

number of excited nucleons predicted by the quark model and those found experimentally. One possible way of solving this problem is to study KY production, like the channel in this work.

The hyperon Σ^{*-} is a member of the baryon decuplet, and therefore, it is a good way to test the $SU(3)$ symmetry by comparing its cross section and other physical observables with theoretical predictions.

This work could and should be one of the continuous steps to understand QCD, the strong interaction, and how the visible mass is generated.

Chapter 2

Experiment and Detector

The data presented here was obtained in Hall B at Thomas Jefferson National Accelerator Facility (TJNAF), also known as Jefferson Laboratory or JLab, in Newport News, Virginia. A picture of it is shown in Figure 2.1. There are currently three experimental halls, denoted as A, B and C. The Continuous Electron Beam Accelerator Facility (CEBAF) can deliver a high-intensity beam to three experimental halls with mostly independent beam parameters simultaneously. A schematic layout is shown in

Figure 2.1. Picture of TJNAF.

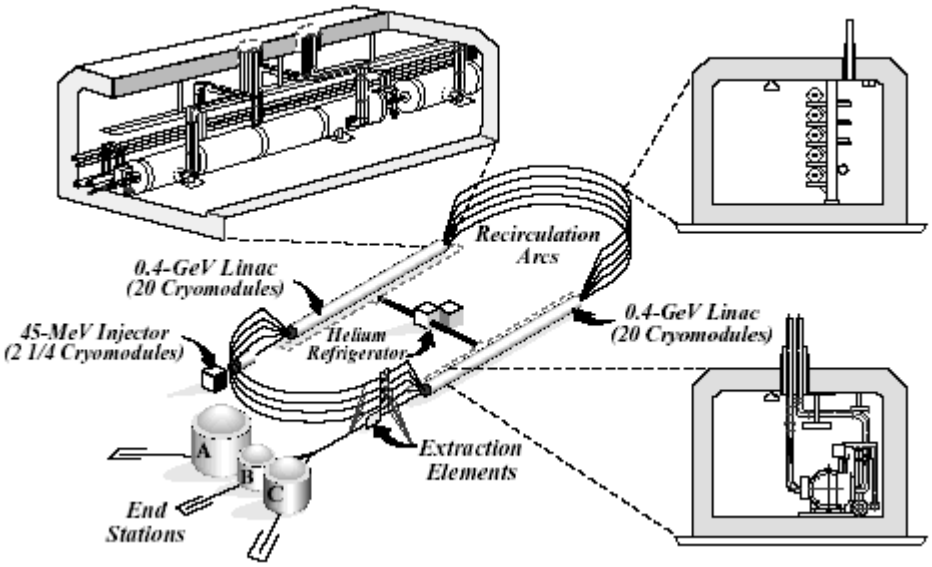

FIGURE 2.2. Layout of Thomas Jefferson National Accelerator Facility, showing injector, linear accelerators, recirculation arcs and three halls.

Figure 2.2. All of the three halls have fixed targets. However, Hall A and Hall C have also fixed-angle detectors dedicated for hadrons and electrons respectively. Whereas Hall B has a spherical detector of large acceptance covering a solid angle of almost 4π.

This experiment EG3 was done in Hall B as part of the search for the exotic Φ^{--} pentaquark state, by using the CEBAF Large Acceptance Spectrometer (CLAS). However, the experiment also provides a high statistics dataset for a number of interesting reaction channels, especially those production channels on the neutron. The electron beam of about 5.7 GeV collided on a radiator in the tagger system and generated a photon beam used in this experiment. The energy of the photon beam ranges from 1.15 to 5.5 GeV. The liquid deuterium target is 40 cm long and 4 cm wide. It is positioned 50 cm upstream of the CLAS detector center to increase the acceptance of highly energetic charged particles. The average incident beam intensity

was about 30 nA. A 40-day run time at high luminosity results in an overall luminosity $L \sim 10^{34} cm^{-2} s^{-1}$ and provides large statistics and the opportunity to investigate high-lying resonances.

2.1. Continuous Electron Beam Accelerator Facility

The CEBAF delivers electron beams to three experimental halls. The main advancement of the accelerator facility is the adoption of superconducting radio frequency (SRF) cavities. Before CEBAF, the usual cavities were made of copper. The electric resistance of the material heated the cavities up, which limit the acceleration gradient. With the usage of the SRF cavities, the accelerator can deliver "continuous", high-energy, and high intensity electron beams.

The electron beam starts from the injector. The electrons are generated by shining a pulsed laser on a GaAs photocathode and then accelerated to 45 MeV by going through 2 and 1/4 SRF cavities. The laser pulses generate electron bunches for each experimental hall every 2 ns. The injector system then cleanly separate the bunches before recirculating them through the linear accelerators (LINACs) of CEBAF Figure 2.2.

The basic element of a LINAC is the SRF cavities as shown in Figure 2.3. There are 168 SRF Niobium cavities in each LINAC. Each cavity is cooled with liquid Helium to 2K to maintain the superconductivity of the material. The RF electromagnetic standing waves in the cavities accelerate the electron beams. This acceleration is independent of the speed of the electron once they have reached the 45 MeV provided by the injector and hence mostly speed of light. The illustration is shown in Figure 2.4. There are two LINACs and each LINAC can accelerate the electron beam by 600 MeV, so that each electron will gain 1.2 GeV after one pass. The recirculation arcs shown in Figure 2.2 bend the electron beam in the loop. There are upto 5 recirculation corresponding to 5 passes. After that, each electron in the beam gains upto 6 GeV energy before entering each experimental hall by extraction elements Figure 2.2. This

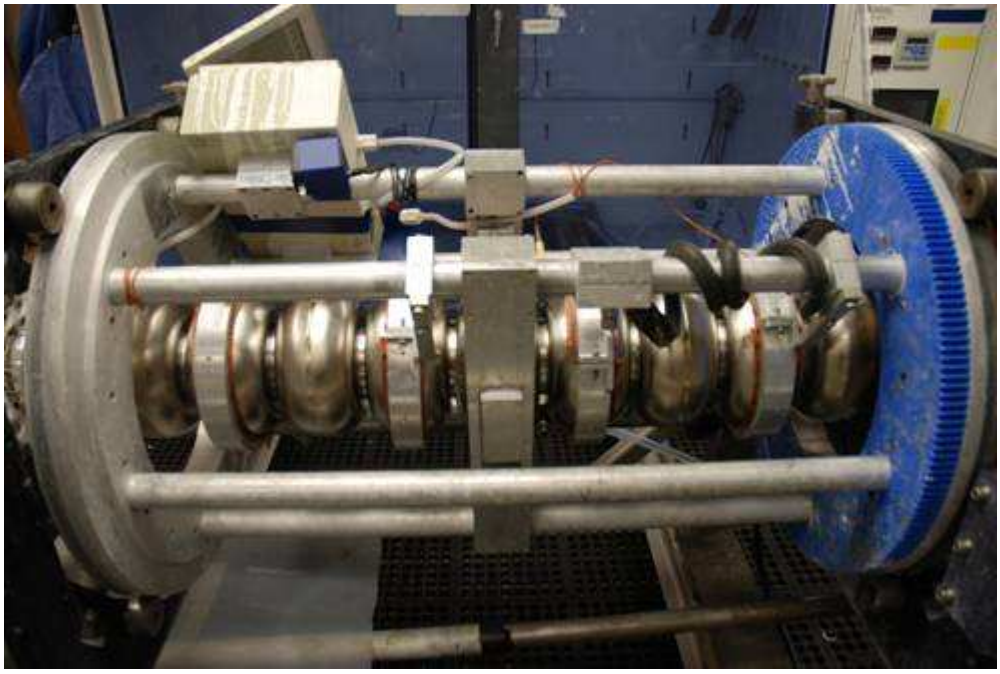

FIGURE 2.3. Picture of CEBAF's SRF cavities.

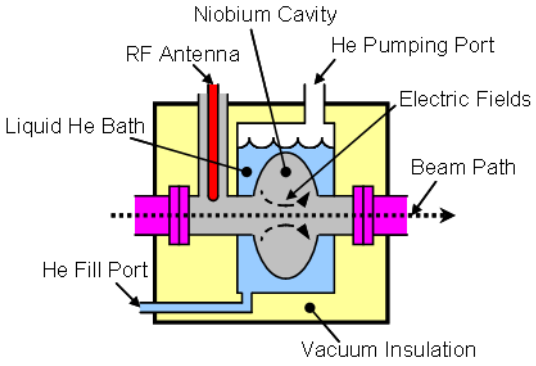

FIGURE 2.4. The acceleration gradient is provided by the electric field formed from standing waves.

acceleration process also helps to focus electrons in the beam so that each bunch has a width of only about several picoseconds.

2.2. The Photon Tagger

The experiments performed in JLab usually utilize two types of beams, electron and photon, corresponding to two types of reactions, electroproduction and photoproduction. However, CEBAF only delivers an electron beam. In order to convert it

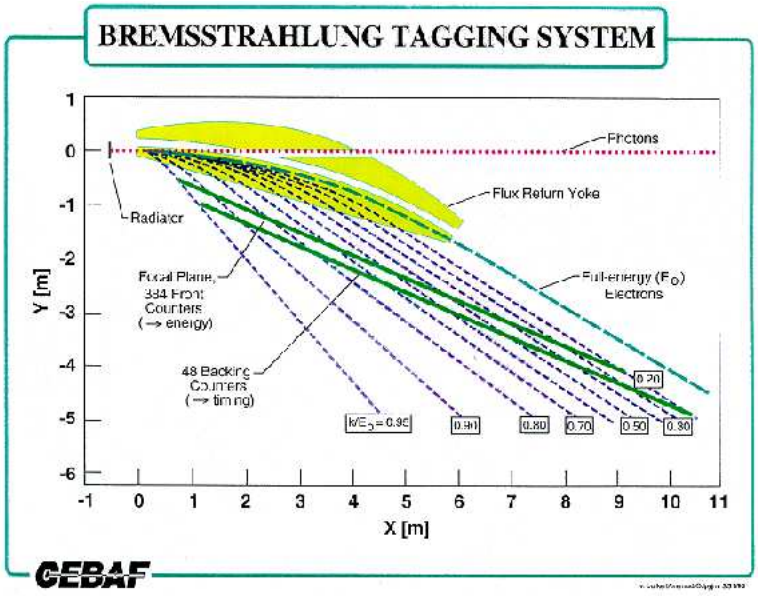

FIGURE 2.5. The schematic diagram of the tagger system in Hall B. The purple dashed line shows the trajectory of photons generated by bremsstrahlung of the electron beam. The cyan dashed lines are paths followed by recoil electrons. Each path corresponds to a fixed momentum of the recoil electrons.

into a photon beam, a photon tagger system is used. The system produces a photon beam by putting a gold foil radiator in the beam path. The electrons interact with the radiator and produce photons via bremsstrahlung. After passing through the radiator, the beam contains primary electrons, recoil electrons and radiated photons. A dipole magnetic field is used to bend the electrons out of the beam path, and photons remain traveling towards the target. The primary electrons are bent into the beam dump, and the recoil electrons are bent on two arrays of scintillation detectors. One set of them, referred to as E-counters, is used to detect the energy of the electron. The other set is used to measure the time when the electrons reach them. This time can then be adjusted by software calibration to the time when the radiated photon reaches the target.

The E-counters are used to determine the momentum of the recoiling electrons simply by selecting the electron's path (see Figure 2.5), because the path of electrons in the magnetic field is solely determined by the momentum. There are 384

E-counters. However, they are overlapping with neighboring counters. This arrangement improves the resolution of the momentum without increasing the size of the scintillators. The total number of logical energy channels becomes 767, rather than 384 E-counters. The E-counters are arranged so that each covers approximately the same energy range. The tagger system can detect recoil electrons that correspond to photons ranging from 20% to 95% of the incident electron beam energy. Therefore, the energy resolution of each logical energy channel is about 0.1% of the incident electron beam energy (Figure 2.5).

The signals from the T-counters are sent to the Master OR (MOR) and an array of FASTBUS TDCs after passing through discriminators. The MOR signal is part of the trigger system, which decides whether it should digitize data from the detectors and write it into the data stream or discard them. The TDC array digitizes the photon timing. The E-counter signals are also sent through a discriminator and then forwarded to a multi-hit TDC. The timing information of both E-counters and T-counters is sent to the data stream. The offline software can establish the timing coincidence between them and the corresponding logical energy channel.

The time resolution from the tagger system is good enough to find from which beam bunch the recoil electron comes. In the offline analysis, the time is corrected according to the beam bunch (RF correction), which is obtained from the accelerator and is the most accurate time information available in the data. It is also corrected to the time when the photon reaches the target in order to serve as the start time of the event.

2.3. The CLAS Detector

The CEBAF Large Acceptance Spectrometer (CLAS) is a spherical, multiple-component detector system used to detect particles produced by the interaction of the electron or photon beam with a typically cryogenic target placed in the beam

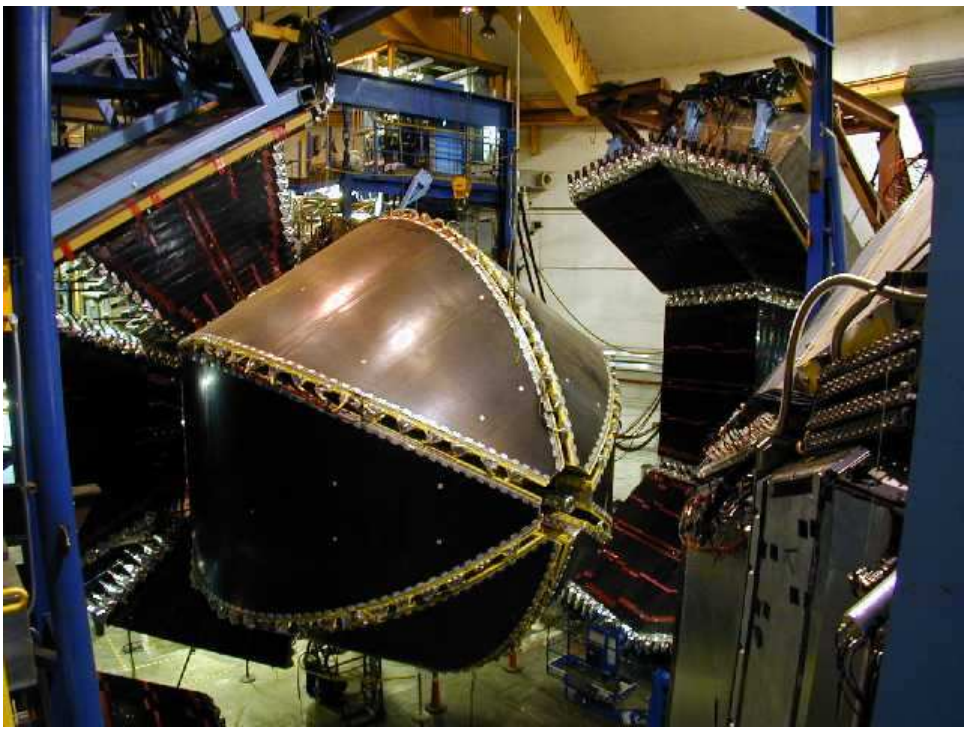

FIGURE 2.6. A picture of the CLAS. Inside you can see is the drift chamber (DC), and the black peeled away is the time-of-flight detector (TOF).

path near the center of the CLAS detector. A picture of CLAS is shown in Figure 2.6. The main components of CLAS include the start counter (ST), magnetic torus, drift chambers (DC), time-of-flight scintillators (TOF or SC), Cerenkov counters (CC) and electromagnetic calorimeters (EC). The charged particle path is bent in the magnetic field generated by the torus and detected by DC via ionization processes. The TOF detectors record the time when the charged particles reach them. In our photoproduction experiment, the TOF time together with the tagger time or ST time tell the time interval each particle travels through the CLAS detector. The momentum, speed, and trajectory of charged particle are fitted by using the DC and timing information. An illustration of the main components is shown Figure 2.7. For a detailed description of the CLAS detector, please refer to [11].

2.3.1. Superconducting Toroidal Magnet. The toroidal magnet is an essential component of the CLAS detector. The magnetic field generated by the torus

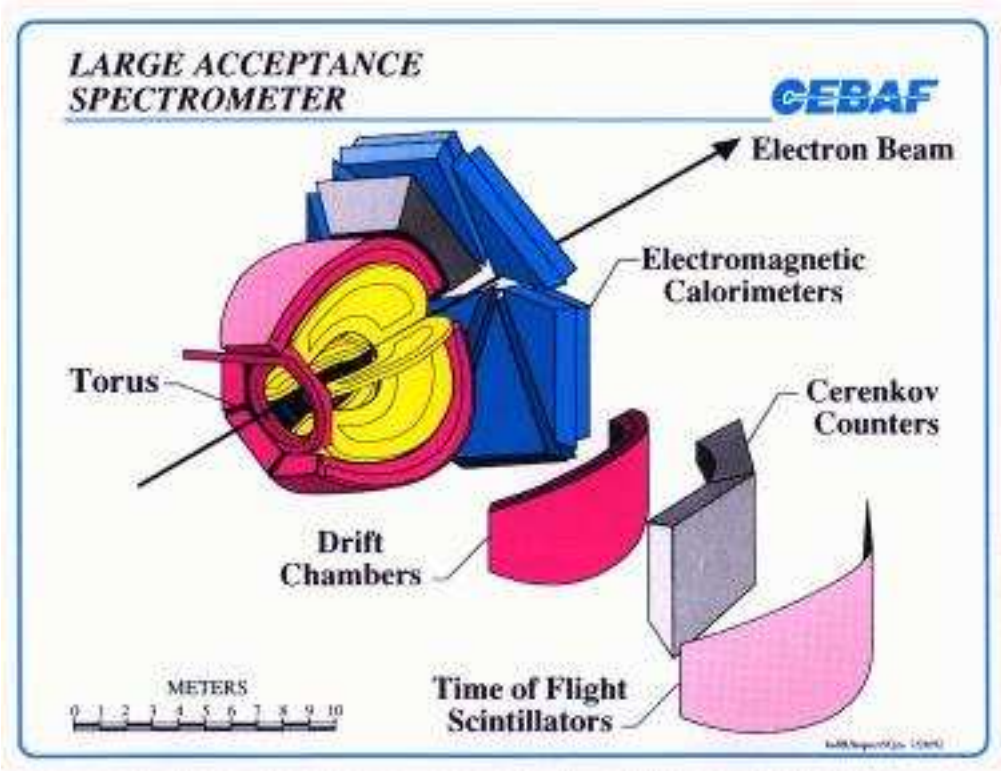

FIGURE 2.7. Illustration of CLAS and its subsystems.

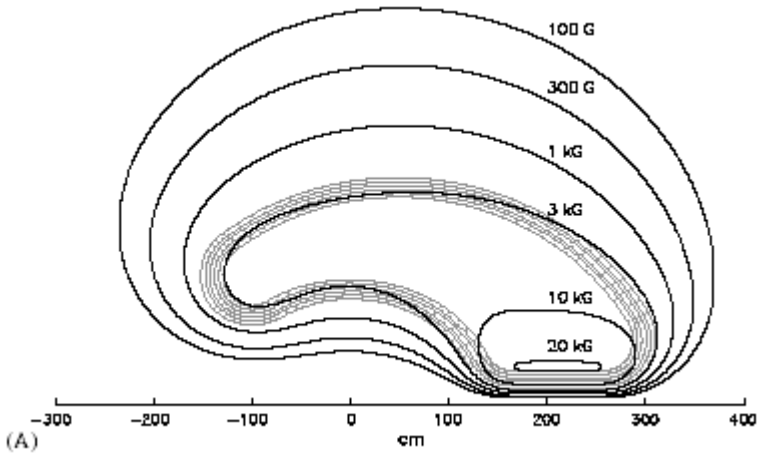

FIGURE 2.8. The magnetic field generated by a kidney-shaped torus at a given azimuthal angle.

bends charged particles within CLAS. The path is recorded by the drift chamber and the information is used to fit the trajectory and momentum of each particle. The field generated by a single torus is shown in Figure 2.8.

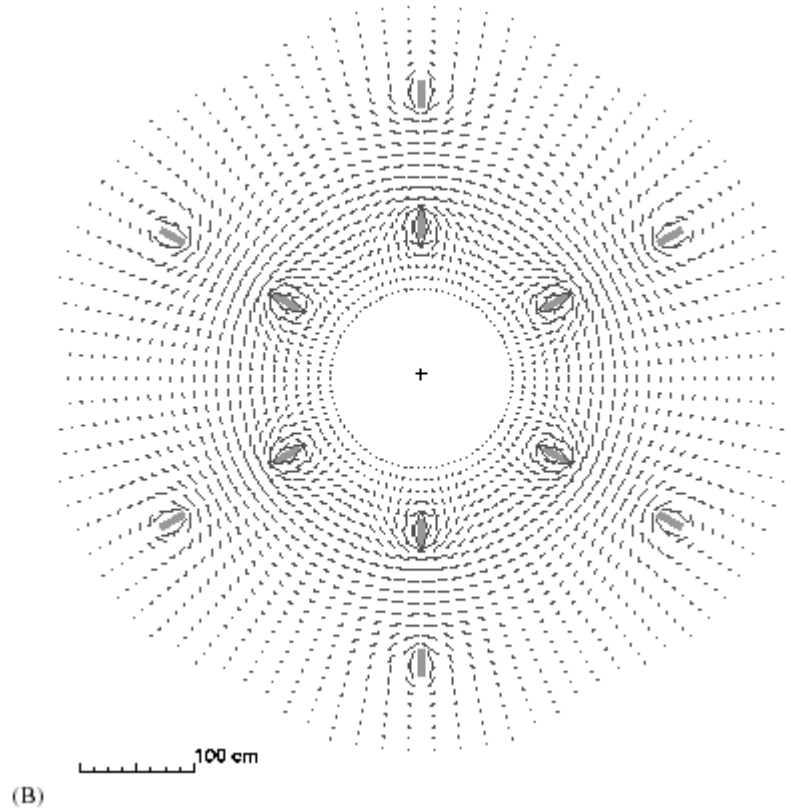

FIGURE 2.9. The azimuthal mapping of the field generated by torus.

CLAS has six kidney-shaped superconducting coils, which are azimuthally symmetrically placed to generate an azimuthally symmetric field Figure 2.9. The inverse field configuration used by EG3, bends negatively charged particles outwards away from the beam line and positively charged particles inwards. The peak current the magnet can support is 3861 A, resulting in a maximum field strength of 3.5 T. However, during the EG3 run period, the current was limited to -1932 A. The negative sign denotes the inverted field. The field intensity affects the detection of particles with different momenta. The higher energetic particles require higher fields to bend them and to get sufficient resolution. However, too high fields may bend low energetic particles too much to be detect. The lower field is optimal for the kinematic range in which EG3 is interested.

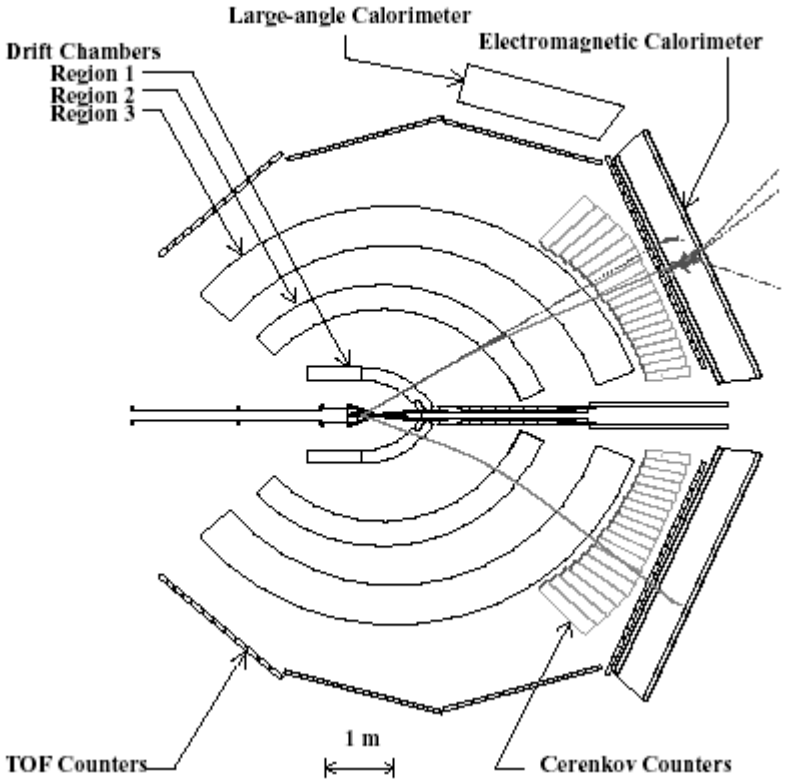

FIGURE 2.10. A cut view of the CLAS detector. The three regions of DC are labeled. Samples of trajectories are shown.

2.3.2. Drift Chambers. The drift chamber (DC) generates the signals caused by the ionization of charged particles passing through. Together with the information of the magnetic field generated by the toroidal magnet, the trajectory and momentum of the particle can be reconstructed. The drift chamber is divided by the torus coils into six sectors . The drift chamber has three separated regions Figure 2.10. Region 1 is located inside the torus coils, where there is almost no magnetic field. Region 2 is located directly on the side of the coils, where the magnetic field is the strongest. Region 3 is positioned outside of the torus coils, where the magnetic field is weak again. An azimuthal view is shown, and six sectors are visible in Figure 2.11, which can be compared with Figure 2.9.

Each of the three regions is divided into two superlayers. One has the wire axially oriented to the magetic field direction. The other has the wire oriented at a 6^o stereo

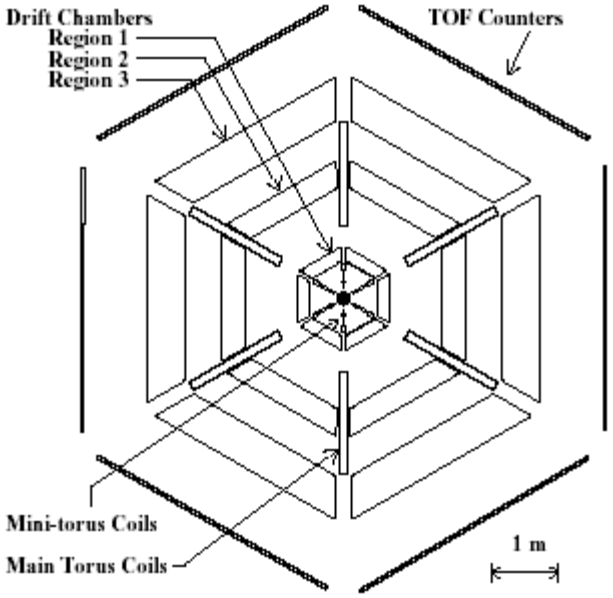

FIGURE 2.11. The azimuthal view of the CLAS detector. The three regions of DC are labeled, and the six sectors are shown. The corresponding magnetic field configuration is shown in Figure 2.9.

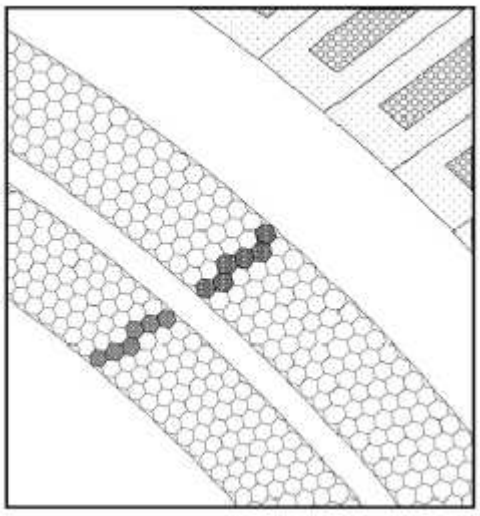

FIGURE 2.12. An example of a track segment in region 3.

angle. The combination is supposed to tell the direction of the particle in three-dimensional space. Each superlayer in region 2 and 3 consist of six layers of hexagonal drift cells, while there are eight layers in region 1 divided into 2 superlayers with four layers each. Each layer of drift cells is offset by half a cell width. Each cell has a

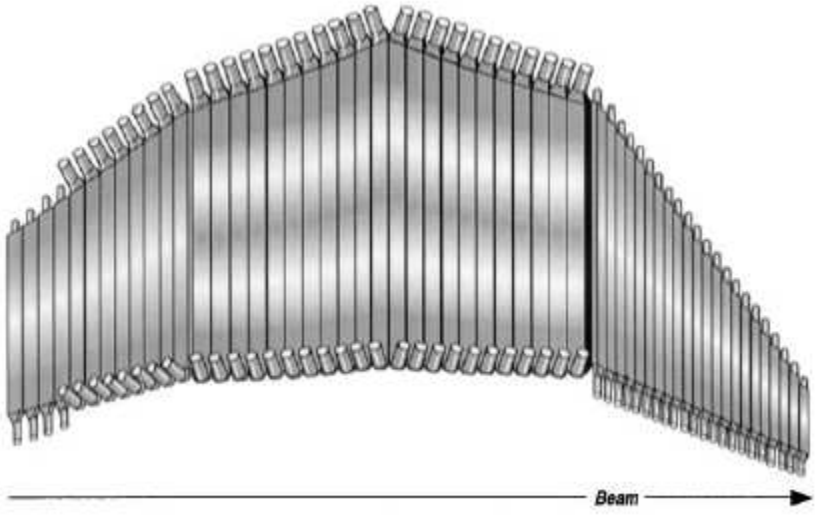

FIGURE 2.13. Diagram of the time-of-flight scintillator shell from one CLAS sector.

sense wire at the center surrounded by six field wires. The sense wires are positively charged, and the field wires are kept negative high voltage. The diameter of drift cells in region 1, 2 and 3 are 0.7, 1.5 and 2.0 cm, respectively. The electrons generated by the ionization caused by the passing charged particle drift onto the sense wire. The signal is passed onto the preamplifier and then to the amplifier discriminator boards (ADBs). It is finally delivered to a TDC to obtain the timing information. The drift chamber gas mixture is 90% Argon and 10% CO_2 to optimize its ionization properties and maintain non-flammability. One example of a trajectory in region 3 is shown in Figure 2.12.

2.3.3. Time-of-Flight Scintillators. The time-of-flight detector is one of the outermost detectors. It measures the flight time of particles from the target to the TOF wall. The TOF detector subsystem includes scintillation bars, photomultiplier tubes, voltage dividers and electronics. The system is divided into six sectors similar to the drift chamber system. The scintillator wall in each sector has four panels and a total of 57 bars of varying lengths and widths (see Figure 2.13). Each bar is 2 inches thick to maximize the detection efficiency of minimum ionizing particles. The signals

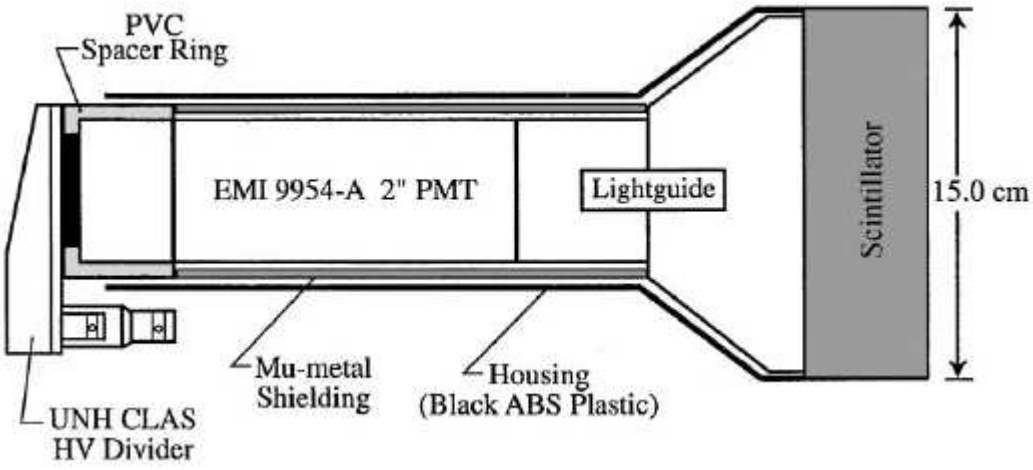

FIGURE 2.14. Diagram of a PMT system on the end of a TOF scintillator at forward angle.

from the scintillators are collected and amplified by photomultiplier tubes (PMTs) mounted at each end (see Figure 2.14). The timing information from TOF is one of the vital pieces to reconstruct the particle identification.

2.3.4. Triggering and Data Acquisition. Every detector subsystem has its own independent electronics to collect signals. However, a signal does not mean a real physics event. There are a lot of accidental signals such as signals caused by cosmic rays and electronic noise. The trigger system helps to determine when it is an interesting physics events. Once the trigger system gives a signal, the data acquisition system (DAQ) collects the signals from all the subsystems and writes them to storage media.

The EG3 experiment used photon beam ranging from 1.15 to 5.5 GeV. All tagger counters are on, but only T-counters 1 to 20 are in the trigger system contributing to MOR. The runs from December 2004 to February 2005 are separated into two groups. One is before the Christmas 2004 and the other is after. The trigger system requires signals from at least three sectors of the CLAS detector, which is indicated by the trigger bit 6, or signals from at least two sectors (reduced by a pre-scale factor), which is indicated by the trigger bit 5. A demonstration is shown in Figure 2.15, in which

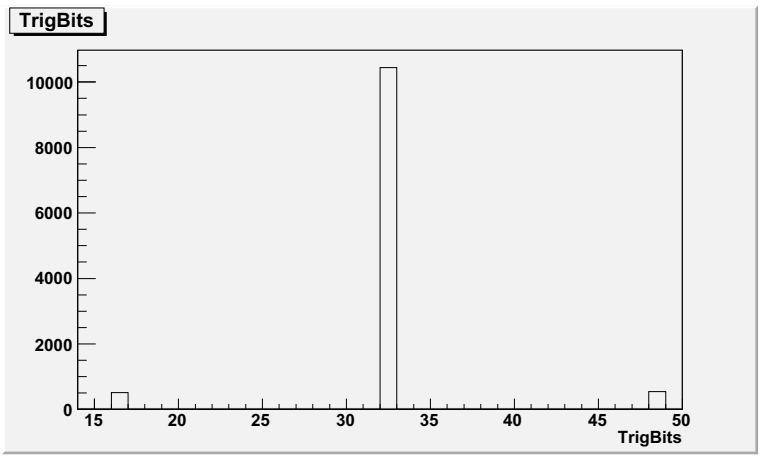

FIGURE 2.15. Distribution of events of different trigger bits. Events around 16 are those of trigger bit 5 on and trigger bit 6 off; around 32 are of bit 6 on and bit 5 off; around 48 are of both bits on.

16 on x axis indicates bit 5 only, 32 means bit 6 only and 48 shows both bits are on. The runs before Christmas did not put start counters into the timing requirement, and the runs after Christmas did.

Chapter 3

Event Selection

The EG3 dataset was collected from December 2004 to February 2005 by the CLAS collaboration. After calibration of the detector, a cooking process was done by Hovanes Egiyan. The process is to collect information from each detector subsystem and combine them together to obtain information about scattered particles. During this process, the photon flux (gflux) was calculated. It reflects the dependence of the photon flux on the photon energy. Moreover, the efficiency of the tagger system is already included.

This chapter describes the steps after cooking. It is highly dedicated to the reaction channel of interest.The reaction is quasi-free photon scattering off neutrons by producing $K^+\Sigma^{*-}(1385)$, $\gamma d \to K^+\Sigma^{*-}(p)$. The Σ^{*-} decays into $\Lambda\pi^-$ and Λ into $p\pi^-$. Therefore, the final particles are $K^+p\pi^-\pi^-$.

The purpose of event selection is to determine a series of conditions, under which a good data sample leading to an error-controlled cross section can be extracted.

3.1. Excluded Runs

Data taking in Hall B is grouped into runs. The EG3 runs are from December 6th 2004 to February 1st 2005. Run numbers are from 45255 to 46351. The first good run starts at 45552. The runs before it are mostly cross-check or optimization run or questionable for other reasons. Most good runs are using a beam current of 30 nA and there are four high luminosity runs at 35 nA. However, they are treated the same in the analysis process, because the normalization is done on the photon flux, which automatically take varying beam currents into account. A good run query program

can be obtained by doing the following as ordered: cvs co eg3_runs, cd eg3_runs, make lib, make exe, eg3_runs. The data is stored in Dbhost "mysql://clasdb.jlab.org" with Dbname "eg3_offline", DbTabl1 "Pass2v1", and DbTabl2 "GoldenRuns". Compared with the all-cooked-run list, the golden-run list has all 15 hydrogen runs removed and 8 bad deuteron runs removed. The golden runs are listed below: 45552, 45553, 45554, 45555, 45556, 45557, 45558, 45563, 45566, 45568, 45569, 45570, 45571, 45572, 45576, 45577, 45578, 45579, 45580, 45581, 45582, 45598, 45599, 45600, 45601, 45602, 45603, 45605, 45606, 45607, 45608, 45609, 45612, 45613, 45614, 45621, 45622, 45623, 45624, 45625, 45626, 45627, 45804, 45807, 45808, 45809, 45810, 45811, 45812, 45814, 45815, 45816, 45817, 45818, 45847, 45848, 45851, 45852, 45860, 45862, 45863, 45864, 45866, 45868, 45869, 45870, 45872, 45873, 45874, 45876, 45891, 45893, 45894, 45895, 45896, 45897, 45902, 45903, 45904, 45905, 45906, 45907, 45911, 45912, 45913, 45914, 45916, 45917, 45918, 45919, 45920, 45921, 45922, 45923, 45924, 45925, 45926, 45927, 45928, 45929, 45930, 45931, 45932, 45933, 45934, 45935, 45936, 45937, 45938, 45939, 45942, 45943, 45944, 45945, 45946, 45947, 45948, 45976, 45977, 45978, 45981, 45983, 45984, 45985, 45986, 45987, 45988, 45993, 45995, 45996, 46000, 46001, 46002, 46003, 46004, 46005, 46009, 46011, 46012, 46013, 46014, 46015, 46016, 46017, 46018, 46019, 46020, 46021, 46022, 46023, 46024, 46025, 46028, 46029, 46030, 46035, 46036, 46037, 46038, 46046, 46047, 46057, 46058, 46062, 46063, 46064, 46065, 46066, 46069, 46071, 46072, 46073, 46074, 46077, 46078, 46085, 46086, 46087, 46088, 46089, 46093, 46094, 46096, 46097, 46098, 46099, 46100, 46101, 46104, 46113. The runs from 45552 to 45627 have been performed before Christmas 2004 and the rest after. There is a change on the trigger condition as described in 2.3.4.

3.2. Inefficient T-Counter Cut

The tagger system serves two purposes. One is to measure the properties of the recoil electrons to tag the energy and time of the radiated photons. The other is to serve as input to the master-or signal(MOR). The latter function is part of the trigger

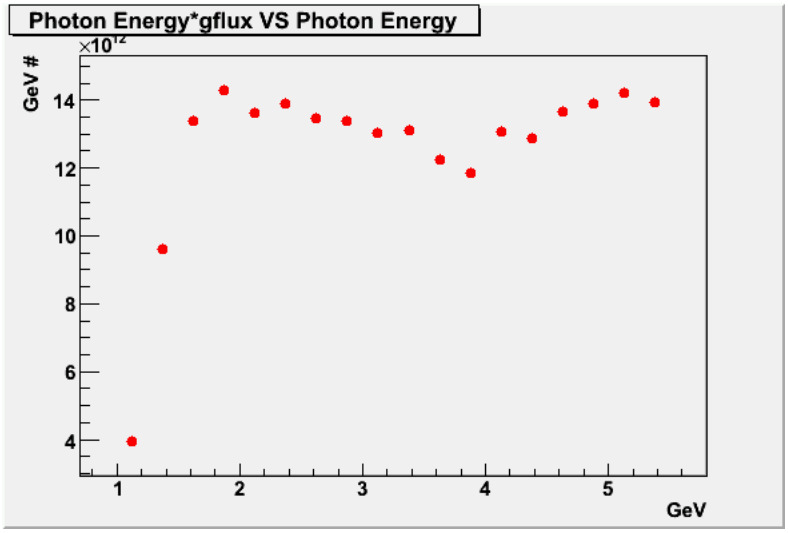

FIGURE 3.1. The product of photon flux and photon energy versus photon energy. The deviation from a flat line indicates the existence of T-counter inefficiencies. A cut around 1.5 GeV is applied according to this plot.

system. The typical yield of the bremsstrahlung photons is inversely proportional to the energy of the photons. The photon flux obtained has the efficiency included, so that the product of the photon flux and photon energy reflects the efficiency of the tagging system. This product versus photon energy is shown in Figure 3.1. If the detector system is working perfectly, then the product yields a flat line indicating that the efficiency is 100%. The deviation from that flat line implies the inefficiency dependency on the photon energy. This dependency can only come from hardware linking to T- and E-counters. There is a dramatic fall in the low energy region. This requires the first two data points of Figure 3.1 to be cut away. This cut applies to those T-counters corresponding to photon energies smaller than 1.5 GeV.

3.3. PARTICLE IDENTIFICATION

3.3.1. Start Time Determination and Photon Selection. After detector calibration and cooking, the particle identification (PID) is usually the first thing to check. However, the EG3 experiment, as the first CLAS experiment that pushed the luminosity to the currently achievable limit, has a high-intensity beam, which gives

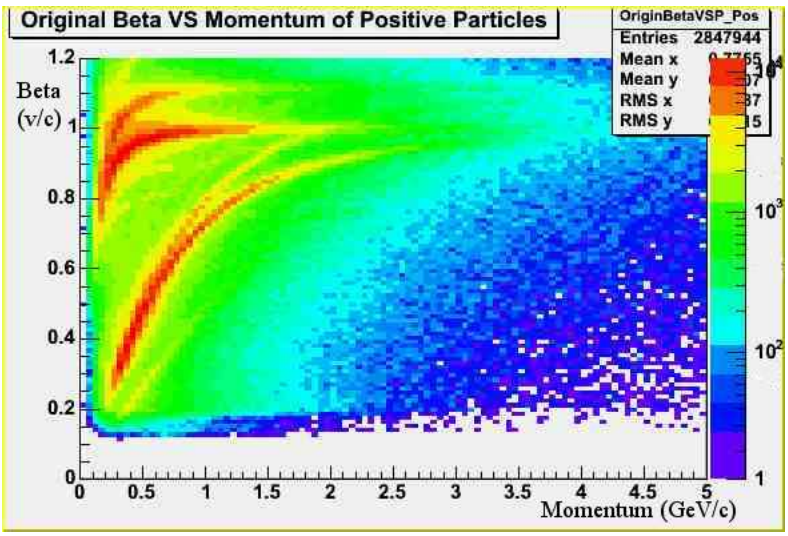

FIGURE 3.2. Beta versus momentum of positively charged particles from the result of standard CLAS offline software. The color is in log scale. Many side bands are visible. No clear band of K^+ is seen.

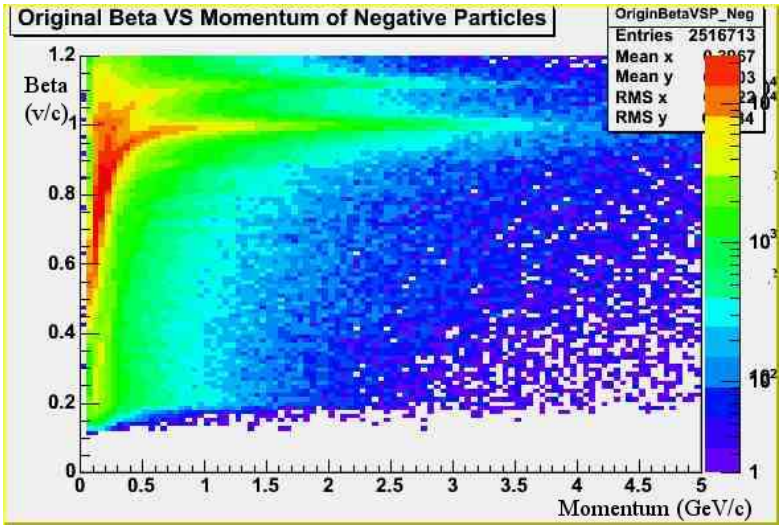

FIGURE 3.3. Beta versus momentum of negatively charged particles from the result of standard CLAS offline software. The color is in log scale. Many side bands are visible.

the opportunity to study events outside the triggered photon energy range. On the other hand, it also causes problems in particle identification, because there are too many photons recorded in each event. The standard CLAS offline software does not give satisfactory results as shown in Figure 3.2 and Figure 3.3. A channel-specified PID method was developped in this work by requiring that two π^-s have a consistent

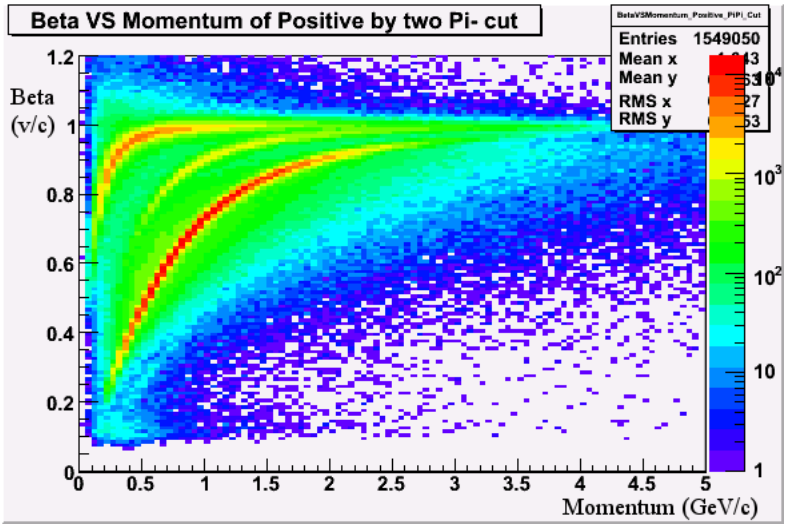

FIGURE 3.4. Beta versus momentum of positively charged particles from the new PID method. The color is in log scale, and bands of pions, kaons and protons are clearly seen.

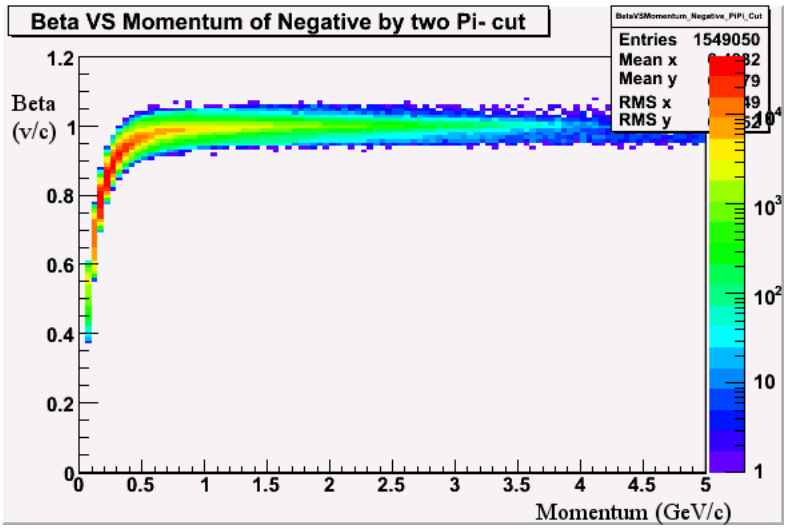

FIGURE 3.5. Beta versus momentum of negatively charged particles from the result of the new PID method. The color is in log scale, and only pions are selected.

vertex time, which leads to much better results as shown in Figure 3.4 and Figure 3.5. The method requires two negatively charged particles reconstructed by the standard cooking software and assumes both of them are π^-. The start time at the target center is calculated from the TOF time, vertex position, momentum, and trajectory

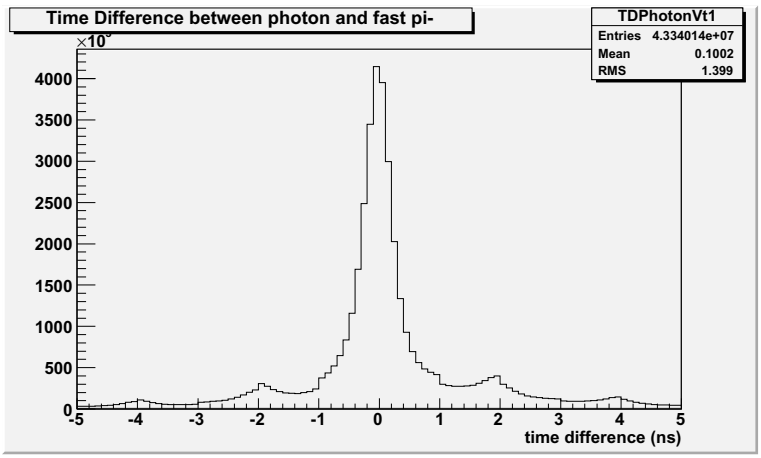

FIGURE 3.6. The difference between the start time of the selected photon and the vertex time of the faster pion.

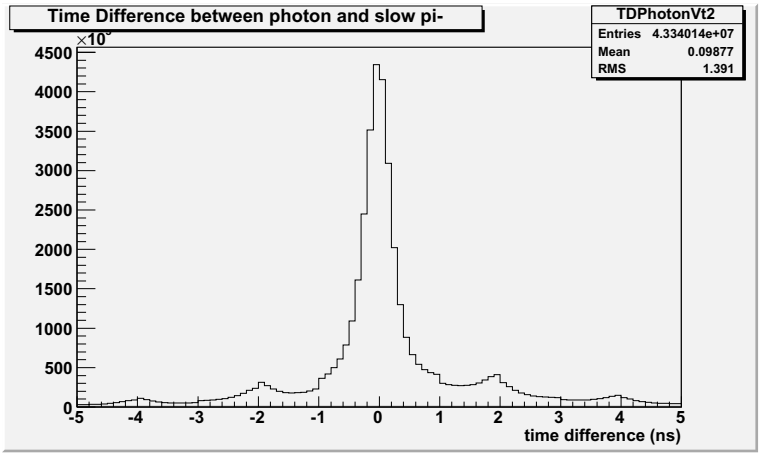

FIGURE 3.7. The difference between the start time of the selected photon and the vertex time of the slower pion.

length by the cooking software assuming the mass of π^-,

$$T_{tc} = T_{TOF} - \frac{l_{track}}{\beta c} - \frac{Z_{vt} - Z_{target}}{c}, \tag{3.1}$$

where T_{tc} is the start time at the target center, T_{TOF} is the TOF time of the particle, l_{track} is the trajectory length, $\beta = \frac{v}{c}$ is calculated from the momentum and mass of the π^-, Z_{vt} is the vertex position and Z_{target} is the target position, which is shifted by -50 cm. The photon, whose time at the target center is closest to the time T_{tc}, is selected according to the two negative charged particles, respectively. The time difference between the photon selected and the faster π^- is plotted in Figure 3.6, and

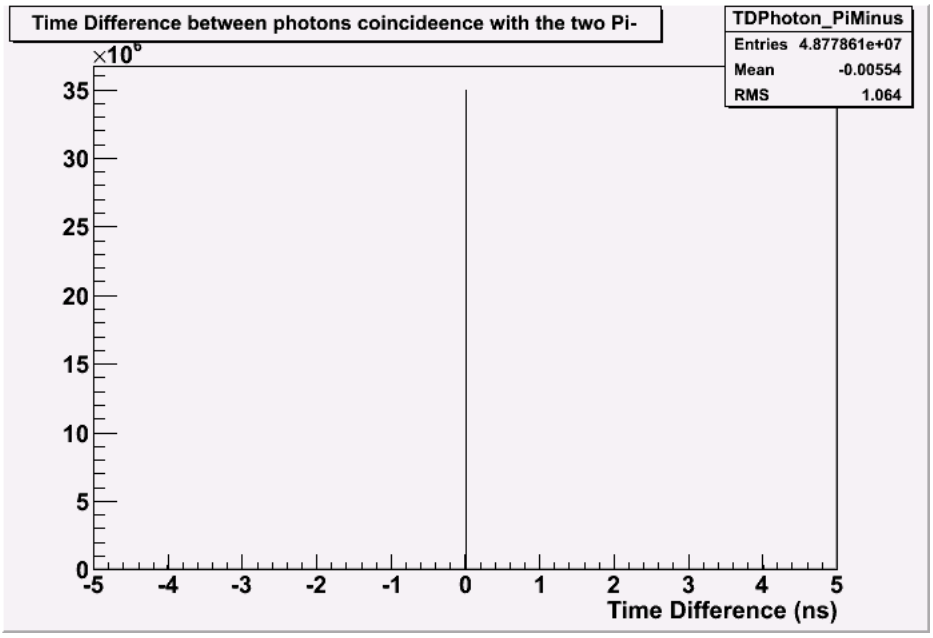

FIGURE 3.8. The time difference between the two selected photons. The central peak is so strong that the side peaks are invisible in this linear scale.

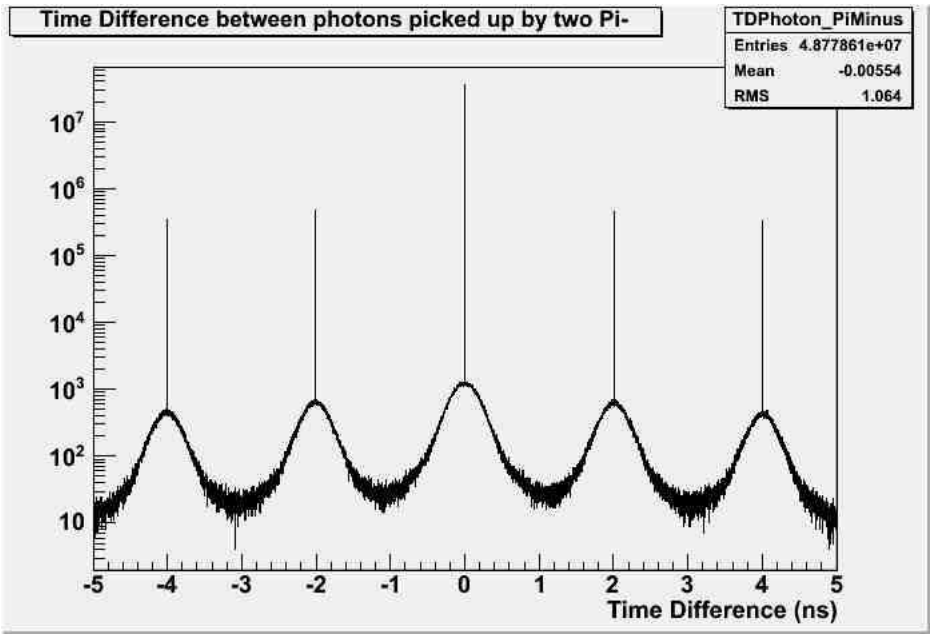

FIGURE 3.9. The time difference between the two selected photons in log scale. The background in the central peak is estimated as 1.5% from the side peaks.

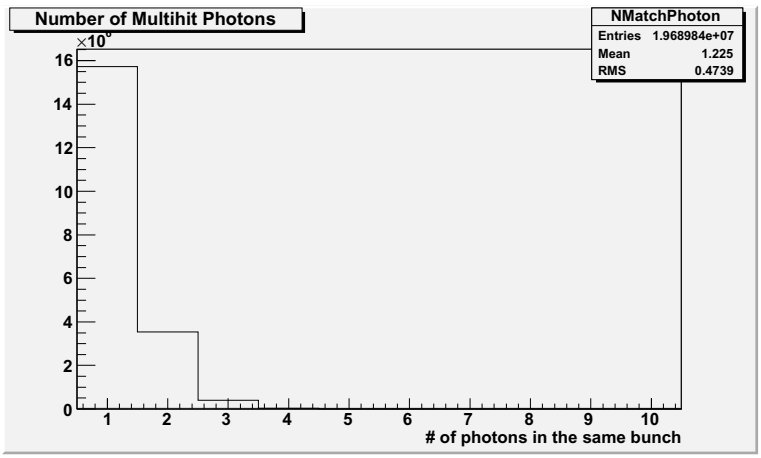

FIGURE 3.10. The number of photons in the beam bunch corresponding to the event start time. This shows that the ratio of events of multiple hits to those of no multiple hits is about 25%.

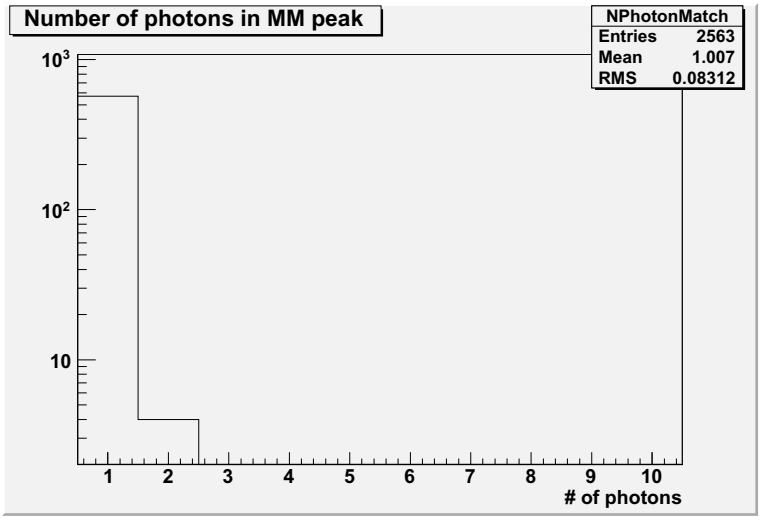

FIGURE 3.11. The number of photons in the beam bunch corresponding to the event start time and also giving the correct missing mass within 3σ cut. The ratio of multiple photons is negligibly low.

the similar histogram of the slower π^- in Figure 3.7. The time difference of these two photons is shown in Figure 3.8, and in the peak at zero, the photons selected according to the two pions are in the same beam bunch in most events. The photons in the central peak are kept and the rest are thrown away. In order to study the introduced error, the same histogram is plotted in log scale and shown in Figure 3.9. The background in the central peak estimated from the side peaks is about 1.5%.

3.3.2. Multiple Photon Hits. The beam intensity of EG3 is so strong that there are more than one electron that generate bremsstrahlung photon evens in one beam bunch (see Figure 3.10). Photons from different bunches can be distinguished by the process described before 3.3.1. However, the pure-timing method cannot distinguish those photons from the same bunch, since they correspond to the same start time. However, these photons usually have different energies. It is very unlikely that they have very close energy. Therefore, a selection based on the missing mass is applied so that the photon that is in time and gives the closest missing mass to spectator proton is selected. The error of this method is studied by plotting the number of photons that satisfy both the timing and energy requirement. The energy requirement is that the missing mass calculated from each photon energy must be within 3σ of the spectator peak. The histogram is shown in Figure 3.11, and the ratio of multiple-photon to single-photon events is below 0.1% and hence negligible in this study.

3.4. The Reconstruction of Λ

When analyzing the $K^+\Sigma^{*-}$ channel, the only interesting events are those with two positive charged particles and two negative charged particles. This feature is already used to select the photon as demonstrated above 3.3.1. Then events with $K^+p\pi^-\pi^-$ are selected. The invariant mass of the $p\pi^-$ pair, whose invariant mass is closer to the $\Lambda(1116)$ mass, is shown in Figure 3.12. A Gaussian distribution is used to fit the peak. The fitted peak is at 1.116 GeV with a width of 1.8 MeV. Events within a 3σ cut around the peak position are selected as candidates for physics events.

After this cut, the invariant mass of $\Lambda\pi^-$ is calculated for each event and plotted versus the missing mass of all detected particles, $K^+p\pi^-\pi^-$, in Figure 3.13. The events in the hot spot at the cross point of the two straight lines are mostly the physical events of the production channel studied.

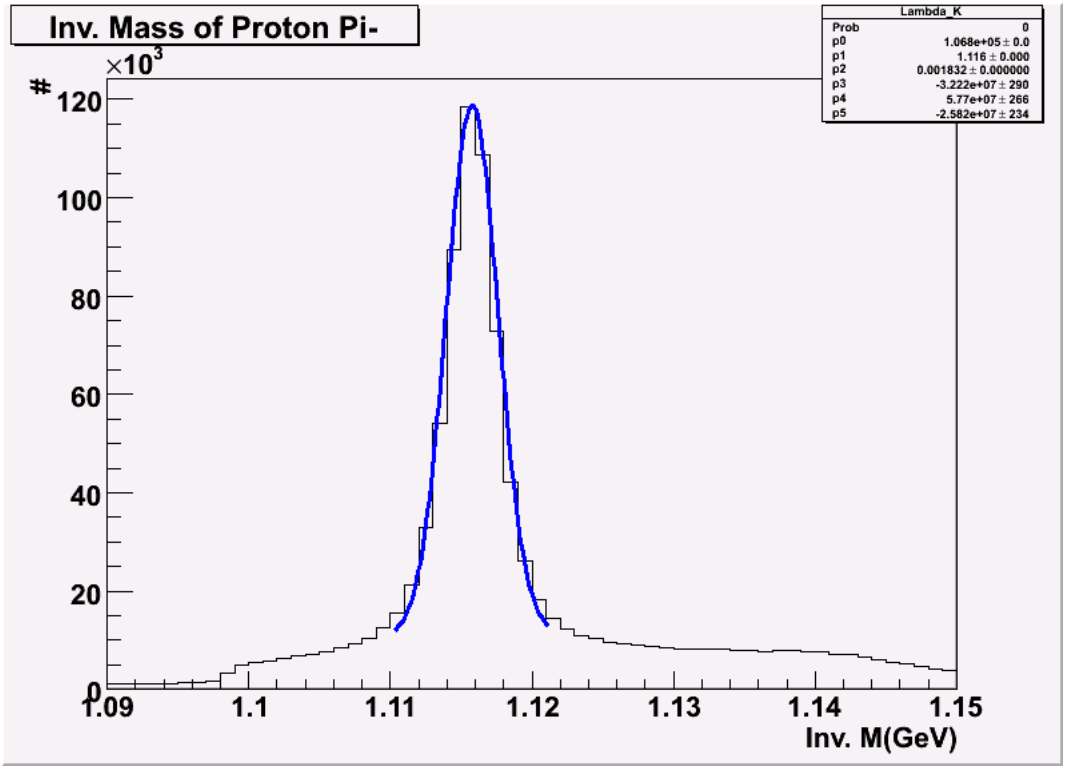

FIGURE 3.12. Invariant mass of $p\pi^-$ around Λ (1116). The blue line is a Gaussian fit with a peak position at 1.116 GeV and a width is about 1.8 MeV.

3.4.1. Trigger Word Cut. As discussed in the previous chapter 2.3.4, there are two trigger bits, bit 5 and bit 6. Bit 5 indicates that the event is a pre-scaled event with tracks coming from at least two sectors. Bit 6 indicates that the event has tracks populating at least three sectors. This work requires that bit 6 is on, which means that the events need to have tracks in at least three sectors.

3.5. Detector Performance Cuts

3.5.1. Minimum Proton Momentum Cut. When charged particles travel through the CLAS detector, they are bent in the magnetic field. When the momentum is so low that the trajectory is not well described by a simple parameterized fitting procedure or even not recognized by the pattern recognition in the cooking procedure, the particles are lost. The lowest momentum under which a proton can

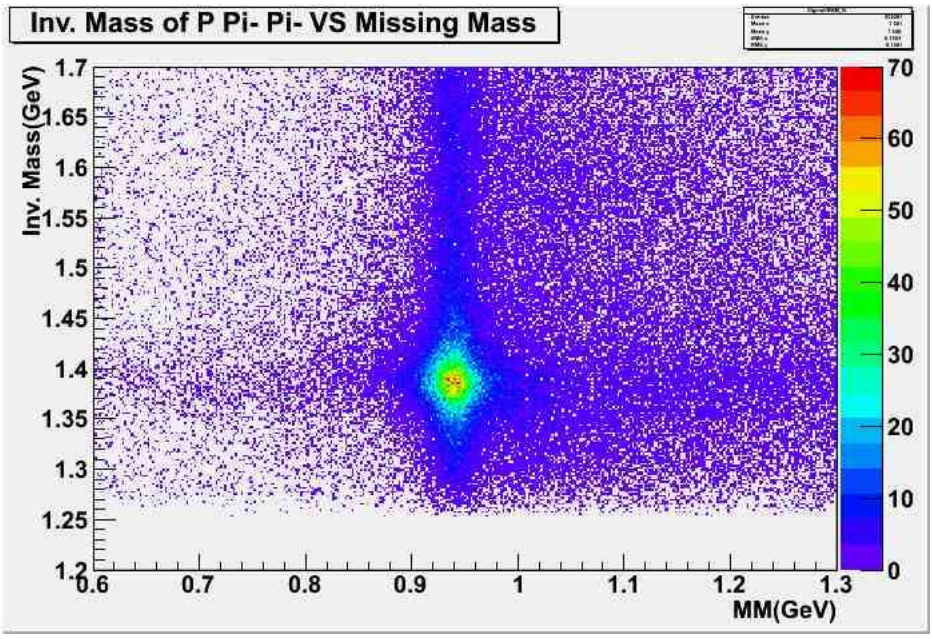

FIGURE 3.13. Invariant mass of $\Lambda\pi^-$ versus missing mass of $K^+\Lambda\pi^-$. The events of interest around the cross point of the $\Sigma(1385)$ band around 1.38 GeV and the spectator proton band around 0.94 GeV are clearly seen.

be reconstructed by the cooking program defines the threshold of detection. However, even above the threshold, in the area close to the threshold, protons are usually thrown away intentionally. The reason is that protons in that region are very difficult to simulate. This is due to two reasons. There is a relatively large amount of energy loss due to the ionization process when the proton travels through the detector. The other reason is that the acceptance is so low near the threshold that a small error would introduce a large relative error in the correction. The way to determine which of the protons to throw away is to plot the momentum distribution of protons and cut on the rising edge. The momentum distribution of protons is shown in Figure 3.14, and a momentum cut at 0.45 GeV is generated according to the distribution.

3.5.2. Fiducial Volume Cuts. The reason for cutting on low momentum protons is reiterated. Some kinematic regions have very low acceptance, which may introduce large uncertainty on the acceptance. Therefore, the fiducial volume needs to be cut out.

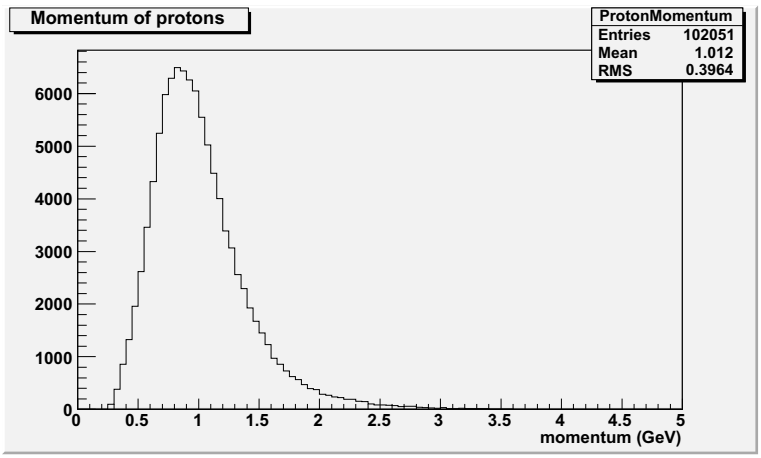

FIGURE 3.14. Momentum distribution of protons. A momentum cut on 0.45 GeV is produced according to this distribution.

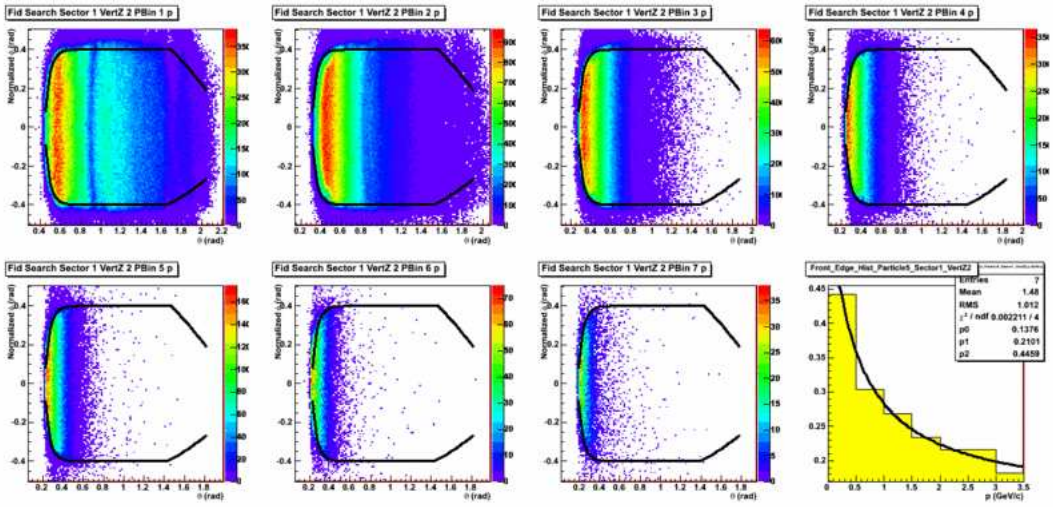

FIGURE 3.15. An example of the fiducial study of protons in sector 1 for middle vertex position. Top left to bottom right is the order of increasing proton momentum. Each histogram except the lower right one shows the distribution of ϕ versus θ in the sector frame and black line is the fiducial cut produced.

The study was done by Paul Mattione. The study was performed sector by sector. Because EG3 has a long target, the work studied the effect of the vertex position, which means it gathers particles into three groups according to the position where they are produced. The trajectory the particle travels depends on the momentum of the particle. Therefore, the work also groups particles according to the particle momentum. To summarize, the study has four independent variables: charge as

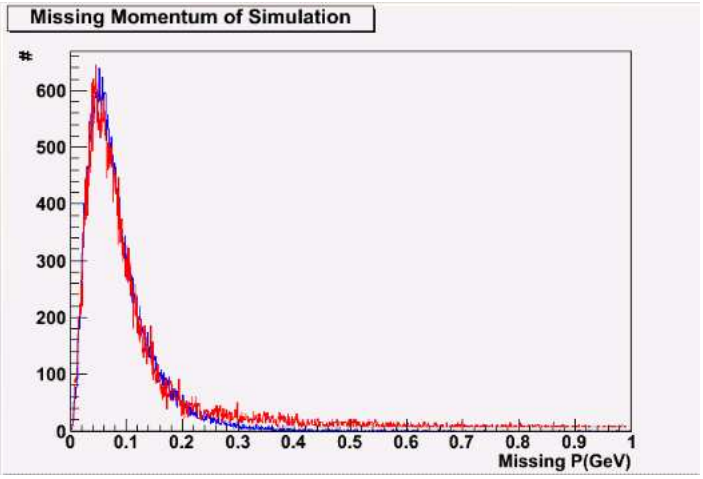

FIGURE 3.16. Comparison between missing momentum from data and simulation. The red line is from data and the blue line from the simulation. They are scaled by a global factor to match each other.

positive or negative, three groups of vertex positions, six sectors, and momentum. Particles are grouped according to these variables. For each group, the θ versus ϕ distribution is plotted, and a cut is produced according to the distribution. One example is shown in Figure 3.15. It shows the fiducial study of protons in sector 1 for the middle vertex position out of three. Each histogram shows the distribution of ϕ versus θ of protons, and the black line is the fiducial cut produced in each kinematic region. The bottom right histogram shows the lowest angle cut, corresponding to the forward-most angle protons of different momentum can be detected efficiently.

A similar study is done for π^-s, which is not shown here. The study can be further extended to any positive charged particles, by using the proton cuts, and to any negative charged particles, by using the π^- cuts. The reason is that the trajectories of particles do not depend on the mass of the particles if the energy loss can be neglected. Therefore, the fiducial cut needs to be done after the energy loss correction.

3.6. Missing Momentum Cut

This work studies the quasi-free production, which means the proton in the deuteron solely serves as a spectator. However, it is experimentally very difficult to exclude protons being involved in the reaction, especially in rescattering processes. The rescattering process implies that the production is on the neutron in the deuteron, but the proton interacts with the final-state particles like the π^-. Additionally, it is known that the proton inside the deuteron exhibits a Fermi motion, hence Fermi smearing of the momentum. Therefore, if the missing momentum, which is supposed to be the momentum of the missing proton, exhibits only Fermi smearing, it is more certain that the proton serves only as a spectator in the sense of statistics. This is done by comparing the missing momentum from data with the missing momentum from simulation, where the simulation is well controlled and the proton is serving simply as a spectator (shown in Figure 3.16). To enhance the quasi-free process, a cut on missing momentum of 0.4 GeV is applied.

3.7. Cut Away $K^*\Lambda$

After all the above cuts applied, it seems that an optimized data sample of reaction of interest is ready. However, there is an additional contamination from a related channel. It is $\gamma n \to K^*\Lambda$ where the K^* decays into $K^+\pi^-$. Therefore, this channel has the same final particles, $K^+\Lambda\pi^-$. The invariant mass of $K^+\pi^-$ versus the invariant mass of $\Lambda\pi^-$ is shown in Figure 3.17. The horizontal band of K^* and the vertical band of Σ^* are clearly overlapping. To remove the effect of K^*, a cut of 3σ on the y-axis from 0.82 to 0.95 GeV is applied.

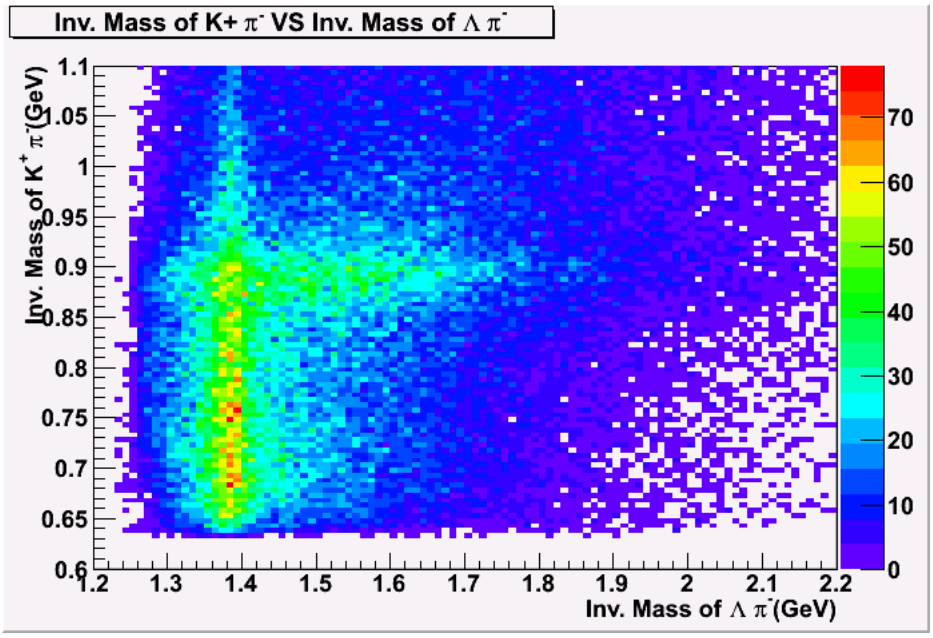

FIGURE 3.17. Invariant mass of $K^+\pi^-$ versus invariant mass of $\Lambda\pi^-$. The horizontal band at about 0.89 GeV is the collection of $K^*(\Lambda)$. The vertical band at about 1.38 GeV is the collection of $(K^+)\,\Sigma^{*-}$.

Chapter 4

Acceptance and Normalization

After selecting the interesting physics events measured by the CLAS detector from the data, the behavior of the detector itself needs to be studied. The purpose is to obtain the inefficiency information of the detector system, so that we can correct the yield obtained to the yield produced. This inefficiency could come from the detector performance or the software used to produce the raw data and convert the raw data to cooked data. The inefficiency from the detector performance could come from the geometry of the detector, the dead time of electronics, the noise from the hardware, unexpected behavior caused by cosmic ray background, and other sources. The data acquisition (DAQ) can have problems caused by the DAQ system's control, like the case that it needs to write the data from cache to tape when the cache is full. The cooking program also could introduce inefficiency in the case that it cannot extract trajectory information from digitization of detector components. This may be caused by too much background, noise from hardware, as well as the software itself having some limitation. The probability that an event in a certain kinematics will survive to the analysis stage is called acceptance. After the acceptance of the detector system is well understood and corrected, the number of events actually produced is obtained.

After the acceptance is obtained, the final goal is to determine the cross section. It is the final goal in most analyses. Cross sections can be used to compare with theoretical calculations or can be confirmed by other experiments carry out in different ways. The process from acceptance-corrected yield to cross section is normalization. The process needs to consider the total number of photons incident on the target during the photoproduction, the total number of target particles, the fraction of total

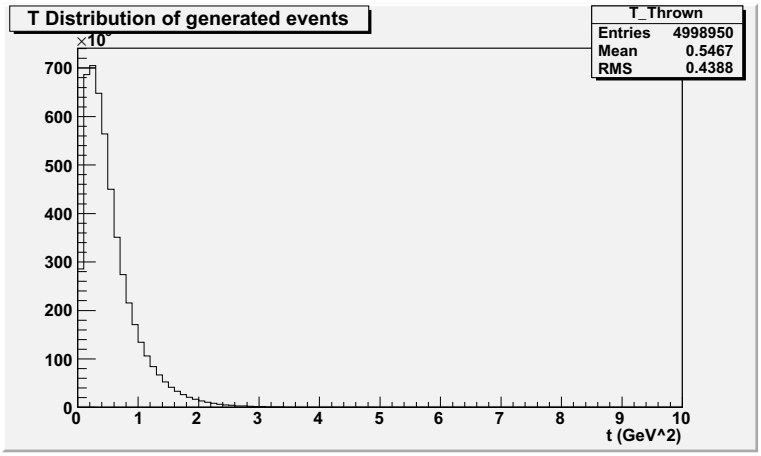

FIGURE 4.1. The t distribution of events from event generator. The gap on the left hand side reflects the minimum t that can be reached in this kinematic region for this channel.

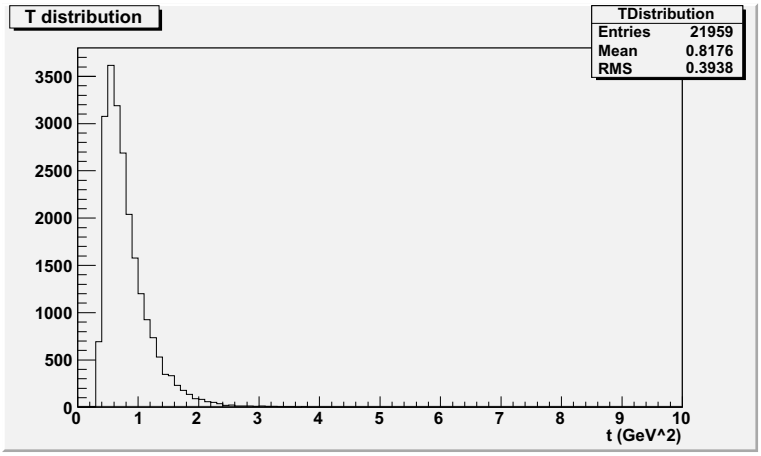

FIGURE 4.2. The t distribution of events from experimental data. The gap on the left hand side is mainly due to acceptance.

time when the detector system is ready to take data, branching ratio of decays, and more. This chapter describes the acceptance calculation and normalization factors.

4.1. Detector Simulation

The standard way in the CLAS collaboration to obtain the acceptance is using an event generator, the GSIM simulation package and the same cooking procedure as for the experimental data processing.

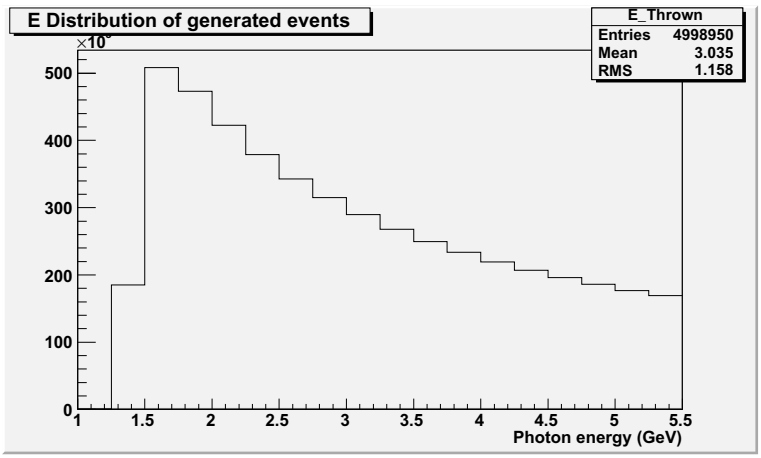

FIGURE 4.3. Photon energy distribution of events from the event generator. The photon energy covered is from the threshold of the production to slightly above 5.5 GeV. The graph exhibits an inversely proportional dependence on photon energy, that is characteristic for bremsstrahlung.

4.1.1. Event Generator. In the event generator step, events are produced as much like real-world events as up to our knowledge level possible. For an unknown production channel, it is typical to produce events according to the phase space distribution. The phase space distribution is to distribute events evenly in the phase space (momentum and coordinate space). However, in this case, we know that the channel is probably t-channel dominated, so that the t-slope phase space event generator is used. The t distribution of events generated is shown in Figure 4.1. The gap on the left hand side close to zero is due to the minimum t value that can reach in this kinematic region for the $K^+\Sigma^{*-}$ production channel. The same t distribution from physical events is also shown in Figure 4.2. Here the large gap on the left hand side is due to the acceptance. The t-slopes of the simulation is adapted to the simulation.

We generated events covering photon energies from the production threshold around 1.3 GeV to 5.5 GeV, and the distribution is shown in Figure 4.3. The number of events generated is inversely proportional to the photon energy. This is the character of bremsstrahlung.

The Breit-Wigner width of the Σ^{*-} is included in the simulation and the decay chain, too. All decay parameters are taken from the particle data group (PDG) values.

4.1.2. GSIM. The foundation of the acceptance calculation is the GEANT-based simulation (GSIM) package of the CLAS detector, which is the CLAS collaboration's standard simulation package. After events are produced by the event generator, they are processed by GSIM. GSIM propagates each of the particles through all CLAS components from the vertex produced by the event generator. The particles travel through the simulated detector where they may lose energy due to ionization, decay with probabilities according to PDG values, and multiple-scatter with detector materials just like in the real detector. The package also simulates the response of each detector component to the particles. The digitized signals from each component are collected and stored just like real events.

The GSIM output is then processed by the GPP package, which smears the detector signals to be more realistic. The scintillator times are smeared according to the length of the scintillator. GPP also smears the drift chamber signal according to the average drift time of ionization electrons to the sensor wires. GPP has a series of parameters allowed to be changed by users to match the resolution of each experiment.

The output of GSIM is then processed by the cooking program just like the experimental data.

4.1.3. Trigger Simulation. The details of the trigger are discussed in 2.3.4, and there are mainly two aspects. One is that it triggers on the photon energy above 4.5 GeV; therefore it creates a jump of yields around 4.5 GeV, which is shown in Figure 4.4. The correction of this will be discussed in the next section 4.3.2. The other is that it requires at least three-sector tracks in one event as discussed in 2.3.4.

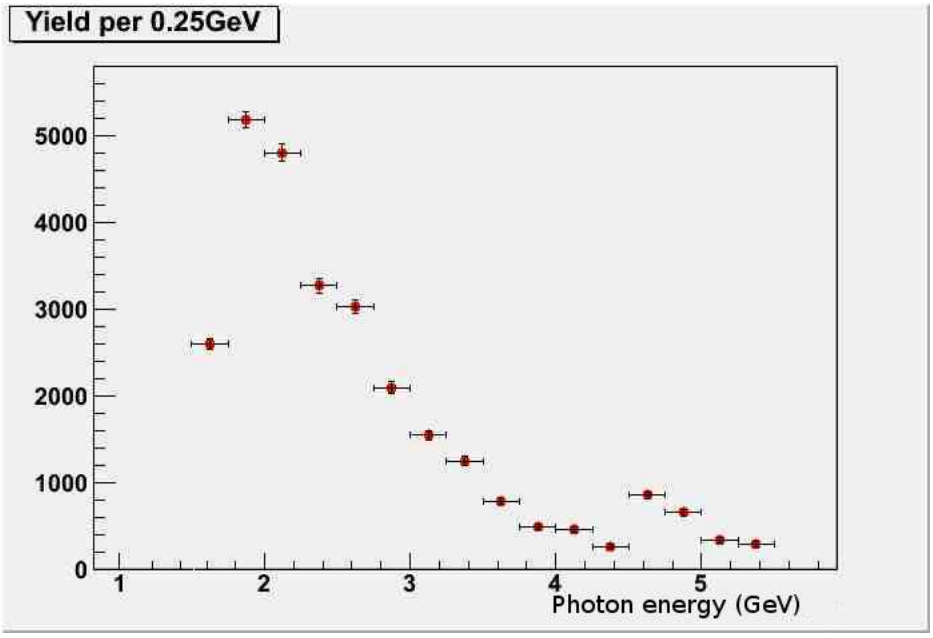

FIGURE 4.4. Yields of the exclusive $K^+\Sigma^{*-}$ channel independence of photon energy. The yield jumps up at 4.5 GeV due to the trigger condition.

The simulation of this is easily done by requiring that each event reconstructed has tracks coming from at least three sectors.

4.2. Energy Corrections

This section discusses the energy and momentum corrections used to improve the data. The two needed corrections are described in this section: energy loss correction and tagger correction.

4.2.1. Energy Loss Corrections. The momentum vectors of all four final state particles K^+, p, π^-, and π^- are corrected for energy loss when they go through all the detector components of CLAS. These charged particles lose energy mostly due to ionization and atomic excitation when they pass through detector materials. Corrections are made to account for the energy lost in the target material (liquid Deuterium) and walls, the start counters and all other materials from the start counter through the drift chambers. The corrections were applied by the eloss software package written by Eugen Pasyuk for the CLAS detector. The invariant mass of Λ is plotted to

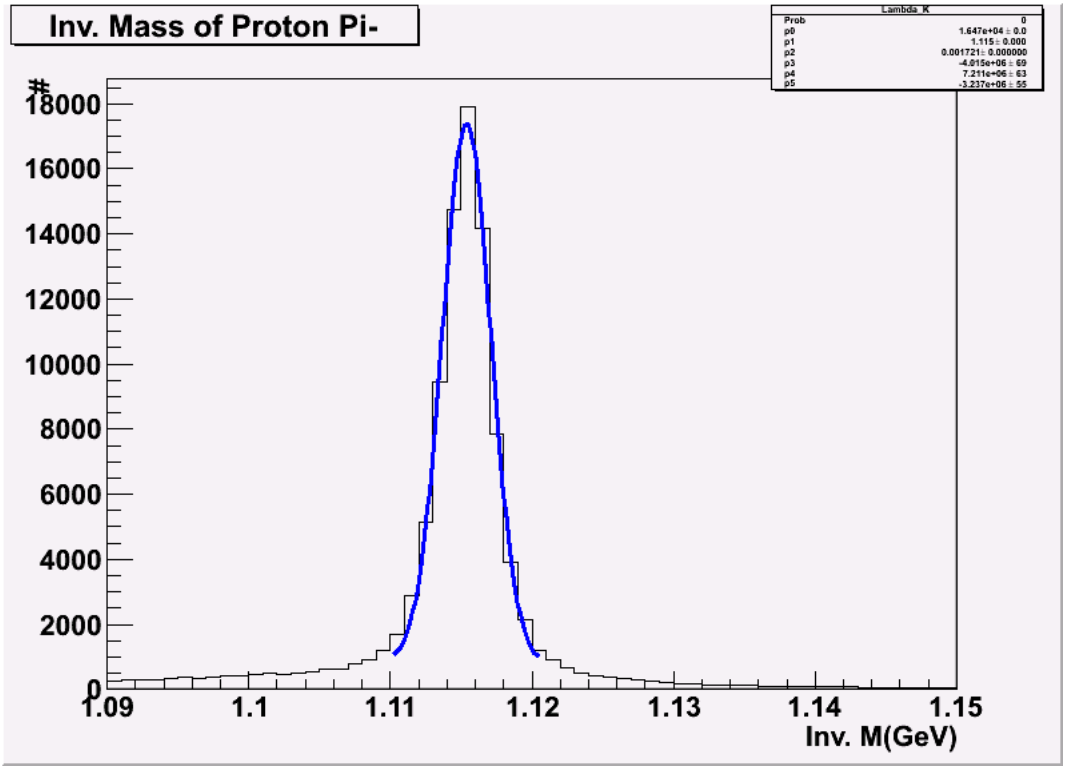

FIGURE 4.5. Invariant mass of $p\pi^-$ around $\Lambda(1116)$. The blue line is a Gaussian fit with a fitted peak position on 1.115 GeV. The fitted width is about 1.7 MeV.

verify this correction and shown in Figure 3.12. The same correction is applied on the simulation data. The same histogram is generated on the simulation data and shown in Figure 4.5. The peak position from both the histograms match with the PDG value, and the widths from both peaks match each other.

4.2.2. Tagger Corrections. The photon energy is measured by the tagger system as discussed in 2.2. The energy of the photon is determined simply by which path the photon follows, which is identified by the logical energy channel or logic paddle number. The relation of photon energy and logic paddle number is shown in Figure 4.8. The straight line in the histogram reflects the good relative calibration of the tagger system. However, Paul Mattione found by an independent study there is an energy shift needed, to correct the photon energy. His result was confirmed in this work. The missing momentum in the beam direction of the $K^+\Sigma^{*-}$ events is plotted

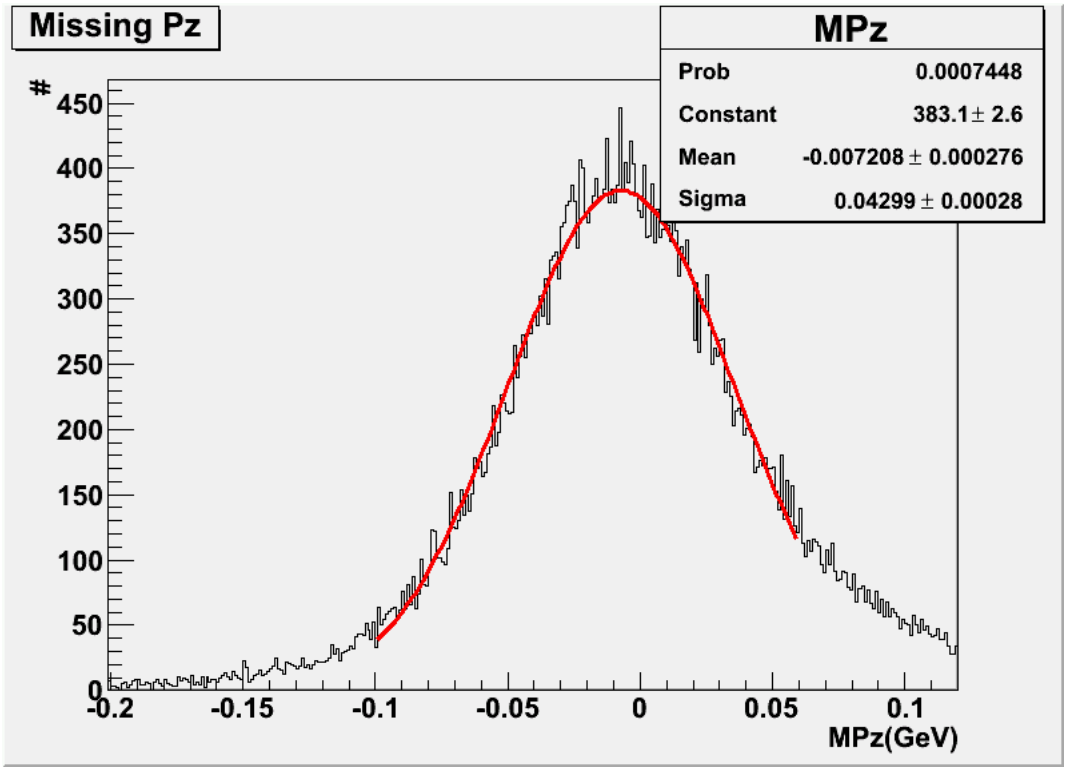

FIGURE 4.6. Missing momentum in beam direction. There is a deviation of the peak position from zero, which indicates that a correction is needed to recenter it at zero.

in Figure 4.6. It is fitted with a Gaussian distribution. The fitting result indicates that a global correction of about 7.0 MeV is needed for all photons. The result after correction is shown in Figure 4.7, where the peak is well centered around zero.

4.3. PHOTON NORMALIZATION

Another important piece of the cross section calculation is the number of photons incident on the target at different energies, which is called photon flux (gflux). It is also standard in CLAS analyses to include the detector live time at this stage. The live time is the accumulated amount of time the tagger system is ready to record data.

4.3.1. gflux. A detailed discussion can be found in [1]. The gflux method is used to determine the photon flux detected by the detector system. The idea of

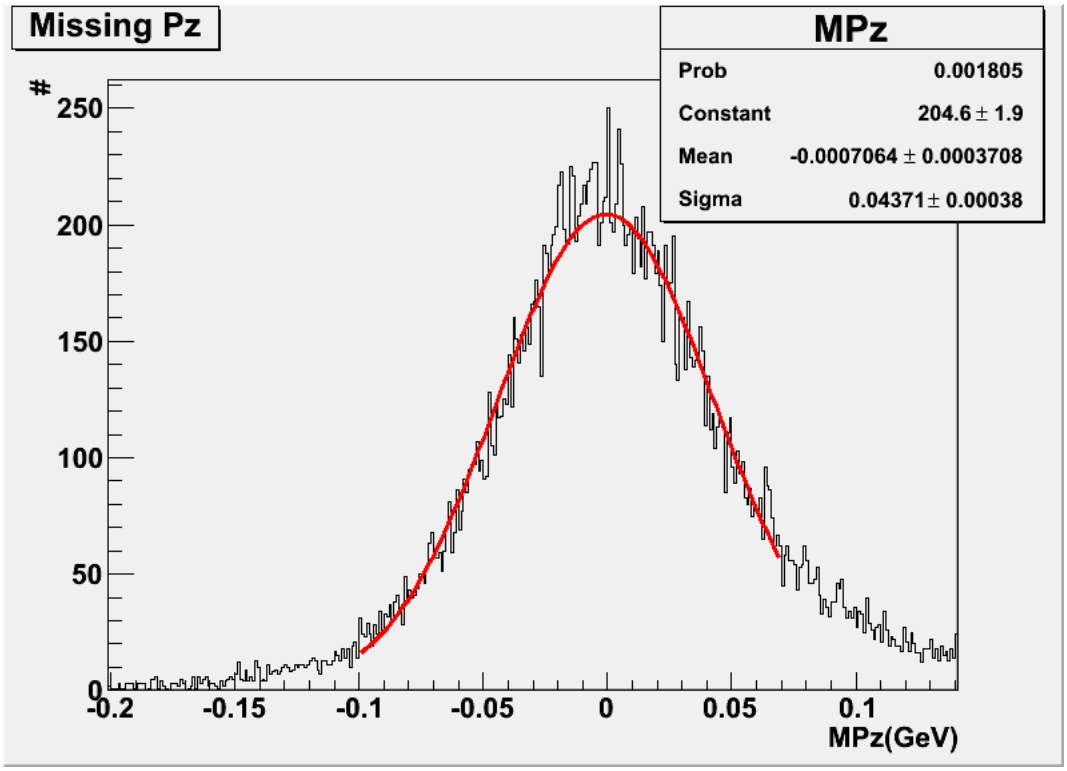

FIGURE 4.7. Missing momentum in beam direction with corrected photon energy. The peak is well centered around zero.

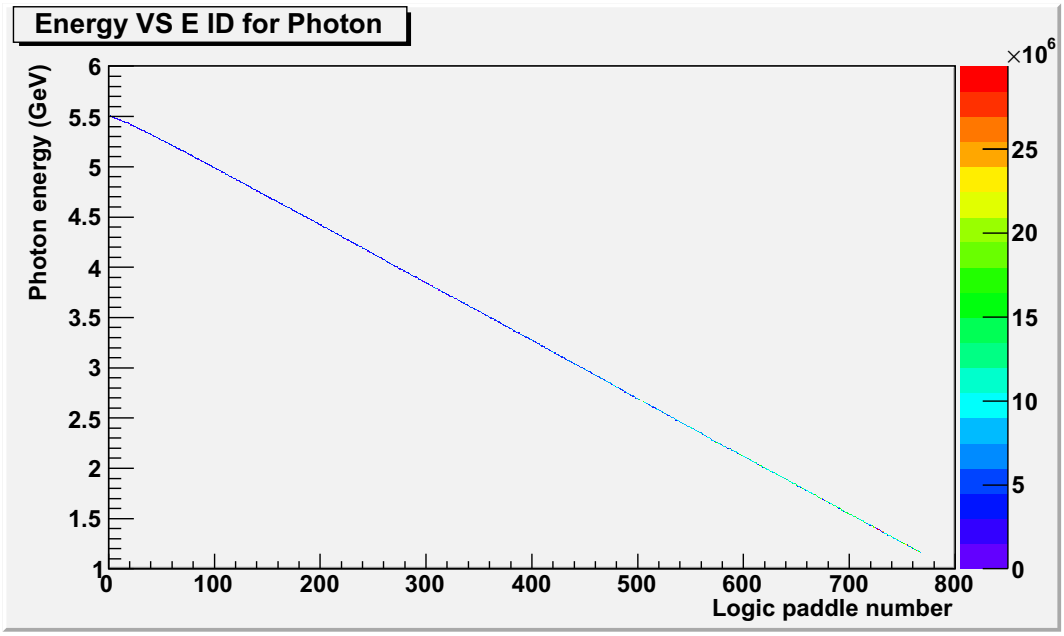

FIGURE 4.8. Photon energy versus the logic paddle number. The color shows the occupation of photon at different energies.

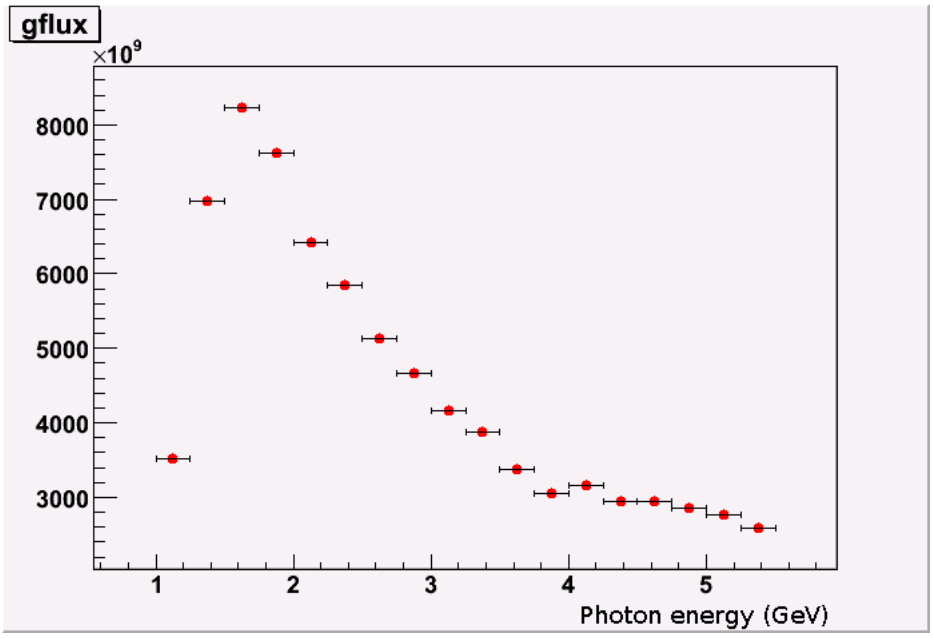

FIGURE 4.9. gflux independence of the photon energy. The first two bins have severe efficiency issues as described in 3.2.

the method is to use the out-of-time photons, which do not produce the events, to calculate the rate corresponding to each T-Counter. This rate is then corrected by a factor accounting for the photon loss between the tagger and the target. The factor is determined during test runs. It is then multiplied with the live time, which is the sum of small intervals during which the rate is consistent with each other within statistical error. The final gflux result is shown in Figure 4.9 and used to normalize yields.

4.3.2. Un-Trigger T-Counter Correction. As discussed in 2.3.4, only the first 20 T-counters in the tagger system were included in the EG3 trigger system, while all T-counters are on. Thus, events caused by photons associated with recoil electrons hitting counters 21 - 60 can only be recorded when there is at least one recoil electron that hits one of the first 20 T-counters during the trigger time window. This causes a discontinuity around 4.5 GeV as shown in Figure 4.4. The gflux software package uses "out-of-time" photons, which are not affected by this trigger condition. Therefore, the result from gflux could not account for this discontinuity, and additional corrections need to be applied.

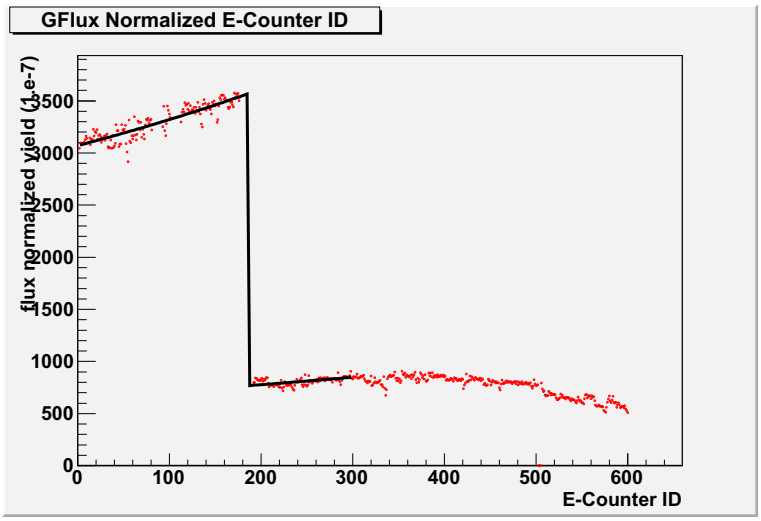

FIGURE 4.10. Normalized yield of mixed-channel events versus E-counter logic paddles. The jump happens at the edge of the triggered to un-triggered region. A second order polynomial function with a jump factor is used to fit the histogram drawn in red. It gives the factor 4.65.

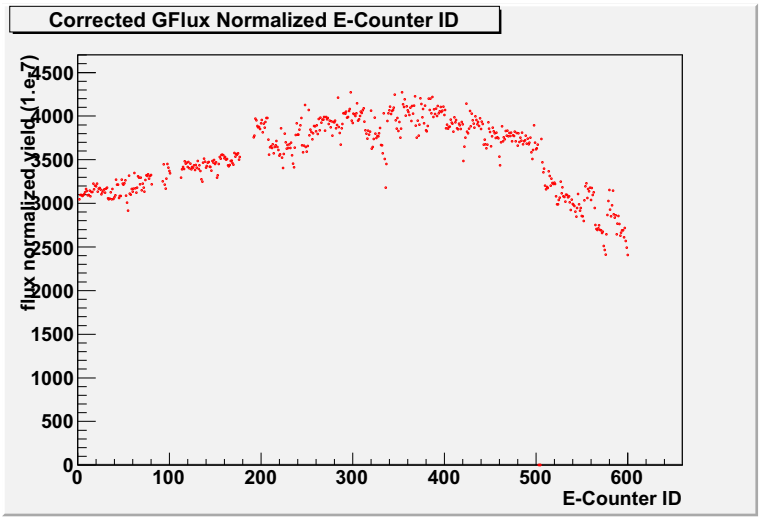

FIGURE 4.11. Corrected normalized yield of mixed-channel events versus E-counter IDs. A factor of 4.65 is used. The dependence of the normalized yield on logic paddles looks continuous.

There are several ways to do this. However, we use a practical approach of plotting the gflux-normalized yield of mixed-channel events as shown in Figure 4.10. The histogram excludes those events with multiple photon hits (see 3.3.2) because multiple photons will wash out the jump and lead to a wrong value. The histogram is fitted with a second order polynomial function and a scaling factor on the low E-counter ID

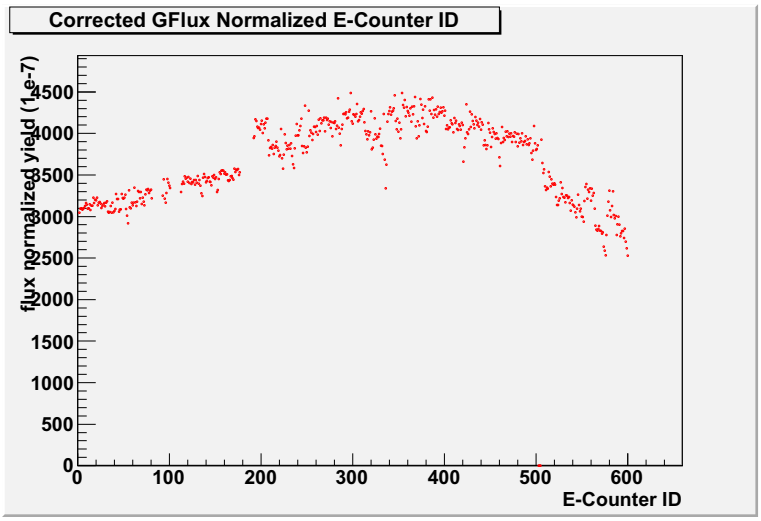

FIGURE 4.12. Over-corrected normalized yield of mixed-channel events versus E-counter IDs. The factor used here is the product of 1.05×4.65. The dependence of the normalized yield on logic paddles shows a little discontinuity at the edge of trigged region.

end. The fit gives the factor as 4.65. The same histogram corrected by the factor is shown in Figure 4.11 and shows no discontinuity. The fit relative error of the factor is about 5%, and an over-corrected normalized yield is shown in Figure 4.12, where a discontinuity to the opposite direction of the uncorrected data is just appearing.

However, this estimate of the factor is biased due to this method. There is no way to get an over-estimated factor, because the accidental photon contribution due to the timing method adds a constant background in Figure 4.10 which washes out the jump to lower the value. In order to compensate for that, an additional factor compensating for the accidental photons selected by the timing method discussed in 3.3.1 (shown in Figure 3.9) is applied. It brings the factor from 4.65 to 4.72 by using additional factor 1.015. The relative error of this factor is 5%.

4.3.3. Trigger Efficiency Correction. There is a discrepancy found in various runs in Hall B. If we plot the normalized rate of a certain channel, there is a discrepancy between runs before and after Christmas appearing on the histograms. Figure 4.13 is the histogram plotted by Hovanes Egiyan when he studied the pentaquark. He plotted events of at least four final state particles with trigger bit 5

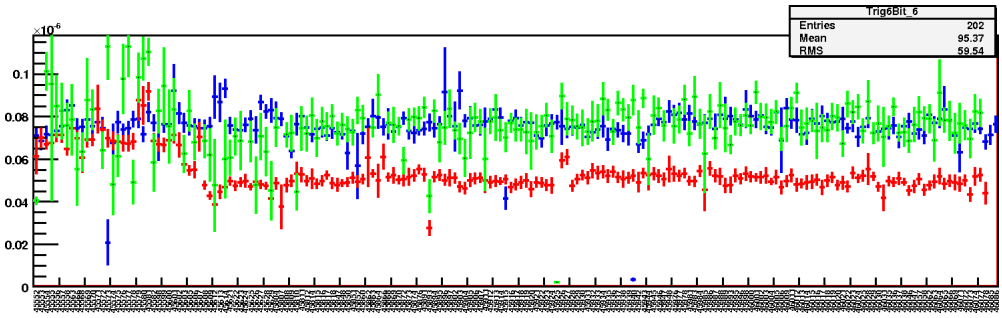

FIGURE 4.13. Comparison of normalized rates of inclusive Λ production with different trigger bits. Events of at least four particles are selected. Prescale factor corrected rates of events with bit 5 are plotted in blue. Normalized rates of events with bit 6 are plotted in red. Where the discrepancy starts to appear corresponds to the change of run condition around Christmas 2004. Data points in green represents normalized rate of bit 6 but corrected by an additional factor to match data points in blue.

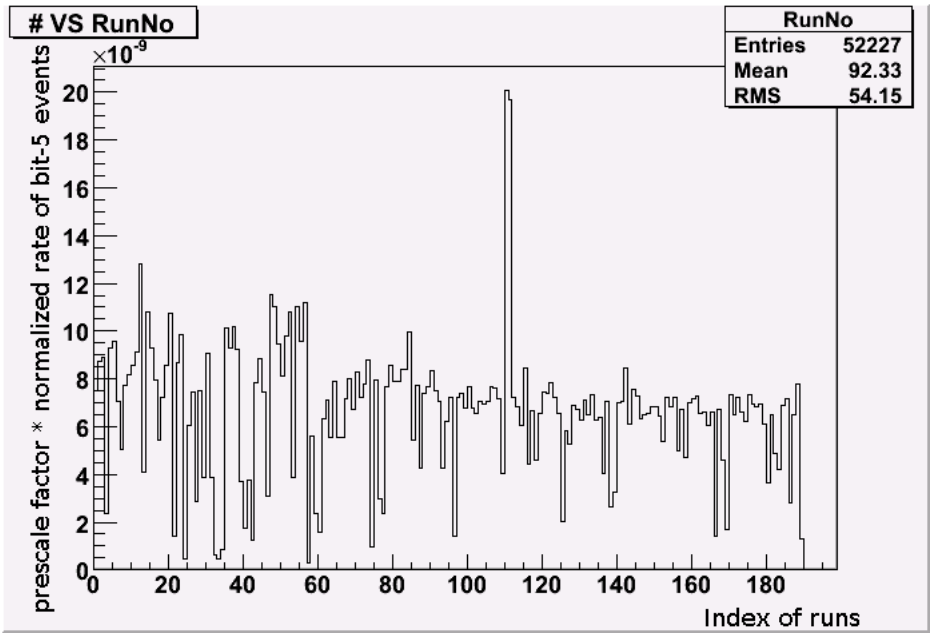

FIGURE 4.14. Prescale factor corrected normalized rates of exact four-track events with trigger bit 5 on, in kinematic region of interest. The discrepancy near the 60th run is corresponding to a run condition change around Christmas 2004.

corrected by a prescale factor and events with trigger bit 6. They are supposed to match with each other. However, there is a discrepancy in those runs after the Christmas 2004. After Christmas, the signal from start counters are put into the timing

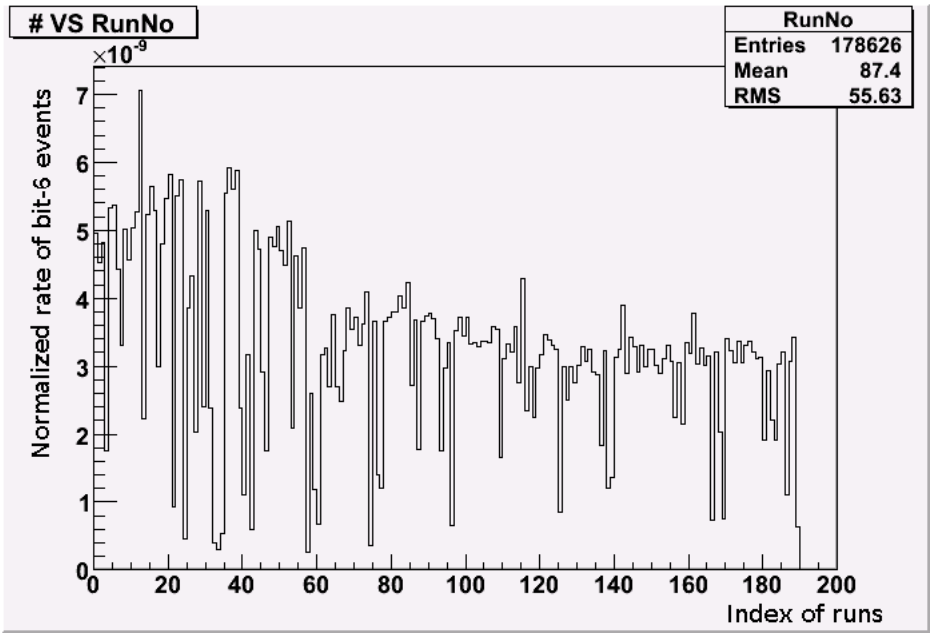

FIGURE 4.15. Normalized rates of exact four-track events with trigger bit 5 on, in kinematic region of interest. The discrepancy near the 60th run is corresponding to a run condition change around Christmas 2004.

requirement of the trigger system. This factor is channel-dependent determined for $K^+\Sigma^{*-}$ channel.

Two histograms are generated similar to Hovanes's work. Figure 4.14 shows the prescale-corrected rate of events with bit 5, and Figure 4.15 shows the normalized rate of events with bit 6. The goal is to normalize the rates of bit 6 for all runs to the rates of bit 5 before Christmas 2004. The resulting correction factor is taken as 1.5 for runs before Christmas and 3.3 for runs after Christmas.

Chapter 5

Cross Sections

In scattering theory, the likelihood of a particular reaction happening is defined as the cross section. It originally started from the classical theory of a point-like particle hitting a target filled with spheres. The probability of a reaction, which means the particle hits a spheres, is simply the ratio between the total cross-sectional area of all spheres and that of the target. In modern scattering theory, it is defined as

$$N_{reaction} = \frac{N_{incoming} N_{target}}{A} \sigma \tag{5.1}$$

where $N_{reaction}$ is the number of reaction events, $N_{incoming}$ is the number of incoming particles and $\frac{N_{target}}{A}$ is the target particle density respectively, and σ is cross section. In this study, the cross section is calculated by

$$\sigma = \frac{Y}{aL} \frac{1}{f_{br}} \tag{5.2}$$

where Y is the yield, a is acceptance, f_{br} is the decay branching ratio, and L is the integrated luminosity. The integrated luminosity is the product of two parts. One is the photon flux, corresponding to $N_{incoming}$. The other one is the areal target particle density calculated as

$$\frac{N_{target}}{A} = \frac{\rho l N_a}{m_{mol}}, \tag{5.3}$$

where ρ is the density of the target, l is the length of the target and 40 cm here, N_a is the Avogadro constant and m_{mol} is the mass of the target material per mole.

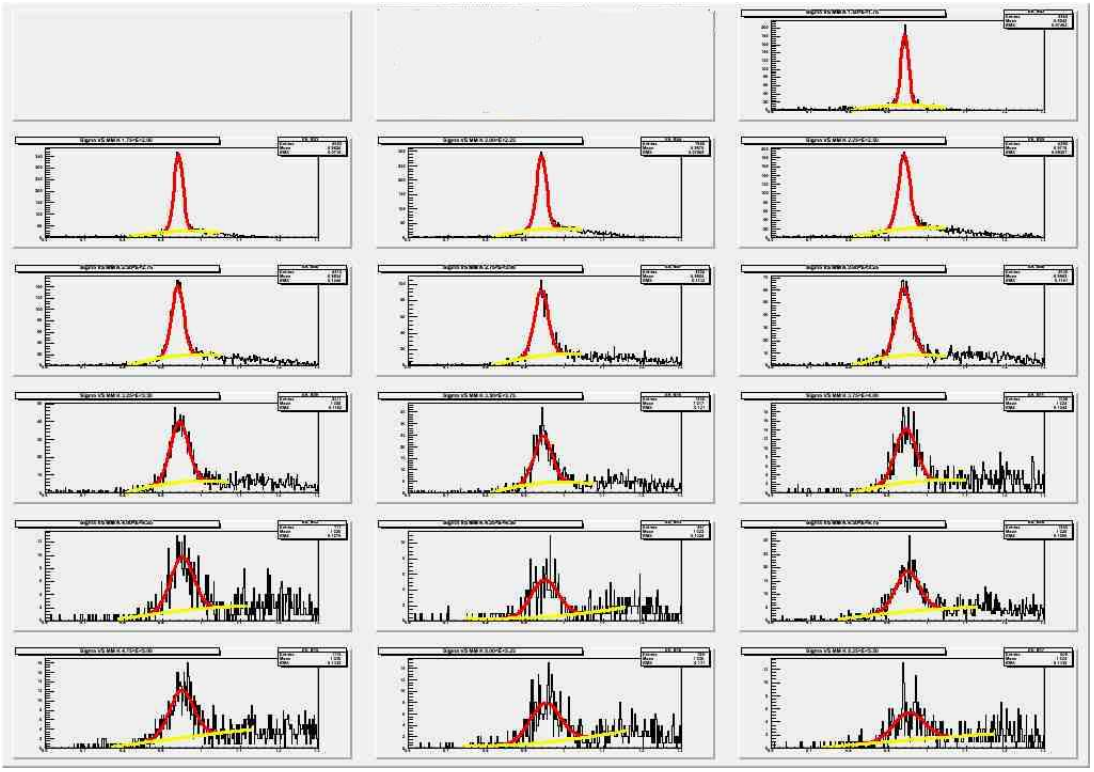

FIGURE 5.1. Missing mass of $K^+\Lambda\pi^-$ in each energy bin. The photon energy increases from top left to bottom right and ranges from 1.5 GeV to 5.5 GeV. The peak is on the spectator proton mass position. A Gaussian distribution (signal) plus a second order polynomial function (background) is used to fit the histogram and plotted in red. The background fit is plotted in yellow.

5.1. KINEMATIC BINNING

5.1.1. Total Cross Section. The data is binned into 16 photon energy bins from 1.5 GeV to 5.5 GeV. The invariant mass of $\Lambda\pi^-$ and missing mass of $K^+\Lambda\pi^-$ are calculated for all events in each energy bin as shown in Figure 5.1 and Figure 5.2.

5.1.2. Differential Cross Section. To extract the differential cross section, the data is again divided into 16 photon energy bins and 10 polar angle bins in cosine θ of K^+ in the center-of-mass frame. The same as in total cross section case, invariant mass and missing mass are calculated in each bin.

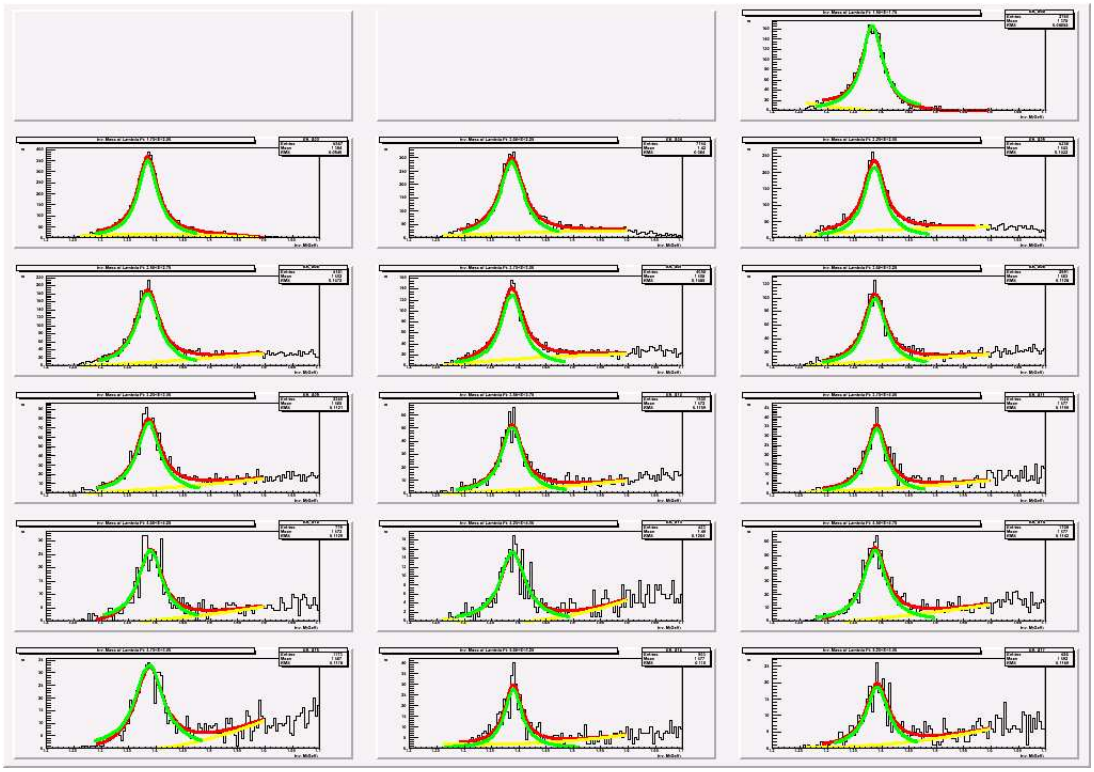

FIGURE 5.2. Invariant mass of $\Lambda\pi^-$ after the missing mass cut has been cut in each energy bin. A Breit-Wigner function (signal) plus a second-order polynomial function (background) is used to fit each histogram. The overall fit is shown in red, background in yellow, and signal peak in green. The photon energy increases from top left to bottom right and ranges from 1.5 GeV to 5.5 GeV.

5.2. Missing Mass Fitting

After binning data, the missing mass of $K^+\Lambda\pi^-$ is plotted and fitted with a Gaussian distribution plus a polynomial background. Then a cut of 3σ, where σ is the width of the Gaussian distribution, around the peak position is applied in order to extract yields. This process is done in both the total cross section case and the differential cross section case. The histograms and fits to extract total cross sections are shown in Figure 5.1.

5.3. Invariant Mass Fitting

The invariant mass of $\Lambda\pi^-$ is plotted after the missing mass cut in each energy bin. A Breit-Wigner function for the signal plus a second-order polynomial function

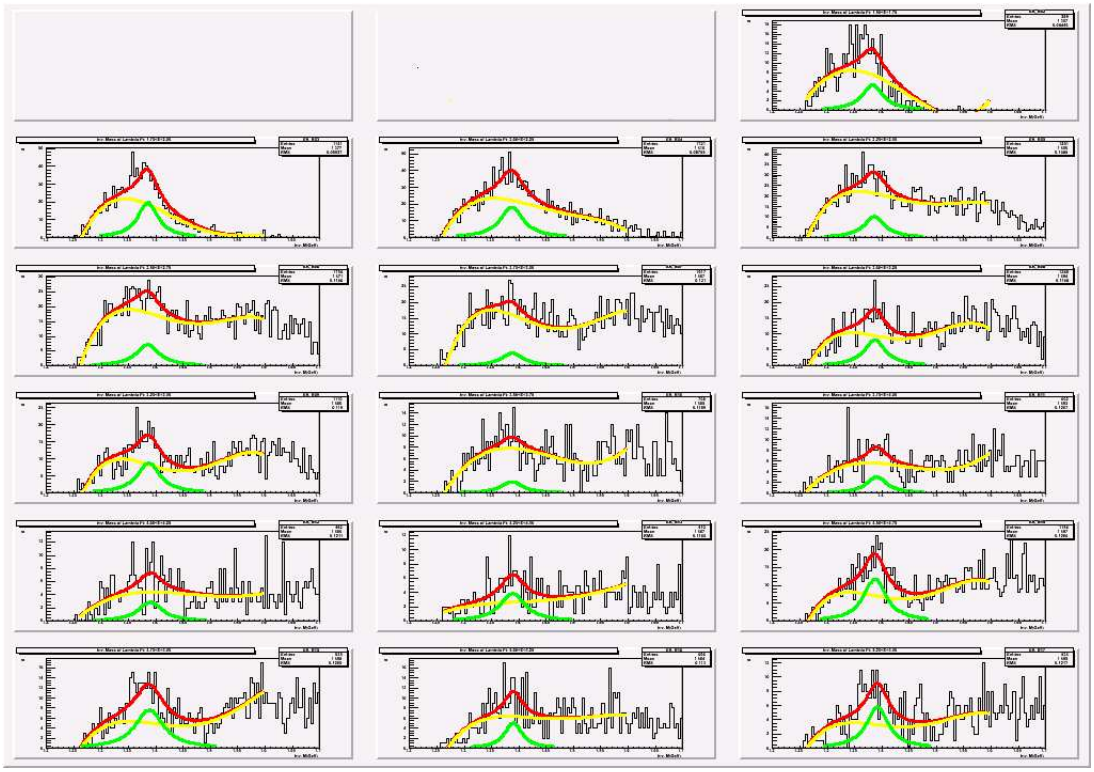

FIGURE 5.3. Invariant mass of $\Lambda\pi^-$ to the right hand side band of the missing mass peak plotted after the same 3σ cut in each energy bin. A Breit-Wigner function for the signal plus a third-order polynomial function for the background is used to fit each histogram. The overall fit is shown in red, background in yellow, and signal peak in green. The photon energy increases from top left to bottom right and ranges from 1.5 GeV to 5.5 GeV.

for the background are used to fit each histogram. The overall fit is shown in red, background in yellow, and signal peak in green. The integration over the green Breit-Wigner fit is the number of events obtained. The same process is also applied to extract the differential cross sections. The histograms and fits to extract the cross sections are shown in Figure 5.2.

5.4. Side Band Extraction and Yield Extractions

In order to extract the signal from the background, side-band subtraction is applied. However, there is a small variation in this case. Typical side-band subtraction cuts the same 3σ width on both sides of the missing mass peak. After fitting the

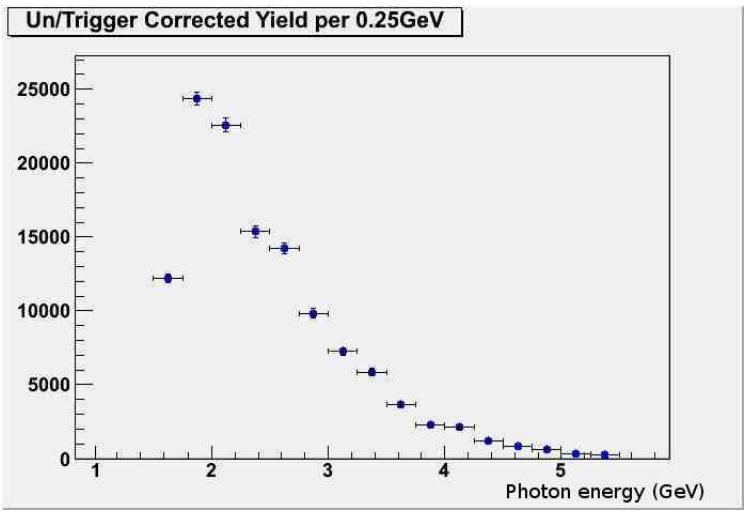

FIGURE 5.4. Untrigged T-counter corrected yields binned in photon energy.

invariant mass peak on both side bands, the average integrated peak from both side bands is subtracted from the number under the invariant mass peak. In this process, a linear behavior of the background in the missing mass histograms is assumed. However, in this case there is little background in the left hand side band. The right hand side band begins to appear and increases when the photon energy increases. This is the case since additional particles are produced when the energy increases. However, these particles are not detected by the detector system. Thus, they become the background. By assuming the linear behavior as typical side band subtraction, and using the relation of similar triangles, a factor of $\frac{1}{3}$ is obtained. This is applied on both total cross section and differential cross section cases.

The invariant mass of the missing mass side band is plotted and shown in Figure 5.3. In order to fit it with a Breit-Wigner function and a third-order polynomial function, the following steps applied. First, cut away the invariant mass peak according to PDG value. Second, fit the rest with a third-order polynomial function and keep the parameters fixed. Finally, fit the total function with the so fixed background. The initial difficulty comes from the fact that there are too few events and too many parameters to fit, but with this fitting subroutine the fits are quite stable.

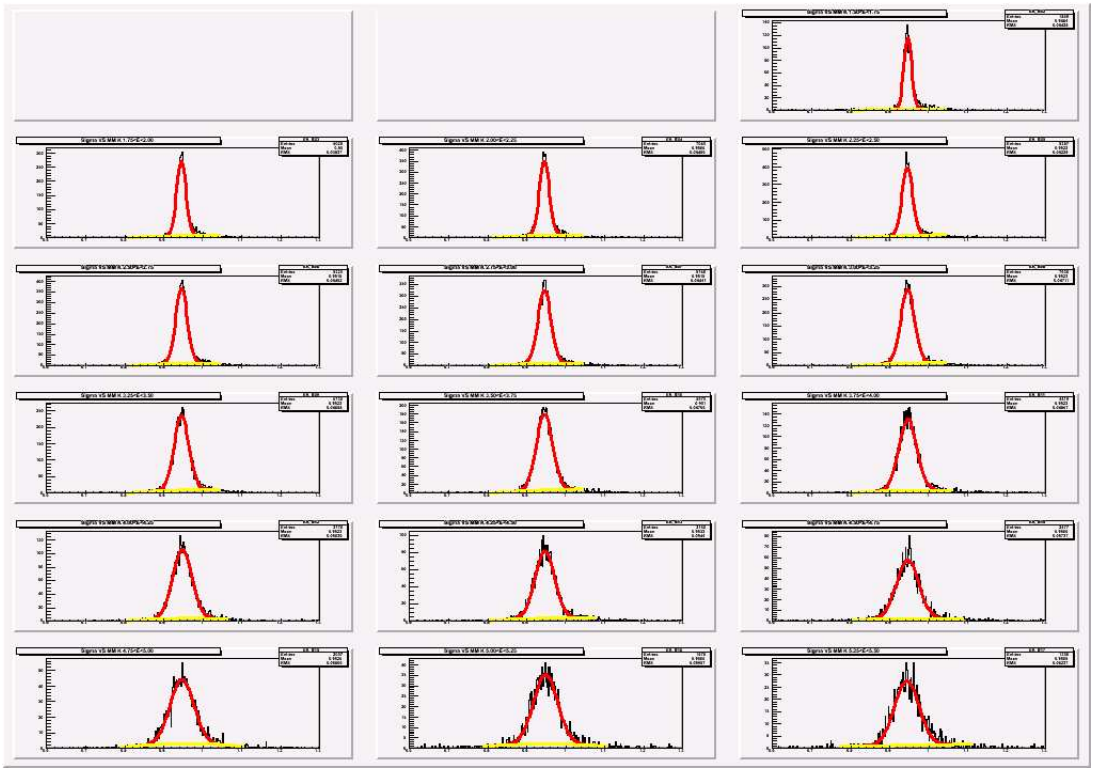

FIGURE 5.5. Missing mass of $K^+\Lambda\pi^-$ from simulation is plotted in each energy bin. The photon energy increases from top left to bottom right and ranges from 1.5 GeV to 5.5 GeV. The peak is on the spectator proton mass position. A Gaussian distribution (signal) plus a second-order polynomial function (background) is used to fit the histogram and plotted in red. The background fit is plotted in yellow. There is almost no background.

The side band subtracted yield is shown in Figure 4.4. The jump around 4.5 GeV is due to the trigged photon energy range as explained in chapter 4. The yield after this correction is shown in Figure 5.4.

5.5. Acceptance and Cross Section

5.5.1. Total Cross Section. After the yield is obtained from the experimental data, the same process is repeated for the simulation data. However, since only the production channel is simulated, there is little background and no side band seen in Figure 5.5. After the yield of the simulation is obtained, the acceptance is determined

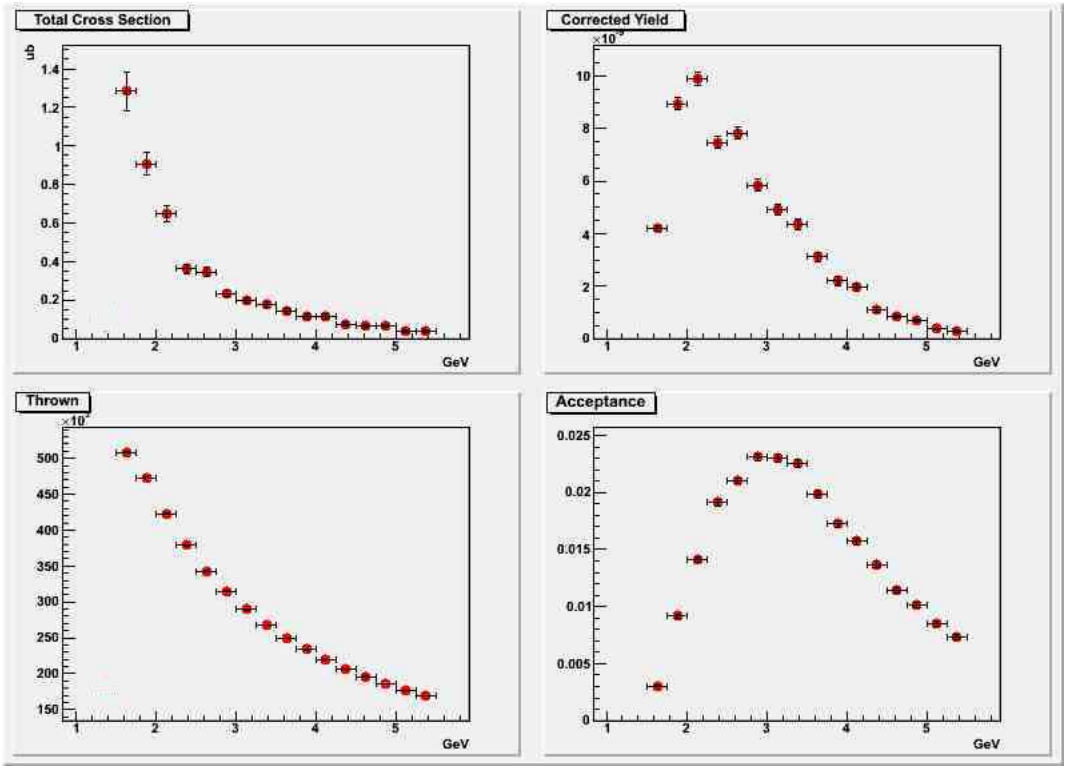

FIGURE 5.6. Top left: total cross sections dependent on the photon energy; top right: gflux-normalized and corrected yields; bottom left: distribution of the events from the event generator; bottom right: acceptance dependent on photon energy.

by dividing the reconstructed yield by the number of events from the event generator. The cross section is then obtained according to Eqn. (5.2).

5.5.2. Differential Cross Section. The same process is carried out to extract the differential cross sections. The angle of K^+ in the center-of-mass frame has a strong correlation with t channel. The K^+s are produced mostly in the forward angle, which is consistent with the t-channel production assumption. The dependence of differential cross sections on the photon beam energy is shown in Figure 5.7 in 13 bins of the cosine angle of K^+ in the center-of-mass frame. The same plot is shown in Figure 5.8 in log scale. The dependence of differential cross sections on the cosine angle of K^+ in the center-of-mass frame is shown in Figure 5.9. The same plot is shown in log scale in Figure 5.10.

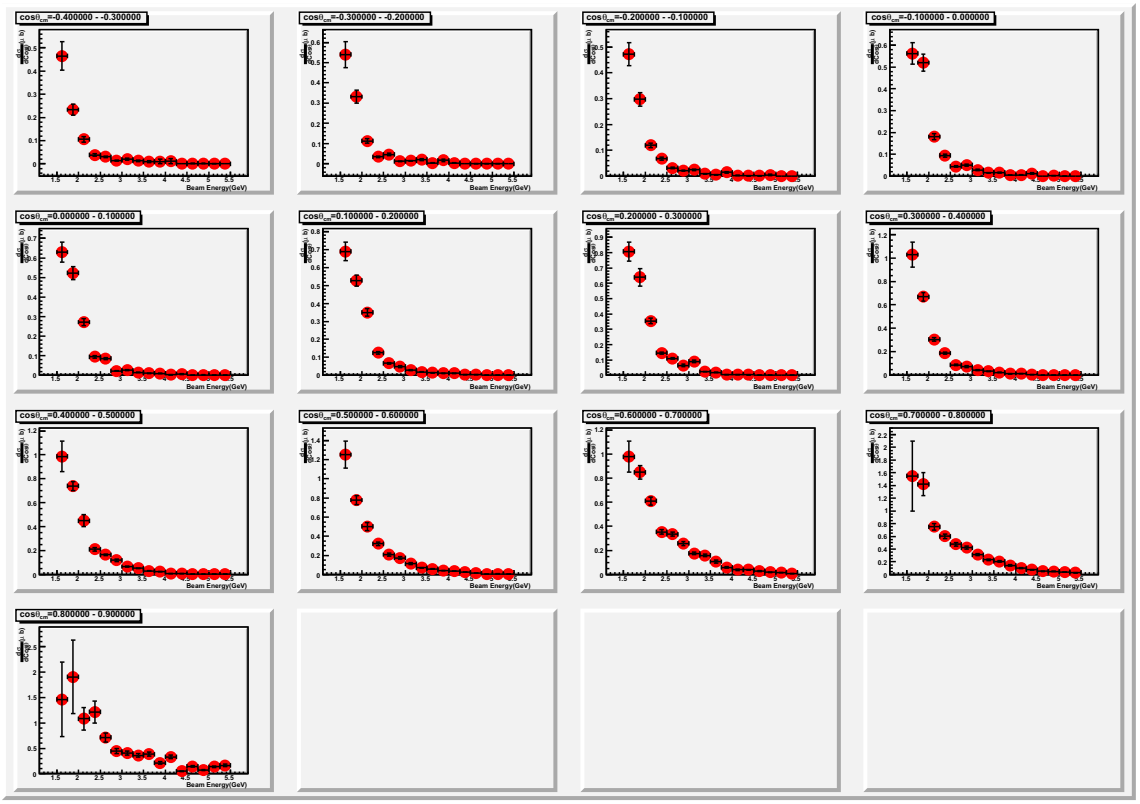

FIGURE 5.7. Differential cross section for $cos\left(\theta_{cm}^{K}\right)$ dependence on the photon beam energy. The cosine of the angle of K^+ in the center-of-mass frame starts from between -0.4 and -0.3 at the top left to between 0.8 and 0.9 at the bottom.

5.6. Comparison with Previous Measurement

As indicated in the first chapter of this thesis 1.3.1, there is only one published experiment on this channel that has only measured differential cross sections. Therefore, only the differential cross section can be compared to existing results. The results are compared in the previous published kinematic range. Most of them are consistent with each other as shown in Figure 5.11.

5.7. Systematic Error Study

The typical way to study the systematic errors is varying the different conditions and calculating the differences of the results demonstrating the systematic errors.

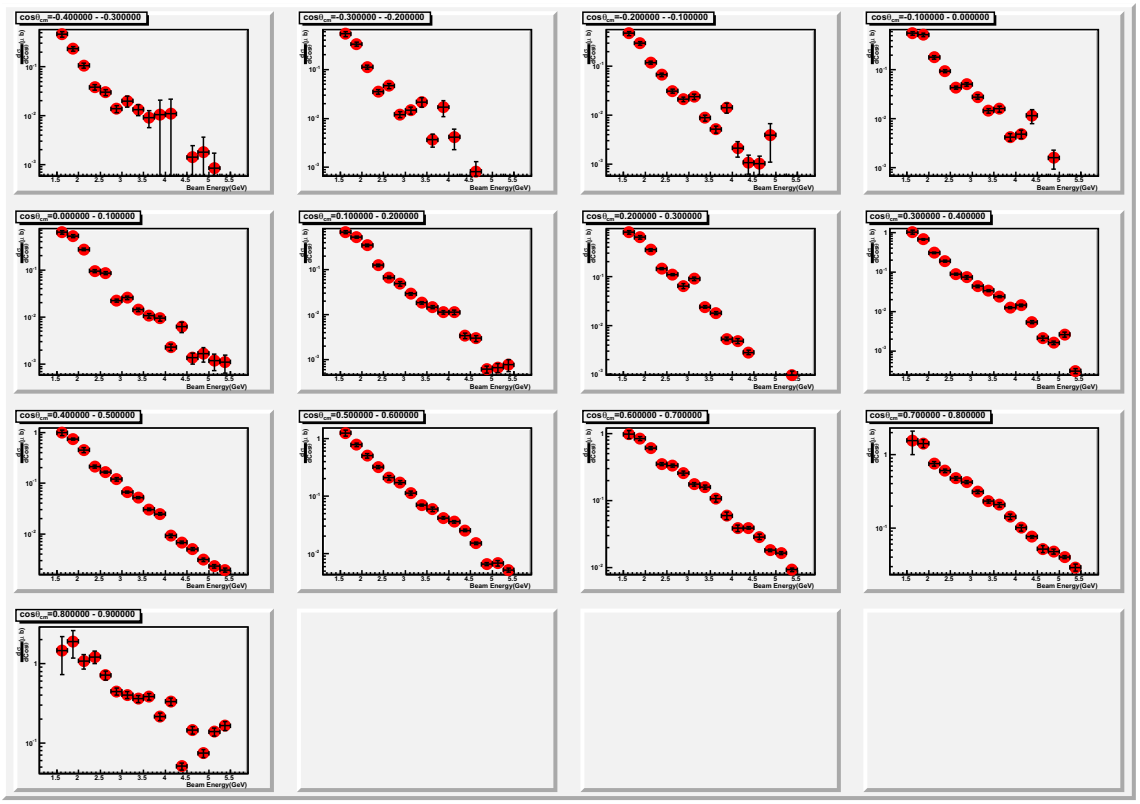

FIGURE 5.8. Differential cross section for $cos\left(\theta_{cm}^{K}\right)$ in log scale dependence on the photon beam energy. The cosine of the angle of K^+ in the center-of-mass frame starts from between -0.4 and -0.3 at the top left to between 0.8 and 0.9 at the bottom.

5.7.1. Fiducial Cut. To study the systematic error of fiducial cut, the total cross sections with and without fiducial cut are compared in Figure 5.12 and also in log scale as in Figure 5.13. The cross sections agree with each other within statistical errors. This suggests that the systematic error of fiducial cut is negligible.

5.7.2. Quansi-free Spectator. This reaction is studied as a quasi-free reaction. The cut to enhance it is the missing momentum cut. The missing momentum is interpreted as the momentum of the spectator proton. The effect is studied by varying the cut from 400 MeV to 300 MeV and 200 MeV. The comparison is shown in Figure 5.14. They agree very well within the statistical error bars.

5.7.3. Acceptance. The systematic study of acceptance is done by requiring K^+ in different sectors. As long as inefficiency of detector components are corrected

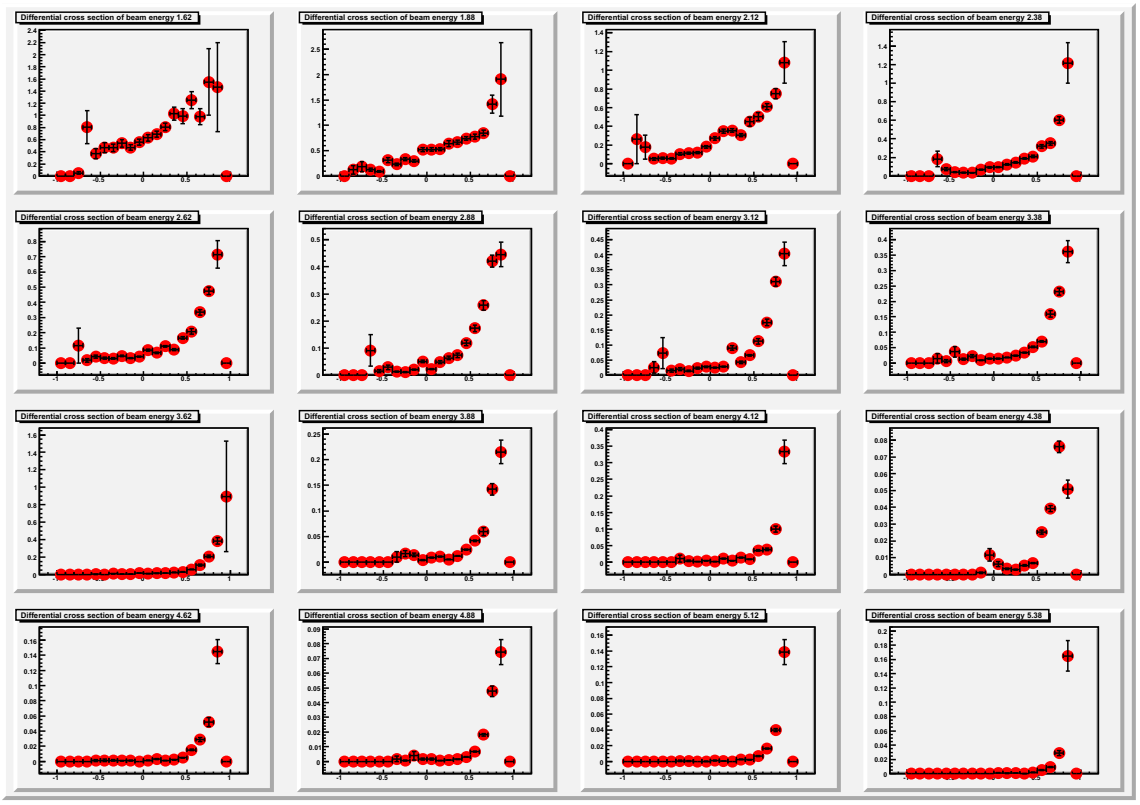

FIGURE 5.9. Differential cross section for $cos\left(\theta_{cm}^{K}\right)$ dependence on the cosine of the angle of K^+ in the center-of-mass frame. The photon beam energy starts from 1.5 GeV at the top left to 5.5 GeV at the bottom right.

properly, the cross sections obtained from different sectors should be the same. The comparison is plotted in Figure 5.15 in linear scale and in Figure 5.16 in log scale. To further calculate the exact value, the ratios of each cross sections to the average are shown in Figure 5.17. The number of data points getting contact with the ratio "1" is 49 out of 96. The number expected is 65 according to the Gaussian distribution. This indicates a systematic error is needed. The way to calculate this error is by adding a constant error to each data points till the number getting contact with the "1" is reaching the number expected. This gives the value of systematic error of acceptance as 8.5%.

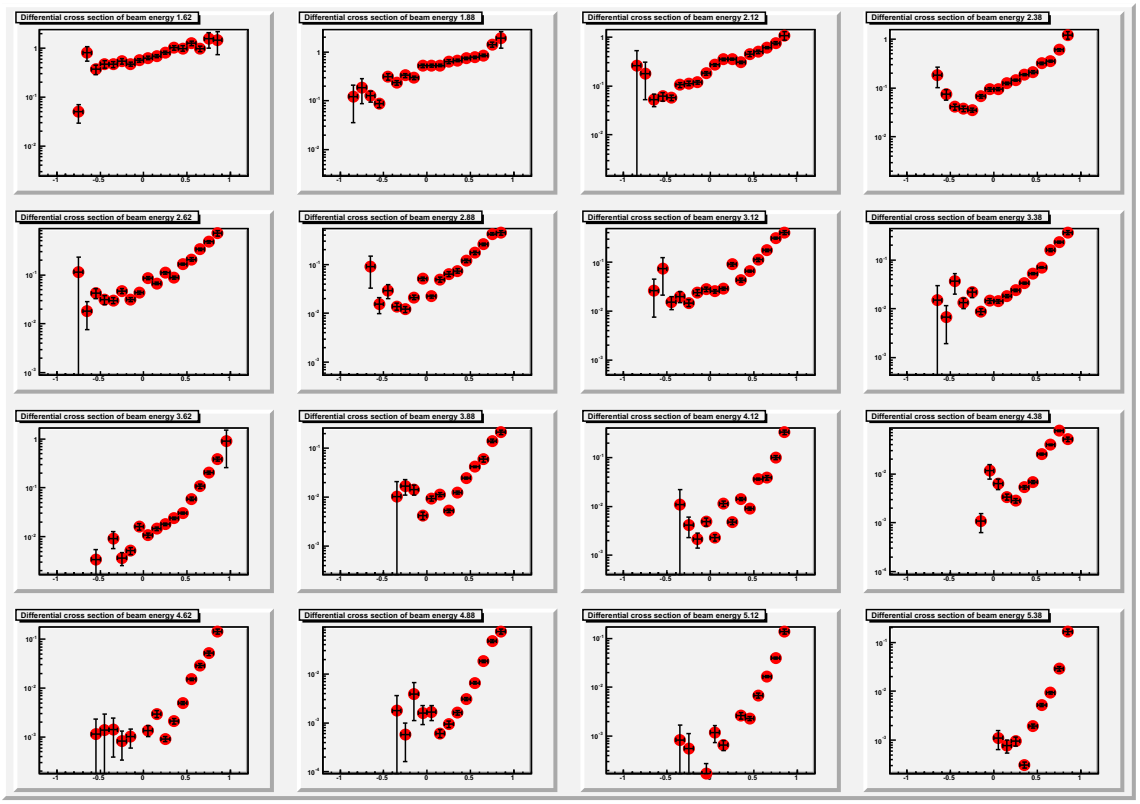

FIGURE 5.10. Differential cross section for $cos\left(\theta^{K}_{cm}\right)$ dependence on the cosine of the angle of K^{+} in the center-of-mass frame in log scale. The photon beam energy starts from 1.5 GeV at the top left to 5.5 GeV at the bottom right.

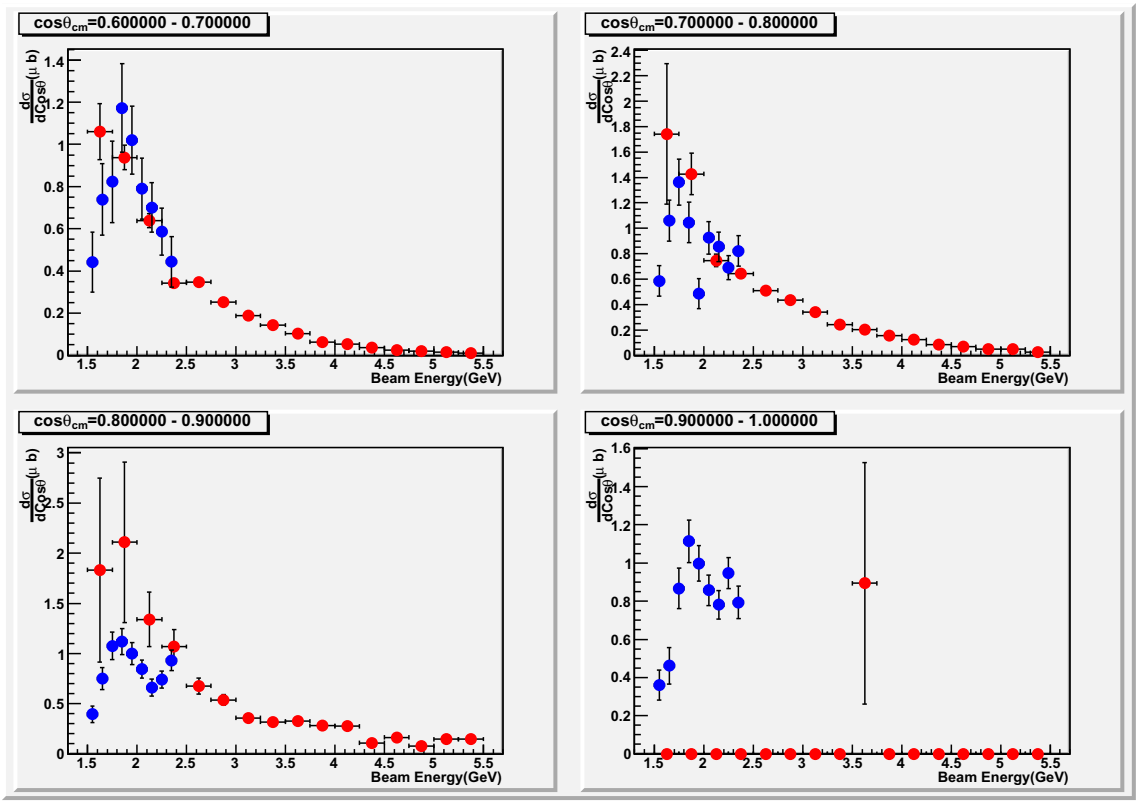

FIGURE 5.11. Comparison of differential cross section with previously published results in the region where they kinematically overlap. Red dots are data from this work. Most of them are consistent with previously published results. There is no coverage of my data in the most forward angle, which is the graph at the bottom right.

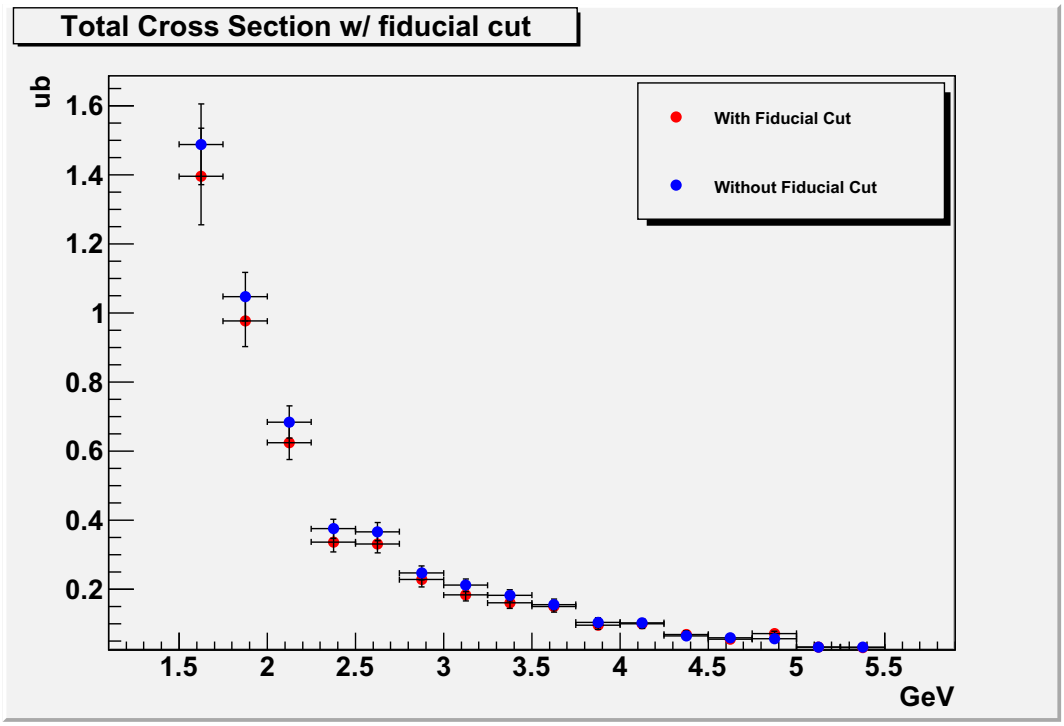

FIGURE 5.12. Comparison of total cross sections with and without fiducial cut. The dots in red show the cross sections with fiducial cut, and those in blue without fiducial cut. The differences are within statistical errors.

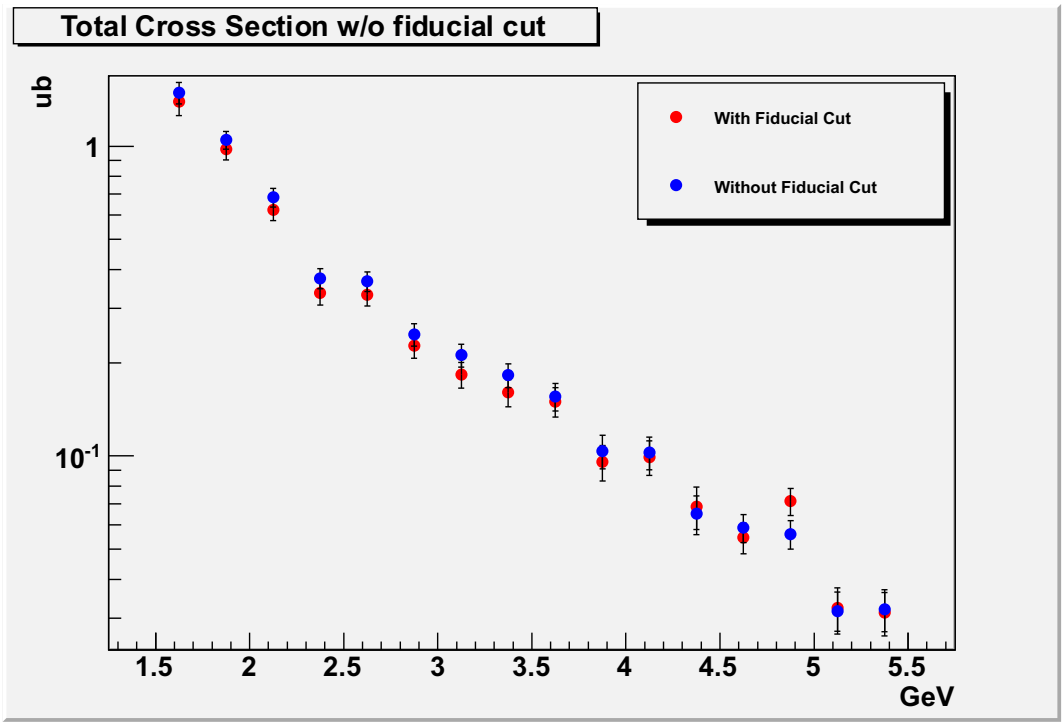

FIGURE 5.13. Comparison of total cross sections in log scale with and without fiducial cut. The dots in red show the cross sections with fiducial cut, and those in blue without fiducial cut.

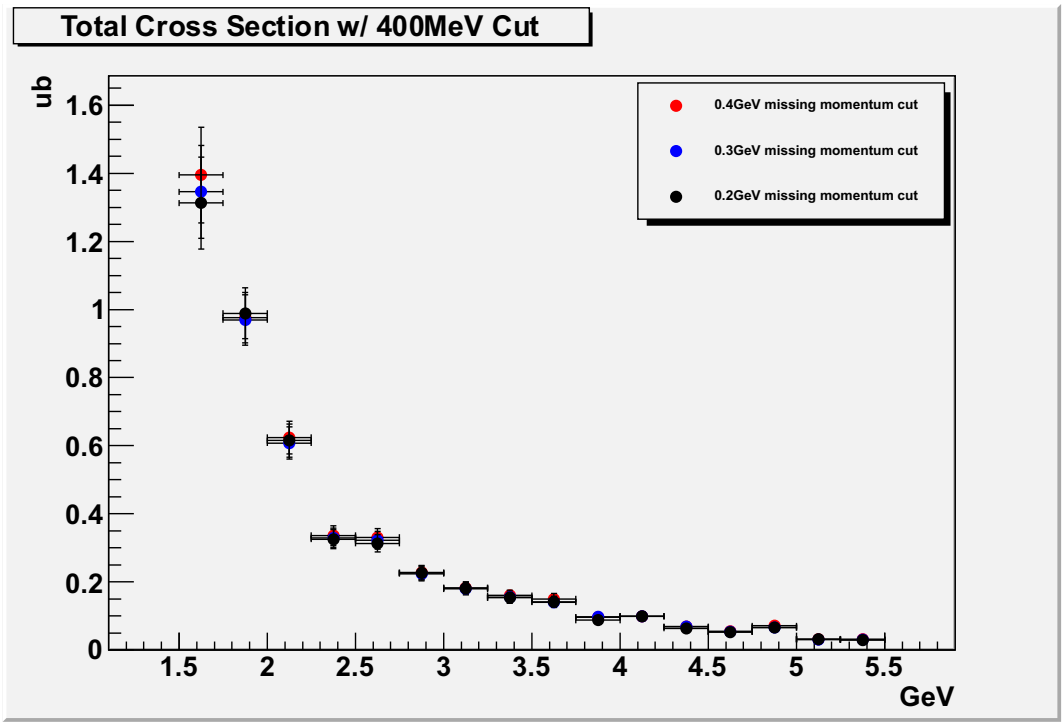

FIGURE 5.14. Comparison of total cross section with different missing momentum cuts. The dots in red are the cross sections with 400 MeV missing momentum cut, in blue with 300 MeV cut, and in black with 200 MeV cut. They agree within statistical errors.

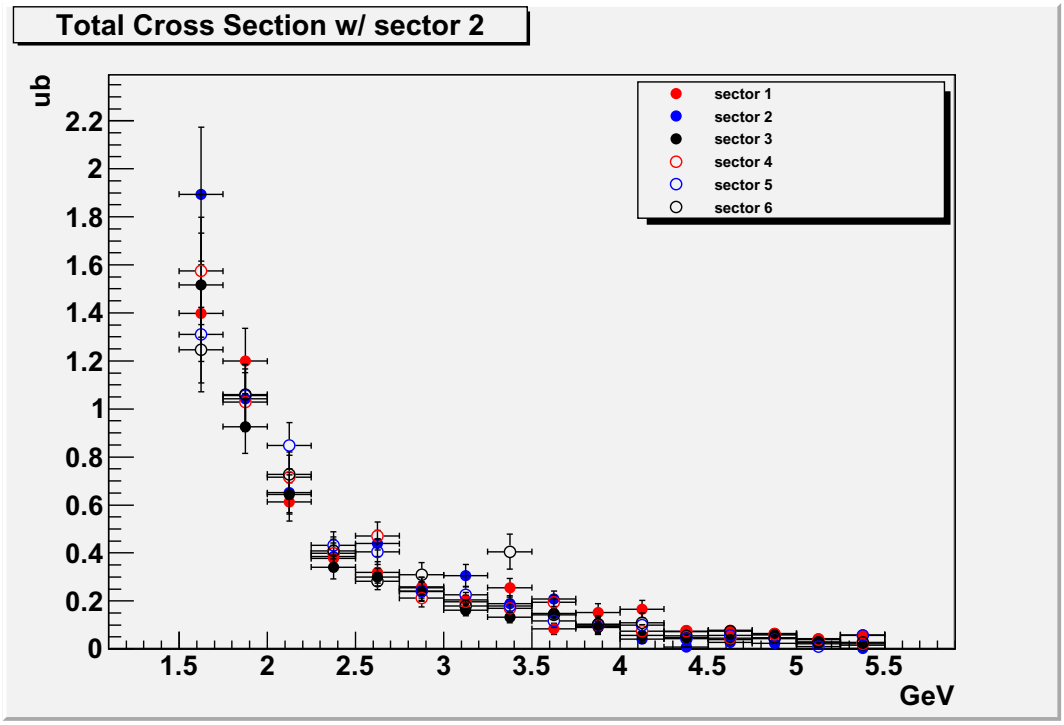

FIGURE 5.15. Comparison of total cross section with K^+ in different sectors.

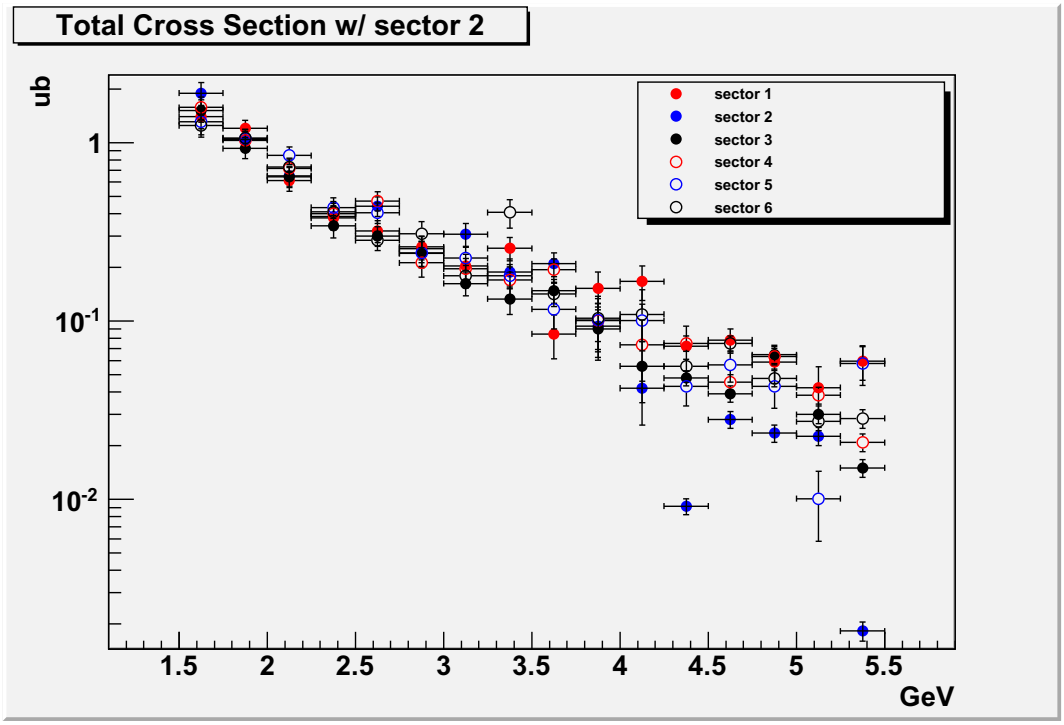

FIGURE 5.16. Comparison of total cross section in log scale with K^+ in different sectors.

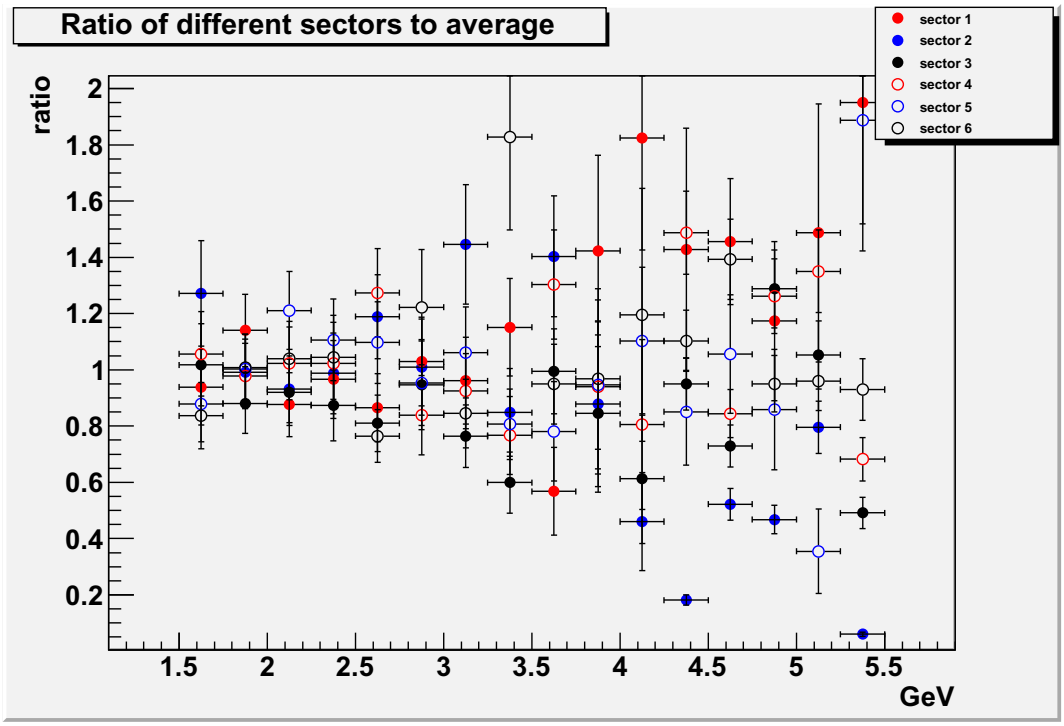

FIGURE 5.17. Ratios of total cross sections with K^+ in different sectors to the average.

Chapter 6

Exchange Meson Study

6.1. Theory

It is important to study which meson, K^+ or K^{*+}, has been exchanged in the t channel process. As discussed in the theoretic part of the chapter 1.3.2, it not only affects the value of the cross section, but also the production mechanism in this

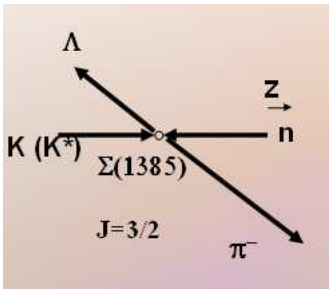

Figure 6.1. Reaction in the Gottfried-Jackson frame. This frame is the rest frame of Σ^{*-} and the z direction is antiparrallel to the direction of the baryon, n. The angle is the polar angle of the decay, π^-, of the resonance Σ^{*-}.

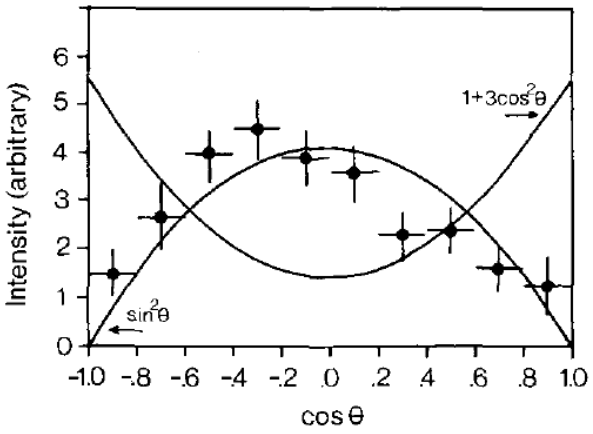

Figure 6.2. Different shapes corresponding to different distributions of substates. This is used to study which substate the production favors.

channel. However, those exchange particles are virtual and they only exist within the interaction phase space. They cannot be measured directly. However, a theory based on the spin density matrix was developed and used to study Λ^* by Barber and et al [2].

The idea is to study the acceptance-corrected event rate in the t-channel helicity frame. The frame is the rest frame of the resonance where the virtual meson collides with baryon head on. In this case, the meson is either K or K^*, the baryon is a neutron and the resonance is a Σ^{*-}. The dependence of the rate on the polar angle of the decay meson, here a π^-, should follow the distribution

$$\sigma = \alpha \left(\frac{1}{3} + cos^2\theta \right) + \beta \left(sin^2\theta \right) + \gamma \left(cos\theta \right), \tag{6.1}$$

where $\alpha\beta\gamma$ are three coefficients and θ is the polar angle. This describes the spin space by using a spin density matrix. For Σ^{*-}, a particle of spin $\frac{3}{2}$, there are two substates with $|S_z|$ equal to $\frac{1}{2}$ and $\frac{3}{2}$. The angle distribution of $\frac{1}{2}$ should behave like the first term and $\frac{3}{2}$ like the second term in Eqn.(6.1). The different behavior of the two terms is shown in Figure 6.2.

6.2. Previous Study

As stated in the chapter 1.3.1, there is only one published experiment on this channel and that experiment the exchange meson could not be studied due to the limitation of their detector system. However, a similar channel has been studied, which is $\gamma p \to K^+\Sigma^{*0}$. This channel is connected with the channel this work studied by isospin symmetry. Therefore, similar results might be expected for those two channels.

The preliminary results from Guo [8] are shown in Figure 6.3 and results are obtained from the fits shown in Figure 6.4.

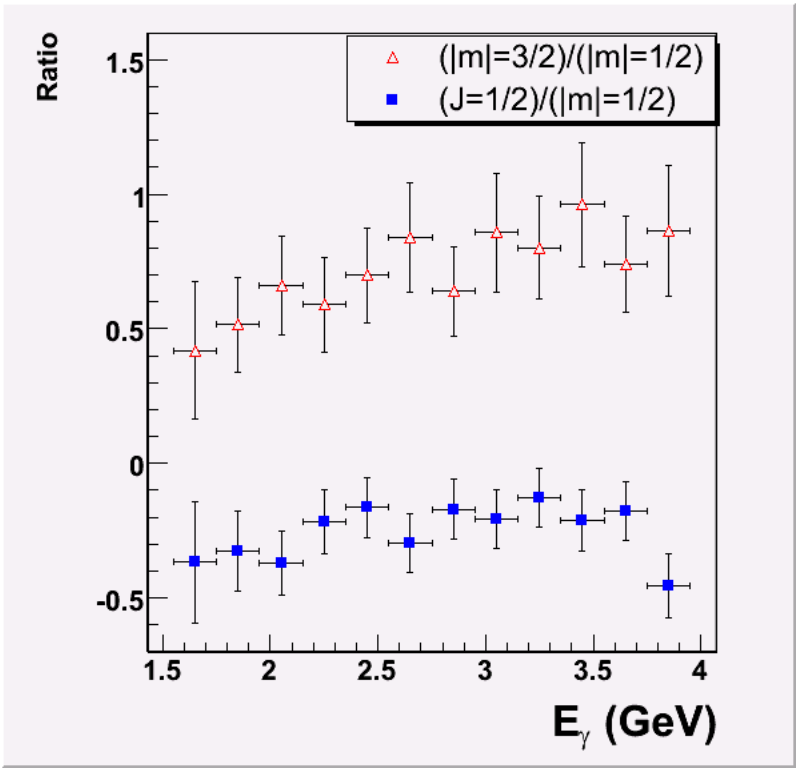

FIGURE 6.3. The ratio of two substates dependence on photon energy of Σ^{*0}. The triangle denotes the ratio of the second term to the first term and the square denotes that between the last term and the first term in Eqn.6.1.

6.3. RESULT

The result is obtained by several steps similar to those used to obtain the cross section. The first is to bin data into energy bins the same as those used to extract total cross section. The second and the third, also similar to the previously described steps to calculate the corrected yields, are to fit the missing mass peaks and subtract side band contribution to determine the yield. The same steps are done in the simulation to obtain the acceptance. After obtaining the acceptance-corrected yield, the distribution is fitted and plotted in Figure 6.5. The ratios of the two substates for different photon energies are shown in Figure 6.6.

In order to get the correct fitting errors for the ratios, a distribution of χ^2 dependent on the two ratios (the second and the last term to the first term in 6.1) is

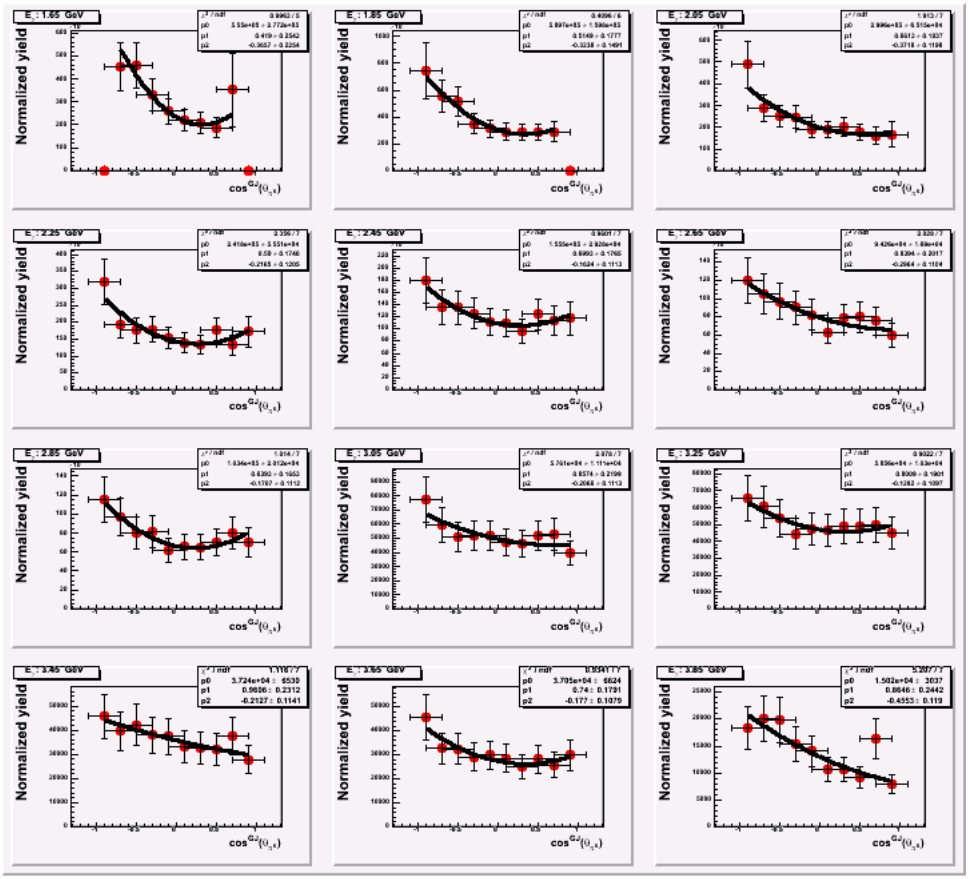

FIGURE 6.4. The fits to obtain the ratio of two substates of Σ^{*0}. The photon energy ranging from 1.5 GeV at the left top to 4 GeV at the right bottom.

generated in the way that the third color circle from the center is around where the result of fitting errors are read from.

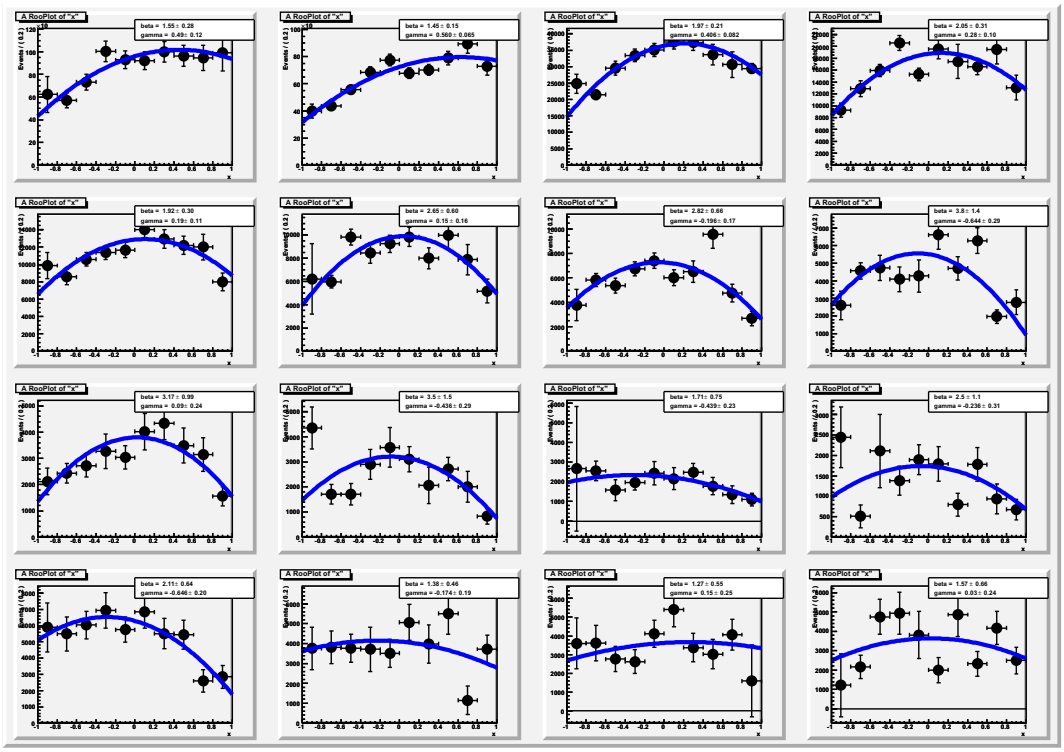

FIGURE 6.5. The fits to obtain the ratio of the two substates of Σ^{*-}. The photon energy ranges from 1.5 GeV to 5.5 GeV and shown from the top left to the right bottom.

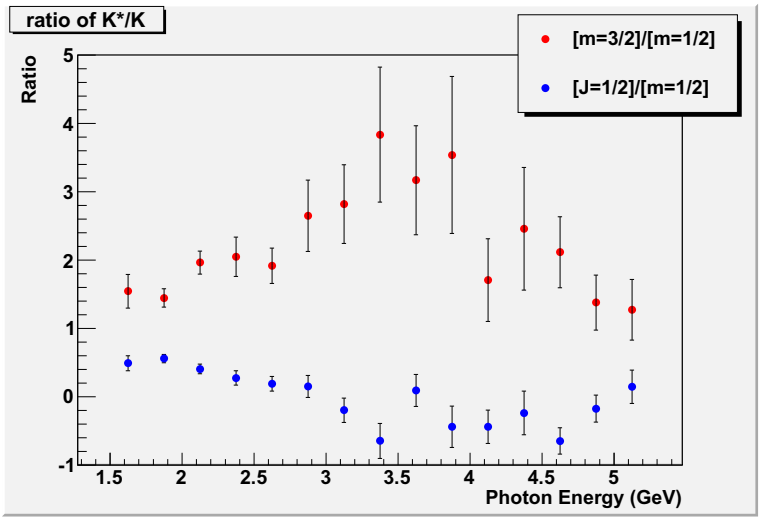

FIGURE 6.6. The ratio of the substate $|m_z| = \frac{3}{2}$ to the substate $|m_z| = \frac{1}{2}$ dependence on photon energy of Σ^{*-}. Similar to Figure 6.3, the red denotes the ratio of the second term to the first term and the blue denotes that between the last term and the first term in Eqn.6.1.

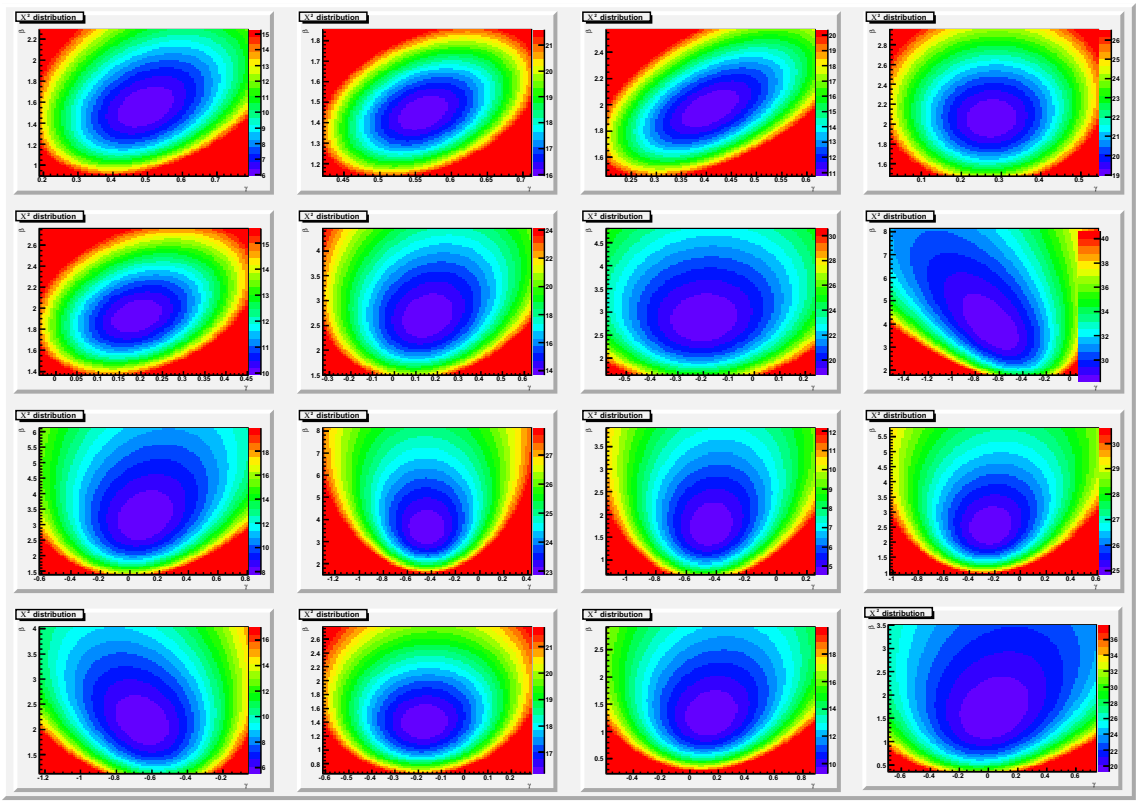

FIGURE 6.7. The χ^2 map of the two ratios in different photon energy bins. They are shown in the way that the third color circle from the center is about where the result of fitting errors are read from.

Chapter 7

Summary and Discussion

This analysis obtained the first total cross section of $K^+\Sigma^{*-}$ photoproduction at an extended photon beam energy ranging from the production threshold to 5.5 GeV, by using EG3 data set obtained in the Hall B at Thomas Jefferson national laboratory. The differential cross section obtained is consistent in the overlapping kinematic region with the previously published results from a different data set. However, it extends to the region of significantly higher photon energies. The differential cross sections exhibit strong t-channel production characteristics as predicted. Furthermore, in the extended region, the results show signs of nucleon excitation resonances, which decay into $K^+\Sigma^{*-}$. This may help the situation of the "missing resonances" puzzle.

In the other way, the production mechanism should be very similar to the Σ^{*0} production off the proton. In the center-of-mass frame of Σ^*, the decay particles are Λ and π^- in Σ^{*-} production or Λ and π^0 in Σ^{*0} production. The π^- and $\pi 0$ are members of the same isospin triplet. At the side of incoming particles, proton and neutron are members of the same isospin doublet. Therefore, the isospin symmetry and electric charge conservation requires that the other incoming particle should be the same for these two reactions. The comparison is shown in Table 7.1. Every particle in these two reactions have corresponding particles in the same isospin singlet, doublet or triplet. The difference of charge on the side of decay particles already reflects on

Table 7.1. Comparison of $K^+\Sigma^{*0}$ and $K^+\Sigma^{*-}$ production

Incoming 1	Incoming 2	Decay 1	Decay 2
X_0	p	Λ	π^0
X_-	n	Λ	π^-

the proton and neutron. Therefore, the X_0 and X_- in Table 7.1 have to be the same if isospin symmetry is preserved. In case of more than one possibilities, the ratio of them is the same instead. In the t-channel helicity frame, the distribution reflects the ratio of the two possibilities as discussed in Chapter 6. However, the difference of the ratios obtained from the distributions in these two channels implies that either the isospin symmetry is broken in this case, if the results from both channels are correct.

Bibliography

[1] J. Ball and E. Pasyuk. Photon flux determination through sampling of "out-of-time" hits with hall b photon tagger. *CLAS Note*, (2005-014), 2005.

[2] D. P. Barber and et al. *Z. Phys. C.*, 7(17), 1980.

[3] Siegfried Bethke. Experimental tests of asymptotic freedom. *Prog. Part. Nucl. Phys.*, 58:351–386, 2007. doi: 10.1016/j.ppnp.2006.06.001.

[4] Simon Capstick and W. Roberts. $n\pi$ decays of baryons in a relativized model. *Phys. Rev. D*, 47:1994–2010, 1993.

[5] Murray Gell-Mann. Symmetries of baryons and mesons. *Phys. Rev.*, 125(3): 1067–1084, Feb 1962. doi: 10.1103/PhysRev.125.1067.

[6] D. J. Gross and Frank Wilczek. ULTRAVIOLET BEHAVIOR OF NON-ABELIAN GAUGE THEORIES. *Phys. Rev. Lett.*, 30:1343–1346, 1973. doi: 10.1103/PhysRevLett.30.1343.

[7] D. J. Gross and Frank Wilczek. Asymptotically Free Gauge Theories. 1. *Phys. Rev.*, D8:3633–3652, 1973. doi: 10.1103/PhysRevD.8.3633.

[8] Lei Guo, 2007. private communication.

[9] Rajan Gupta. Introduction to lattice QCD. 1997.

[10] K. Hicks and et al. Cross sections and beam asymmetry for $k + \sigma * -$ photoproduction from the deuteron at $e\gamma = 1.5 - -2.4gev$. *Phys. Rev. Lett.*, 102(1): 012501, Jan 2009. doi: 10.1103/PhysRevLett.102.012501.

[11] B. A. Mecking and et al. The cebaf large acceptance spectrometer (clas). *Nuclear Instruments and Methods in Physics Research Section A*, 503.

[12] Yongseok Oh, Che Ming Ko, and K. Nakayama. Nucleon and δ resonances in $k\sigma(1385)$ photoproduction from nucleons. *Phys. Rev. C*, 77(4):045204, Apr 2008. doi: 10.1103/PhysRevC.77.045204.

[13] H. David Politzer. RELIABLE PERTURBATIVE RESULTS FOR STRONG INTERACTIONS? *Phys. Rev. Lett.*, 30:1346–1349, 1973. doi: 10.1103/PhysRevLett.30.1346.

[14] Wikipedia. Particle physics. `http://commons.wikimedia.org/wiki/Particle_physics`.

[15] Kenneth G. Wilson. Confinement of quarks. *Phys. Rev. D*, 10(8):2445–2459, Oct 1974. doi: 10.1103/PhysRevD.10.2445.